HOLOGRAPHIC PATTERNING OF POLYMER DISPERSED LIQUID CRYSTAL MATERIALS FOR DIFFRACTIVE OPTICAL ELEMENTS

by

ROBERT ALLAN RAMSEY

Presented to the Faculty of the Graduate School of

The University of Texas at Arlington in Partial Fulfillment

of the Requirements

for the Degree of

DOCTOR OF PHILOSOPHY

THE UNIVERSITY OF TEXAS AT ARLINGTON

December 2006

To my wife Robin and daughter Rilee

who set the example and made me who I am.

ACKNOWLEDGEMENTS

I would like to thank my supervising professor Dr. Suresh Sharma for constantly motivating and encouraging me, also for his invaluable advice during the course of my studies. I wish to thank Dr. Ali Koymen, Dr. Asok Ray, Dr. Alex Weiss and Dr. Qiming Zhang for their interest in my research and for taking time to serve on my dissertation committee. I am especially grateful to Douglas Coyen for his unending curiosity in my research and for the helpful discussions and invaluable comments provided. I also wish to thank Dr. Robert Henry, Jay Atman, and Kalpesh Vaghela for their assistance in my research. Finally, I would like to express my deep gratitude to my wife Robin who has encouraged and inspired me throughout my graduate studies. I am extremely fortunate to be so blessed. I am also extremely grateful to my father, late mother, sister and brothers for their support and encouragement. Also my mother-in-law and father-in-law for their support. I also extend thanks to several of my friends who have helped me throughout my studies.

This research was supported, in part, by grants from the Texas Advance Technology Program under grant number 003656-0123-2001 as well as a Strategic Partnership of Research in Nanotechnology (SPRING) grant.

November 21, 2006

ABSTRACT

HOLOGRAPHIC PATTERNING OF POLYMER DISPERSED LIQUID CRYSTAL MATERIALS FOR DIFFRACTIVE OPTICAL ELEMENTS

Publication No. _____

Robert Allan Ramsey, Ph.D.

The University of Texas at Arlington, 2006

Supervising Professor: Suresh C. Sharma

Liquid crystals are a soft condensed matter phase that share properties with both isotropic liquids and crystalline solids. Composite materials formed from both low molecular weight liquid crystals and polymers are of both fundamental and technological importance. One method for preparing dispersions of polymers and liquid crystals is polymerization-induced phase separation. Photo-polymerization induced phase separation utilizes a mixture of a liquid crystal and a photo-curable polymer contained between two indium tin-oxide (ITO) coated glass substrates. Irradiation of the homogeneous pre-polymer mixture initiates polymerization, which in turn induces a phase separation between the polymer and liquid crystal. Holographically patterned polymer dispersed liquid crystals (H-PDLCs) are a recent descendent of the conventional PDLCs. Rather than a random dispersion of droplets, holographic exposure is used to selectively pattern the liquid crystal phase in well-defined planes creating diffractive optical elements. H-PDLCs can operate in the transmission or reflection diffractive modes, depending on the experimental geometry, and can be switched on and off with voltages just as con-

ventional polymer-dispersed liquid crystals (PDLCs). The realization of a switchable H-PDLC Bragg and Raman-Nath transmission and Bragg reflection gratings written with the 632.8 nm wavelength of He-Ne laser are developed and investigated. The observation of well-defined periodic grating structures, which are characterized with grating periods of $\Lambda \approx 210$ nm - 10.5 μm, are discussed in detail. Polymer functionality effects on formation kinetics along with morphology development are examined along with effects of externally applied electric fields on the diffraction efficiency and switching times. Theoretical models for these data are discussed and compared. Future research in this area along with initial experimental results in a new operational mode, the so called "Reverse Mode", are also examined and discussed.

TABLE OF CONTENTS

LIST OF FIGURES

LIST OF TABLES

CHAPTER 1

LIQUID CRYSTALS AND POLYMER MATERIALS

Soft condensed matter constitutes a large class of materials that are neither simple liquids nor crystalline solids. Materials such as liquid crystals, polymers, colloid suspensions, emulsions, membranes and a large class of biological materials are all classified as soft condensed matter. It is termed "soft matter" because most of the materials have a much smaller Young's modulus than traditional solid state materials like metals or semiconductors. In spite of their various forms, many soft condensed matter materials share common properties such as disorder at the molecular scale, order at mesoscopic scale, and weak interaction strengths close to the thermal energy between the molecules. As a subdiscipline of materials science, soft matter is of increasing importance in the physical studies of the unique properties of these materials as well as the critical importance of the these materials in a variety of industrial, military and bio-physics applications.

In this chapter, an introduction is presented on a variety of soft matter materials namely; liquid crystals, polymers, reactive mesogens and dispersions of liquid crystal/polymeric materials. We will focus on the properties of these materials on scales from nanometers to microns. The properties discussed are strongly correlated to the physical and electro-optical performance of the studied liquid crystal/polymer composite materials. This chapter will provide a general background which will be useful in subsequent chapters.

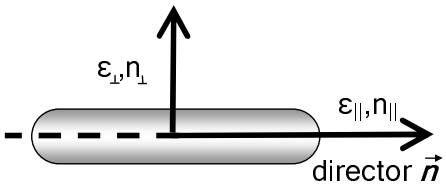

Figure 1.1. Rod-like or calamitic liquid crystal molecule with director $\vec{\mathbf{n}}$.

1.1 Liquid Crystals

As most people discovered in school, there are three simple phases of matter present in nature: solids, liquids and gases. However, in 1888 F. Reinitzer, a botanist, found that a type of cholesterol benzonate exhibited an intermediate phase between the liquid and solid phases.[1] When heated to 145.5^{o}C the material transformed into a translucent liquid and then transformed into a transparent liquid even at higher temperatures. This phase is referred as the liquid crystal phase, which was coined in 1889 by O. Lehmann.[2] Materials capable of forming liquid crystal phases are called *mesogens*.[3] Liquid crystals usually exhibit one or more intermediate phases between crystalline solid and isotropic liquid phases. In this intermediate phase they retain the ability to flow like ordinary liquids, but also possess long-range orientational order. Some liquid crystals may also have translational order as well.

While all liquid crystal's are molecularly anisotropic, the nature of this shape anisotropy falls into two categories: *calamitic* liquid crystals which are shaped like rods, and *discotic* liquid crystals which are shaped like disks. Calamitic liquid crystals consist of elongated molecules where the direction of the long axis of the molecule is called the *director*(See Figure 1.1).[4, 5, 6] The director is denoted by the vector $\vec{\mathbf{n}}$, which is an apolar vector; as $\vec{\mathbf{n}}$ and -$\vec{\mathbf{n}}$ are equivalent. Figure 1.2 shows the basic chemical structure of the most commonly occurring chemical structure of a calamitic liquid crystal molecule. They are aromatic, and if they contain benzene rings, they are often referred to as ben-

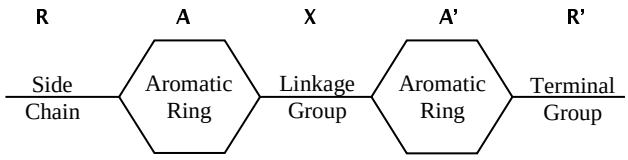

Figure 1.2. Molecular structure of a typical calamitic type liquid crystal.

zene derivatives. In general, aromatic liquid crystal molecules such as the one shown in Figure 1.2 are comprised of a side chain R, two or more aromatic rings A and A' connected by a linkage group X, and at the other end there is a terminal group, R'. Examples of side-chain and terminal groups are alkyl (C_nH_{2n+1}), alkoxy ($C_nH_{2n+1}O$), and others such as acyloxy, alkylcarbonate, alkoxycarbonyl, and the nitro and cyano groups. The **X**'s of the linkage groups are simple bonds or groups such as stilbene, ester, tolane, azoxy, Schiff base, acetylene and diacetylene. The names of calamitic liquid crystals are often fashioned after the linkage group. The chemical stability of liquid crystals depends very much on the central linkage group. Schiff-base liquid crystals are usually quite unstable. Ester, azo and azoxy compounds are more stable, but are also quite susceptible to moisture, temperature change and ultraviolet radiation (UV). Compounds without a central linkage group are among the most stable liquid crystals ever synthesized. Other compounds such as pyrimide and phenylcyclohexane are also quite stable.

There are quite a number of aromatic rings; these include saturated cyclohexane or unsaturated phenyl, biphenyl and terphenyl various combinations. The majority of calamitic liquid crystals are benzene derivatives. The rest include heterocyclics, organometallics, sterols and some organic salts or fatty acids. Heterocyclic liquid crystals are similar in structure to benzene derivatives, with one or more of the benzene rings replaced by a pyridine, pyrimidine or other similar group. Cholesterol derivatives are the most common chemical compounds that exhibit the cholesteric (or chiral nematic) phase

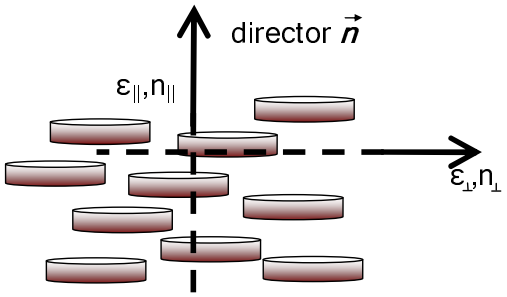

Figure 1.3. Disk-like or discotic liquid crystal molecule with director $\vec{\mathbf{n}}$ (nematic phase).

of liquid crystals. Organometallic compounds are special in that they contain metallic atoms and possess interesting dynamical and magneto-optical properties.[7]

So far the discussion has been devoted to calamitic liquid crystals, that is, the phases formed by rod-like molecules. In 1977 researchers in India discovered that disc-like molecules also form liquid crystal phases in which the axis perpendicular to the plane of the molecule tends to orient along a specific direction. These phases and the molecules that form them are called *discotic* liquid crystals. The most simple discotic phases is termed the nematic phase, because there is orientational order but no translational order. Such a phase is shown in Figure 1.3, where the discotic liquid crystals are shown as flat disks. The molecules move about quite randomly, but on average the axis perpendicular to the plane of each molecule tends to orient along the director $\vec{\mathbf{n}}$. An example of the chemical structure of a molecule possessing discotic liquid crystal phases is shown in Figure 1.4. These molecules are fairly rigid, planar center with hydrocarbon chains emanating in all directions. These features are common to just about all discotic liquid crystal molecules.

All the physical and optical properties of liquid crystals are governed by the properties of these constitute groups (e.g. side chain, linkage group, etc.) and how they are chemically synthesized together. Dielectric constants, elastic constants, viscosities,

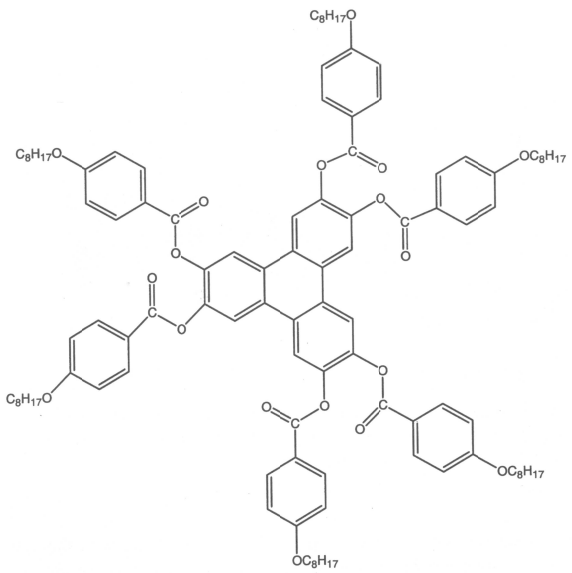

Figure 1.4. Molecular structure of a typical discotic type liquid crystal.

absorption spectra, transition temperatures, existence of mesophases, anisotropies and optical nonlinearities are all a consequence of how these molecules are engineered. Since these molecules are quite large and anisotropic, and therefore very complex, it is practically impossible to treat all the possible variations in the molecular architecture and the resulting changes in the physical properties. Nevertheless, there are some generally applicable observations on the dependence of the physical properties on the molecular constituents. These will be highlighted in the following sections.

1.1.1 Liquid Crystal Phases

One can classify liquid crystals in accordance with the physical parameters controlling the existence of the liquid crystalline phases. There are three distinct types of liquid crystals: *lyotropic*, *polymeric* and *thermotropic*. These materials exhibit liquid crystalline properties as a function of different parameters.

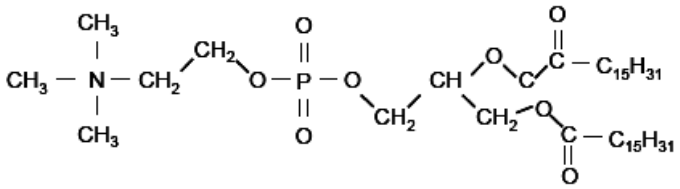

Figure 1.5. Illustration of a common phospholipid molecule.

1.1.1.1 Lyotropic Liquid Crystals

Lyotropic liquid crystals are obtained when an appropriate concentration of a material (solute) is dissolved in a solvent. The liquid crystal phase behavior is controlled by the concentration of the solvent/solute mixture. The principal interaction in lyotropic liquid crystals is the solute-solvent interaction. The most common systems are those formed by water and amphiphilic molecules (molecules that possess a hydrophilic part that interacts strongly with water and a hydrophobic part that is insoluble in water) such as soaps, detergents and lipids. When such molecules are placed in water the ends that exclude water tend to arrange themselves together, allowing the other end of the molecules to be in contact with the water. This effect results in structures of various shapes (spheres and cylinders are common) which themselves can be positioned in a very specific arrangement. A typical molecule that posses this type of characteristic is the common phospholipid molecule, whose chemical structure is seen in Figure 1.5. The molecules themselves are free to move about in the solvent, but as the do so, they retain the orientational and positional order due to the molecular structure, and are therefore proper liquid crystalline phases. One can represent molecules of this type by a circle (water-seeking) connected to a tail (water-excluding). Two of the many structures these molecules form are shown in Figure 1.6. There are quite a number of phases observed in such water-amphiphilic systems, as the composition and temperature are varied; some appear as spherical micelles and others possess ordered structures with one-, two- or

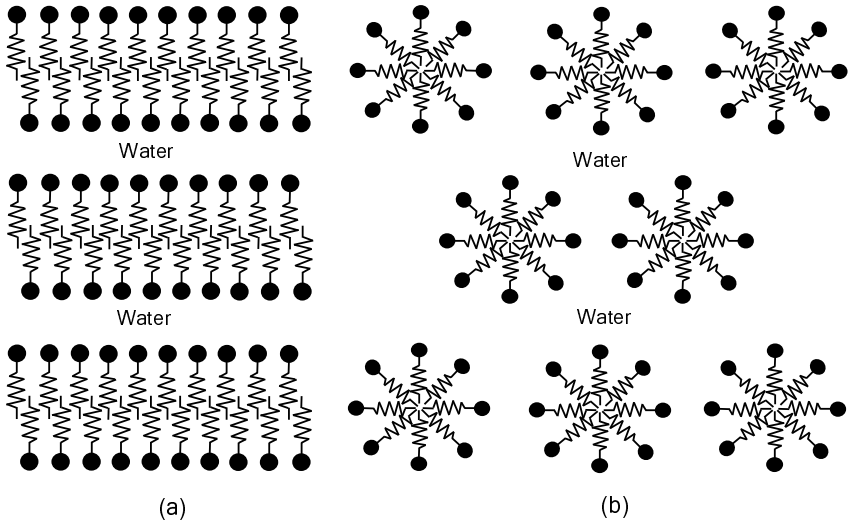

Figure 1.6. Cross-sections of the (a) lamellar and (b) hexagonal lyotropic liquid crystal phases. The round end of each molecule represents a hydrophilic (water-seeking) group, while the zigzag line depicts a hydrophobic (water-fearing) group.

three-dimensional translational order.[8] Lyotropic liquid crystals are mainly of interest in biological studies; an excellent review may be found elsewhere.[9]

1.1.1.2 Polymeric Liquid Crystals

Polymeric liquid crystals are compounds in which the mesogen is chemically attached to a reactive monomer, which can be polymerized to yield a high molecular weight compound with liquid crystalline properties (polymers and polymerization are

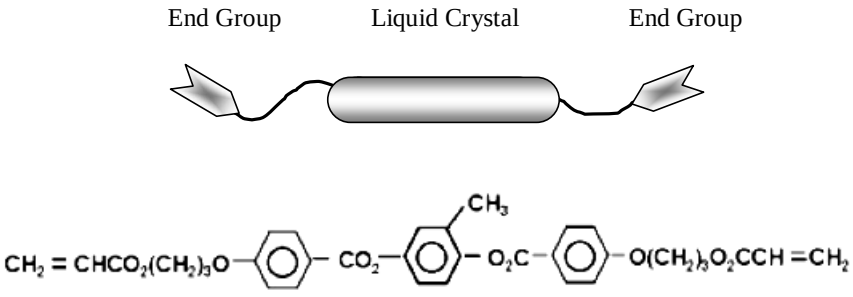

Figure 1.7. Schematic and chemical structure of the a typical reactive mesogen.

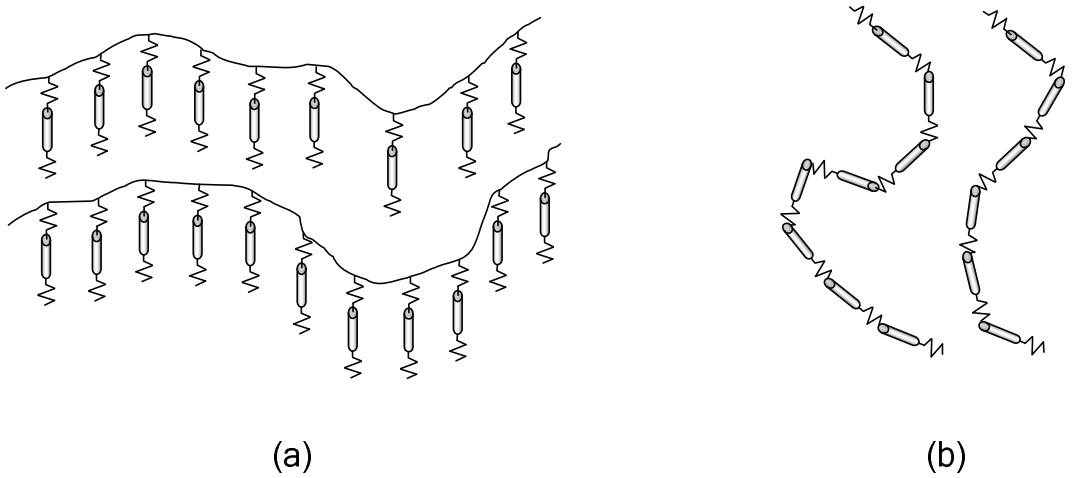

Figure 1.8. Illustration of the orientational order in (a) side chain and (b) main chain liquid crystal polymers. The rod-shapes represent rigid segments of the polymer and the zigzag lines represent the flexible segments.

discussed in detail in subsequent sections). Mesogenic or liquid crystalline polymers are classified in accordance with the molecular architectural arrangement of the mesogenic monomer. The structure and chemical makeup of a typical polymeric liquid crystal is seen in Figure 1.7. Liquid crystal side-chain monomers are formed by pendant side attachment of mesogenic monomers to a conventional polymeric chain, as depicted in Figure 1.8(a). Main-chain polymers are built up by joining together the rigid mesogenic groups in a manner depicted schematically in Figure 1.8(b); the link may be a direct bond or some flexible space. A good account of polymeric liquid crystals may be found in Ciferri et al.[10] In general, polymeric liquid crystals are characterized by a much higher viscosity than monomers and they are very useful for a wide range of applications such as reflective polarizers[11], optical compensation films for improving the viewing-angle characteristics of liquid crystal displays[12], liquid crystal elastomers[13, 14] and self-assembled microstructures with a locked-in dielectric anisotropy.[15]

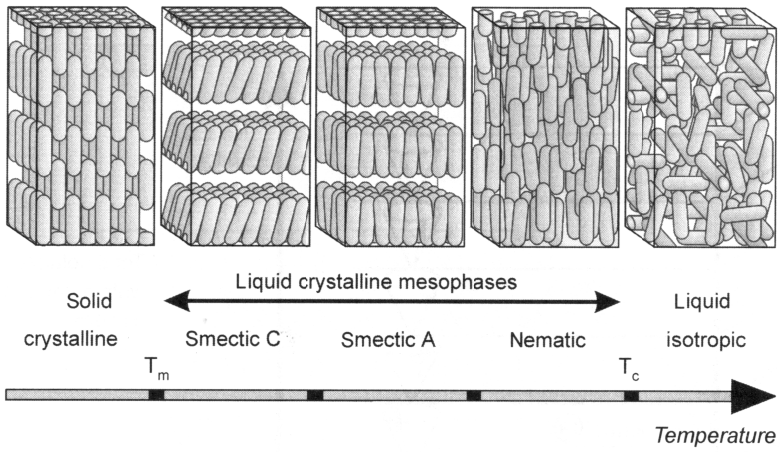

Figure 1.9. Phases of thermotropic liquid crystal materials as a function of temperature.

1.1.1.3 Thermotropic Liquid Crystals

The most widely used and extensively studied for their linear as well as nonlinear optical properties are thermotropic liquid crystals. They exhibit various liquid crystalline phases as a function of temperature. Although their molecular structures are, in general, quite complicated, they are often represented as either calamitic or discotic. There are three main classes of thermotropic liquid crystals: nematic, cholesteric, and smectic. In smectic liquid crystals there are several subclassifications in accordance with the positional (translational order) and directional (orientational order) arrangements of the molecules. These mesophases are defined and characterized by many physical parameters such as long- and short-range order, orientational distribution functions and so on.

We, again, primarily focus on calamitic type liquid crystals as they are the most important class of liquid crystals for electro-optical applications.[16] Below the melting point, T_M, calamitic liquid crystals are solid, crystalline and anisotropic, whereas above the clearing point with temperature $T_C > T_M$ they are a clear isotropic liquid. In the mesophase region, see Figure 1.9, between T_M and T_C, the material has the appearance of a milky liquid, but still exhibits ordered phases. These phases will be discusses in

the sequence given by increasing temperature. In a smectic phase, the molecules arrange themselves in planar sheets. Within each layer, the molecules are aligned, but have only one-dimensional translational order. Two common subclasses of smectic ordering are the smectic A phase and smectic C phase. The first phase above T_M is the smectic C phase. As all smectic phases, it is ordered in two dimensions (orientational and 1-D translational). The molecules are arranged with random deviations tilted to the plane of the layer. In the smectic A phase the directors of the molecules are, again with random deviations, perpendicular to the plane of the layer. The most disordered type of liquid crystalline phase is the nematic phase, which has no translational order, but in which the molecules, on average, orient about a particular direction (the director). Next to the clearing point (T_C), the nematic phase appears with only a one-dimensional order (orientational). (NOTE: It is possible to have a phase which has translational order in two dimensions as well as orientational order; this kind of phase is found in molecules that are discotic which form columnar phases) All members of these mesophases are anisotropic, as in the solid phases. Table 1.1 summarizes the different levels of translational and orientational order of different mesophases.

Table 1.1. Degrees of order in liquid crystal mesophases

PHASE	**TRANSLATIONAL ORDER**	**ORIENTATIONAL ORDER**
Liquid	None	None
Nematic	None	Yes
Smectic	One-Dimensional	Yes
Columnar	Two-Dimensional	Yes
Crystalline	Three-Dimensional	Yes

All thermotropic liquid crystal phases are characterized by long-range orientational order of the mesophases. However, the extent of translational order varies. The nematic

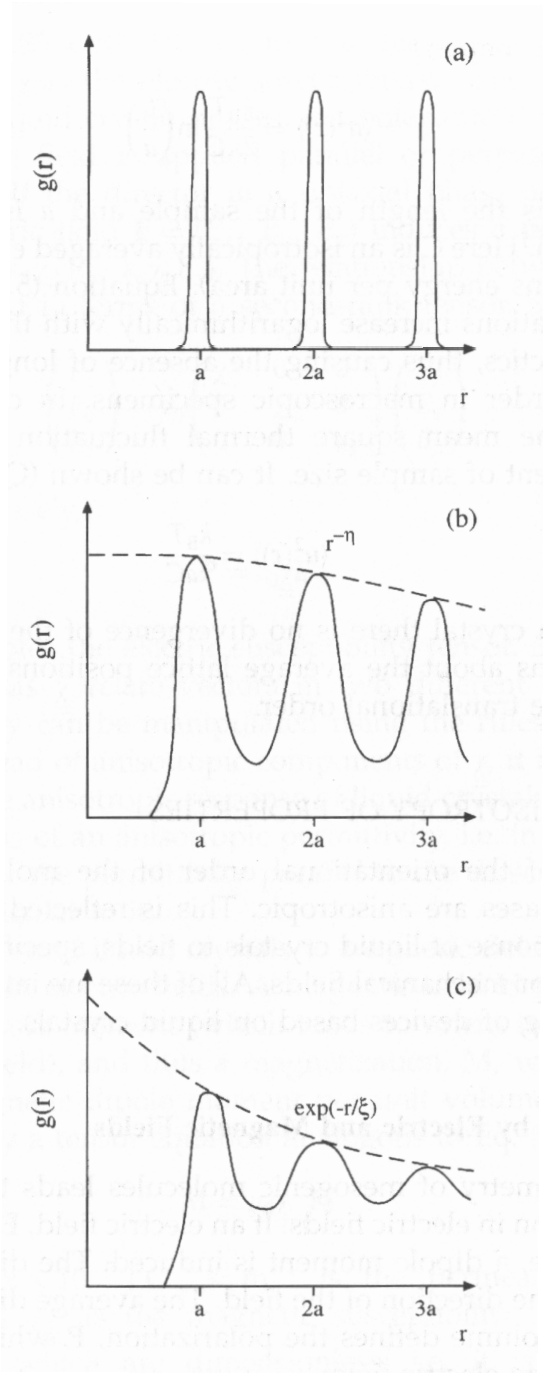

Figure 1.10. Schematic of radial distribution functions for (a) crystals, (b) smectic liquid crystal and (c) isotropic or nematic liquid crystal.

phase has no long-range translational order, whereas smectic and columnar phases are periodic in one and two dimensions respectively. The translation ordering of molecules is described by the radial distribution function, $g(r)$, which provides a mathematical description of the extent of translational order in the system.[17] With the use of the distribution function we can allow $g(r)r^2dr$ to be the probability that a liquid crystal molecule is located in the range dr at a distance r from one another. In crystals, $g(r)$ contains peaks that result from the periodic spacing of molecules in the lattice. Thermal fluctuations broaden these peaks, as seen in Figure 1.10(a). In contrast to crystals, liquids exhibit no long-range positional order, only local packing of molecules giving rise to weak oscillations in $g(r)$ (see Figure 1.10 (c)). In a liquid, this function decays as $\exp(-r\xi)$, where ξ is a translational correlation length. The form of $g(r)$ for a nematic liquid crystal is identical to that for a liquid, since both posses only short-range translational order. Smectic liquid crystals are periodic in one direction (normal to the layers). However, the Landau-Peierls instability destroys long-range ordering. Instead, the ordering is said to be quasi-long-range and decays slowly as $r^{-\eta}$ (see Figure 1.10 (b)), where η is a temperature-dependent exponent of the order 0.1 to 0.4.

Compared to smectic materials, as well as discotic materials, nematic liquid crystals usually have a much lower viscosity ($\sim$ 0.1 Pa·s), which makes them suitable for fast switching electro-optical applications. In this dissertation, we focus our attention on the properties and applications of nematic materials in liquid crystal/polymer dispersions.

1.1.2 Order Parameter

In the nematic phase one molecular axis tends to point along a preferred direction. The ensemble average of this preferred direction is called the nematic ensemble director and is denoted by the unit vector $\vec{\mathbf{n}}$. The degree of orientational ordering in a liquid

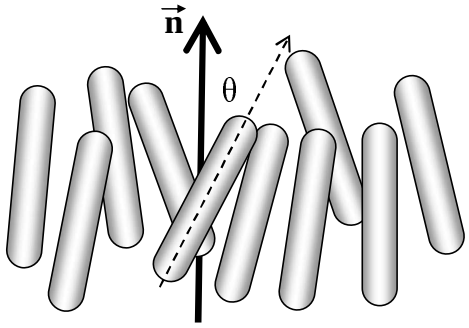

Figure 1.11. Orientational order between nematic liquid crystal molecules. The nematic director is indicated by $\vec{\mathbf{n}}$. The angle between the symmetry axis of an individual molecules and the director is denoted as θ.

crystal can be quantified by defining an order parameter. For a nematic liquid crystal this can be constructed phenomenologically as[18]

$$S = \left\langle \frac{3}{2}\cos^2\theta - \frac{1}{2} \right\rangle \tag{1.1}$$

Here, θ is the angle between the molecular symmetry axis and the director (see Figure 1.11). The brackets denote ensemble averaging. If all liquid crystal molecules are perfectly aligned ($\theta_i = 0^o$ for all i) then $S = 1$. If the system has no orientational order (liquid phase) then θ is expected to have any value with equal probability, and an ensemble average yields $S = 0$. This scalar order parameter, S, describes the microscopic orientational property of the nematic liquid crystal phase. The typical order parameter of nematic liquid crystals is ~ 0.5 to 0.7. The order parameter for all thermotropic liquid crystals is temperature sensitive. When temperature increases the order parameter decreases and jumps to zero at the nematic-isotropic transition temperature, or the clearing temperature T_c. Figure 1.12 shows the order parameter as a function of temperature, according to Maier-Saupe mean field theory.[19]

The scalar order parameter can be determined by optical measurements[20], X-ray scattering [21] and nuclear magnetic resonance investigations.[22] The order parameter

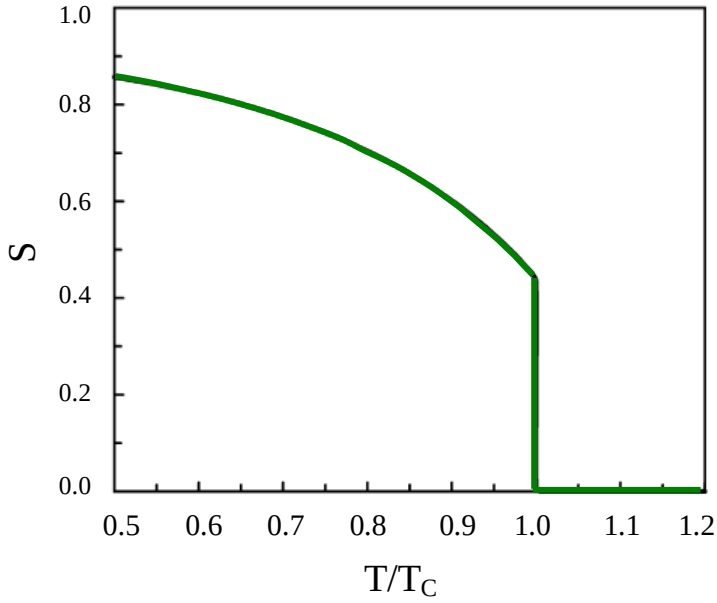

Figure 1.12. Nematic liquid crystal order parameter (S) plotted as a function of temperature.

is of much interest in the studies of liquid crystal because it is strongly correlated to the macroscopic properties of these materials, such as dielectric/optical anisotropy. For example, the optical birefringence of liquid crystals decrease with an increase in temperature. i.e. a decrease of the order parameter S. (see Section 1.1.3)

1.1.3 Anisotropy in Liquid Crystals

As previously mentioned, liquid crystals exhibit shape anisotropy which gives them their unique phase ordering properties. This shape anisotropy manifests itself in other physical properties of the material such as the dielectric constant, index of refraction, and magnetic susceptibility. Depending upon the direction of measurement these values can have considerably different values. There may be as many as three different values - one for each axis of symmetry. If two of the directions are equivalent the material is termed uniaxial, as in the case of the nematic liquid crystals we will discuss.

Considering a nematic liquid crystal in an applied electric field; the field will change the charge distribution in the molecules and induce dipole moments. Collectively, the induced polarization of the nematic liquid crystal is proportional, in the weak field limit, to

$$\mathbf{P} = \epsilon_o \chi \mathbf{E} \tag{1.2}$$

where $\epsilon_o = 8.86$ x 10^{-12} $C^2/N{\cdot}m^2$ is the permittivity of free space, χ is the macroscopic susceptibility tensor of the material which is strongly associated to the orientational order.[18] The direction of the induced polarization $\mathbf{P}$ (or the electric displacement $\mathbf{D} = \epsilon_o \mathbf{E} - \mathbf{P}$) does not have to be the same direction as the external field $\mathbf{E}$ as seen in Figure 1.13 (a). Due to the shape anisotropy of the liquid crystal molecule, the electric susceptibility has one value when the electric field is applied parallel ($\chi_{||}$) to the nematic director and a different value when applied perpendicular ($\chi_{\perp}$). The difference between these two values is

$$\Delta\chi = \chi_{||} - \chi_{\perp} \tag{1.3}$$

which is often expressed as the dielectric anisotropy

$$\Delta\epsilon = \epsilon_{||} - \epsilon_{\perp} \tag{1.4}$$

where $\epsilon = 1 + \chi$, and $\epsilon_{||}$, $\epsilon_{\perp}$ are the dielectric permittivities parallel and perpendicular to the molecular symmetry axis, respectively. The induced dipole moment will serve to reorient the nematic director such that its symmetry axis is parallel to the applied field direction ($\Delta\epsilon > 0$) or perpendicular to the applied field direction ($\Delta\epsilon < 0$). The value of $\Delta\epsilon$ is dependent on the chemical structure of the nematic liquid crystal. The typical values of dielectric anisotropy of nematic liquid crystals is $\Delta\epsilon \sim 5$ to 20. If the nematic mesogen is in the isotropic liquid phase the molecular anisotropy is eliminated and there is no dielectric anisotropy observed. Maier and Meier[23] showed that the dielectric anisotropy is proportional to the order parameter $\Delta\epsilon \propto S$, which was experimentally

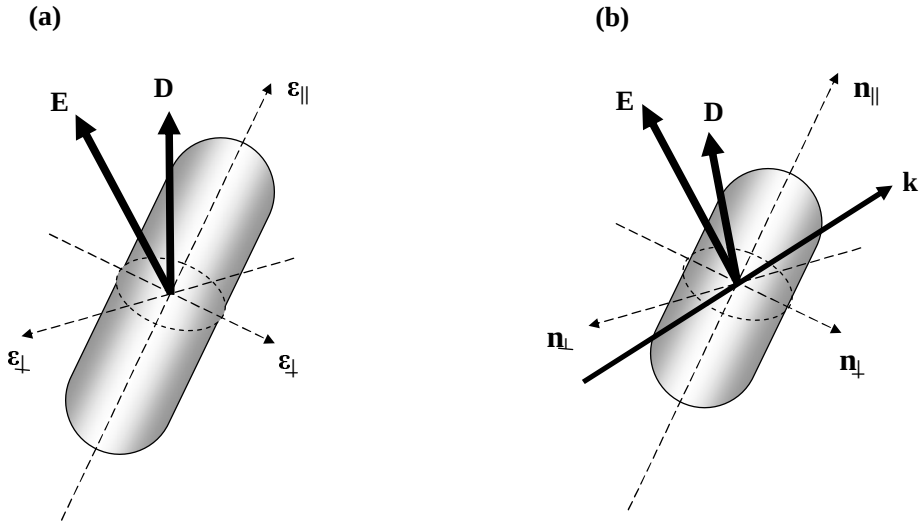

Figure 1.13. The dielectric anisotropy (a) and optical anisotropy (b) of a uniaxial nematic liquid crystal.

proved by de Jeu and Bordewijk.[20] Analogous properties hold true for magnetic susceptibilities also, however the fields necessary to achieve molecular reorientation are too high for most practical devices.

The dielectric constants of liquid crystals are also functions of frequency. Above the Debye frequency, $\omega_D \sim 10^{10}$ Hz, the response of dipole moments cannot follow such fast external perturbations and the dielectric constants relax to a lower value.[24] In the optical regime ($\omega \sim 10^{14} - 10^{16}$ Hz) the index of refraction, defined as $n(\omega) = \sqrt{\epsilon(\omega)}$, is also a tensor which induces an anisotropy in the optical regime termed *birefringence*. Considering the index of refraction for a nematic liquid crystal is a tensor of rank 2, there are 3 normal modes of propagation. If light propagates in the liquid crystal with the polarization parallel to the nematic director, we call it an extraordinary ray with the extraordinary index of refraction $n_{||} \equiv n_e$. If light propagates with the polarization normal to the director (2 modes occur for a uniaxial nematic), we call it an ordinary ray

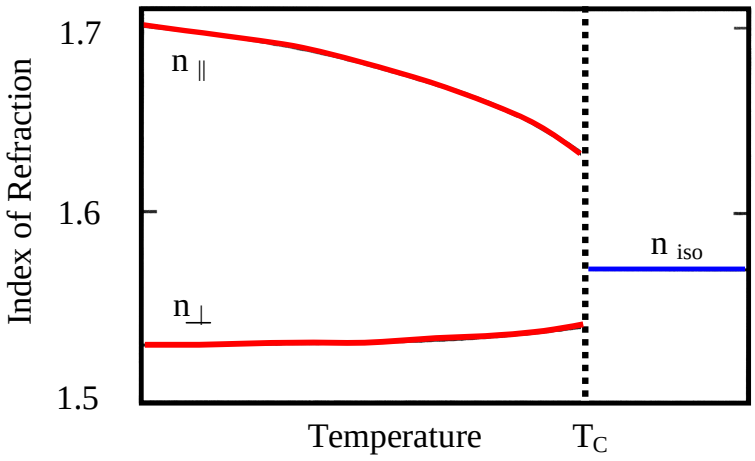

Figure 1.14. Indices of refraction as a function of temperature for a typical nematic liquid crystal.

with the ordinary index of refraction $n_\perp \equiv n_o$. For an incident optical wave ($\mathbf{k}$) with arbitrary polarization, as shown in Figure 1.13 (b) the index of refraction is given by

$$n(\theta) = \left[\frac{\cos^2\theta}{n_e^2} - \frac{\sin^2\theta}{n_o^2}\right]^{-\frac{1}{2}} \tag{1.5}$$

For nematic liquid crystals the optical anisotropy $\Delta n = n_e - n_o$ is positive. Negative optical anisotropy can be obtained in discotic materials.[25] The typical value of Δn for nematic liquid crystals is $\sim 0.05 - 0.3$, which holds for the whole optical spectral regime. Similarly the optical anisotropy is also a function of temperature and approximately proportional to the order parameter S.[26]. In Figure 1.14 the indices of refraction are plotted as functions of temperature. We can see the optical anisotropy Δn decreases as the temperature increases and vanishes in the isotropic phase.

1.1.4 Elastic Continuum Theory of Liquid Crystals

In most cases of interest the nematic liquid crystal is not uniformly aligned in a sample. Usually finite geometry constraints impart surface alignment effects, which influence the director orientation in the bulk of the material (see section 1.1.5). In most

cases distortions of the director from uniform alignment occur over microscopic lengths. If these distortions or variations are small, the order parameter can be safely assumed to be constant. A continuum theory has been developed based on the assumption that this is true and considers only liquid crystals elastic free energy.[18, 19] In a nematic system in equilibrium, the director is constant everywhere inside the liquid crystal. In a non-equilibrium state the elastic free energy per unit volume is proportional to the squares of the spatial derivatives of the director and can be written as[27, 28]

$$f = \frac{1}{2}k_{11}[\nabla \cdot \hat{\mathbf{n}}]^2 + \frac{1}{2}k_{22}[\hat{\mathbf{n}} \cdot (\nabla \times \hat{\mathbf{n}})]^2 + \frac{1}{2}k_{33}[\hat{\mathbf{n}} \times (\nabla \times \hat{\mathbf{n}})]^2 \tag{1.6}$$

where k_{11}, k_{22} and k_{33} are Frank elastic constants. (It is found that for most liquid crystals k_{11}, k_{22} and k_{33} are of the order 10^{-11} N and k_{33} is usually larger than k_{11} and k_{22}.) If we define the z-axis along the liquid crystal director, then

$$[\nabla \cdot \hat{\mathbf{n}}]^2 = \left[\left(\frac{\partial n_x}{\partial x}\right)_{y,z} + \left(\frac{\partial n_y}{\partial y}\right)_{x,z}\right]^2 \tag{1.7}$$

$$[\hat{\mathbf{n}} \cdot (\nabla \times \hat{\mathbf{n}})]^2 = \left[\left(\frac{\partial n_y}{\partial x}\right)_{y,z} - \left(\frac{\partial n_x}{\partial y}\right)_{x,z}\right]^2 \tag{1.8}$$

$$[\hat{\mathbf{n}} \times (\nabla \times \hat{\mathbf{n}})]^2 = \left(\frac{\partial n_x}{\partial z}\right)^2_{x,y} + \left(\frac{\partial n_y}{\partial z}\right)^2_{x,y} \tag{1.9}$$

Each equation above describes different types of deformations of the nematic liquid crystals, namely; splay, twist and bend, respectively, as seen in Figure 1.15. k_{11}, k_{22} and k_{33} are then called splay, twist and bend constants.

The contribution of liquid crystals coupling to external electro-magnetic fields can also be incorporated into this free energy expression by the addition of the extra terms

$$f_{field} = f_e + f_m = -\frac{1}{2}\epsilon_o \Delta\epsilon(\mathbf{E} \cdot \mathbf{n})^2 - \frac{1}{2}\frac{\Delta\chi}{\mu_o}(\mathbf{B} \cdot \mathbf{n})^2 \tag{1.10}$$

where $\Delta\epsilon$ and $\Delta\chi$ are the dielectric and magnetic anisotropy, respectively. The permeability of free space is denoted as μ_o ($\mu_o = 4\times\ 10^{-7}$ N$\cdot$s^2/C^2). The electric and magnetic

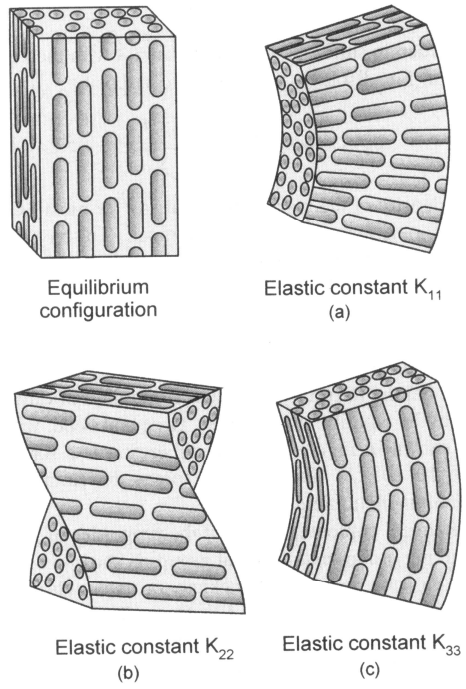

Figure 1.15. Equilibrium configuration; the elastic deformations splay (a), twist (b) and bend (c).

field vectors are given as **E** and **B**, respectively. One immediately notes that for a nematic with a positive dielectric anisotropy, alignment of the director along the field direction reduces the free energy density; thus nematic liquid crystals exhibit a preferred orientation in an applied field.

The interaction of a liquid crystal with a surface can also be treated using continuum elastic theory. The liquid crystal director on a surface typically posses a preferred orientation with respect to the surface. Anchoring free energy densities are usually treated by an even power series expansion about the sin of the derivation from a preferred tilt angle (See Figure 1.16). The Rapini-Papoular free energy density for anchoring is given as[29]

$$f_{surf} = \int \frac{1}{2} \left[W_\theta \cos^2(\phi - \phi_o) - W_\phi \sin^2(\phi - \phi_o) \right] \sin^2(\theta - \theta_o) dS \qquad (1.11)$$

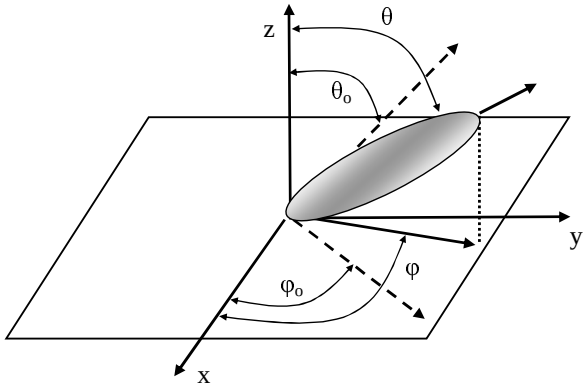

Figure 1.16. Interaction of a liquid crystal with a surface. Deformations from the tilt angle (defined by θ_o and ϕ_o) cost energy.

Here, θ and ϕ are the deviation from the preferred polar (θ_o, out-of-plane) and azimuthal (ϕ_o, in-plane) angle, respectively. W_θ and W_ϕ are the coefficients associated with the $\sin^2$ term of the respective energy expansions. Typical values of W are on the order of 10^{-4} to 10^{-7} J/m^2. In some cases $W_\theta > 10^{-3}$ J/m^2 and $W_\phi > 10^{-4}$ J/m^2 can be obtained.[30]

The total free energy of a nematic liquid crystal medium can be expressed as

$$F_{total} = \int_V f dV + \int_V f_{field} dV + \int_S f_{surf} dS \tag{1.12}$$

where V and S denote the volume and surface, respectively of the liquid crystal material. Equation 1.12 can be minimized using the Euler Lagrange equations to predict various system attributes.

Continuum elastic theory is extremely useful for calculating static director configurations, critical fields and dynamic response times of liquid crystals confined in various geometries. Equilibrium director configurations can be determined by minimization of the free energy density subject to specific boundary conditions. Critical fields are determined by balancing the free energy contributions of elastic deformation and an external

field. Also, by considering the balance of torques it is possible to determine dynamic response times for different director configurations.

1.1.5 Liquid Crystal Alignments

In a liquid crystal sample, various kinds of molecular alignment can be induced by treating the supporting substrate differently. Since there is no long range order in nematic liquid crystals the bulk material strongly scatters light. The scattering of light in nematic liquid crystals is 10^6 times stronger than in conventional isotropic liquids.[18] In order to make practical, functional devices and to achieve desirable optical performance proper alignment of nematic liquid crystals is necessary.

There are two common categories of liquid crystal alignment geometries: *homogeneous* alignment and *homeotropic* alignment, such as depicted in Figure 1.17. Homogeneous alignment occurs when the nematic director is parallel to the surface while homeotropic alignment occurs when the nematic director is perpendicular to the surface. The nematic order is fixed on the surface at the macroscopic scale and the order penetrates several microns inside the bulk of the sample. These alignments can be achieved by mechanical, chemical or optical treatments of the substrate surface. In 1911 Mauguin invented the process of rubbed polymer layers to achieve homogeneous alignments.[31] This technique is still the most common alignment method used in modern liquid crystal display technologies.[32] After mechanically rubbing the substrates, microgrooves are formed on the polymer surface and the directors of most liquid crystals prefer to align along the rubbing direction, i.e., the direction of the microgrooves. Besides rubbing, this microgroove structure can be generated through unidirectional polishing, tangential evaporation and the formation of relief grating structures on the substrate.[33, 34] In order to avoid introducing contaminating impurities or electrostatic charges during the rubbing process optical alignment methods were developed.[35, 36, 37] For example, po-

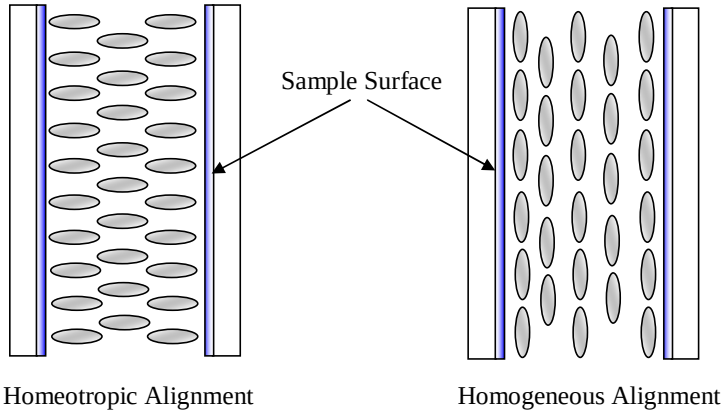

Figure 1.17. Homeotropic and homogeneous nematic liquid crystal alignment geometries.

larized ultraviolet (UV) exposure on a polymer doped with an azo dye can introduce an in-plane anisotropy and hence a homogeneous alignment direction.[35] The photoinduced alignment in some other materials is also possible.[36, 37] Homeotropic alignments are normally obtained chemically by treating the substrate with some specific long-chained surfactant such as silane.[38] Other sample geometries such as twisted and super twisted alignments are often employed in display applications, but are not relevant to this dissertation.

1.1.6 Liquid Crystals in Electric Fields and the Fréedericksz Transition

When a nematic liquid crystal is under the influence of an applied electric field, the resulting induced polarization (dipole moment per unit volume) is

$$\mathbf{P} = \epsilon_o \bar{\chi} \mathbf{E} \tag{1.13}$$

where $\bar{\chi}$ is the electric susceptibility tensor. If we assign the z-direction to be along the liquid crystal director, the above equation can be written as

$$\begin{pmatrix} P_x \\ P_y \\ P_z \end{pmatrix} = \epsilon_o \begin{pmatrix} \chi_\perp & 0 & 0 \\ 0 & \chi_\perp & 0 \\ 0 & 0 & \chi_{||} \end{pmatrix} \cdot \begin{pmatrix} E_x \\ E_y \\ E_z \end{pmatrix} \tag{1.14}$$

The electric displacement is, again, given as

$$\mathbf{D} = \epsilon_o \mathbf{E} + \mathbf{P} \tag{1.15}$$

or

$$\mathbf{D} = \bar{\epsilon}\mathbf{E} \tag{1.16}$$

where $\bar{\epsilon} = \epsilon_o(\bar{1} + \bar{\chi})$, and $\bar{1}$ is a unit tensor.

The component of an applied electric field parallel to the director, i.e.

$$E_{||} = \mathbf{E} \cdot \mathbf{n} \tag{1.17}$$

gives rise to an induced polarization also parallel to the director

$$P_{||} = \epsilon_o \chi_{||} E_{||} \tag{1.18}$$

Similarly, the component of the applied electric field perpendicular to the director,i.e.

$$E_\perp = \mid \mathbf{E} - (\mathbf{E} \cdot \mathbf{n})\mathbf{n} \mid \tag{1.19}$$

produces an induced polarization perpendicular to the director

$$P_\perp = \epsilon_o \chi_\perp E_\perp \tag{1.20}$$

The total induced polarization is then

$$\mathbf{P} = \epsilon_o \left[\chi_\perp \mathbf{E} + \Delta\chi(\mathbf{E} \cdot \mathbf{n})\mathbf{n}\right] \tag{1.21}$$

where $\Delta\chi = \chi_{||} - \chi_{\perp}$ is the susceptibility anisotropy. The energy density (electric energy per unit volume) is then found to be

$$U = -\frac{1}{2}\epsilon_o \left[\mathbf{E}^2 + \Delta\chi(\mathbf{E}\cdot\mathbf{n})^2\right] = -\frac{1}{2}\left[\epsilon_o E^2 + \Delta\epsilon(\mathbf{E}\cdot\mathbf{n})^2\right] \tag{1.22}$$

or in the case of interaction with optical fields we can write

$$U = -\frac{1}{2}\left[\epsilon_o\langle E^2\rangle + \Delta\epsilon\langle(\mathbf{E}\cdot\mathbf{n})^2\rangle\right] \tag{1.23}$$

where the bracket denotes an average over the optical cycle.

In the presence of an electric field, nematic liquid crystal molecules will realign themselves in order to minimize this energy, more specifically, the orientation-dependent part of Eqs.1.22 and 1.23. In other words, the applied electric field distorts the liquid crystal's director. For example, in a liquid crystal with positive dielectric anisotropy, the applied field will rotate the director such that it aligns parallel to the field. However, for any distortion to occur, the strength of the applied field has to be larger than a certain threshold in order to overcome the elastic and viscoelastic forces of the liquid crystal. This threshold is called the Fréedericksz threshold and the transition from an undistorted director configuration to a distorted one is called the Fréedericksz transition or the Fréedericksz effect. If the external field is an optical field, the effect is then called the Optical Fréedericksz Transition. Since this effect originates from the liquid crystal collective reorientation, it is nonlinear in the strength of the applied field (above the field threshold), and gives rise to a large nonlinear response which has been referred to as "Giant Optical Nonlinearity".[39, 40]

In addition to coupling with the director field directly, the applied electric field can also interact with the director field indirectly by means of the spontaneous dielectric polarization that arises from the director field distortion. This is called the flexo-electric effect[41], which is analogous to the piezoelectric effect in solids.

For splay, twist, and bend, the threshold field strengths for the Fréedericksz effect are (assuming strong anchoring at the boundaries)

$$(E_t)_{splay,twist,bend} = \frac{\pi}{d}\sqrt{\frac{k_{11,22,33}}{\epsilon_o \Delta\chi}} \tag{1.24}$$

where d is the sample thickness.

When the electric field strength becomes larger than the threshold field, convection instability will occur in the liquid crystal sample, due to a hydrodynamic effect caused by moving charge impurities. This electro-hydrodynamic instability[42] leads to the creation of a periodic distortion of the nematic alignment with spacing about equal to the sample thickness, which are called Williams domains or Williams striations.[43, 44] If the applied field strength is increased further, the flow becomes turbulent and the liquid crystal sample exhibits dynamic scattering.

1.2 Polymers and Photopolymerization

Polymers are another class of soft condensed matter which can be observed in our daily life, such as proteins, starches, rubbers, plastics, nylons, etc. The molecules in these materials have very high molecular weights and are called *macromolecules*. The typical polymer molecule is a chain of small species termed *monomer*. Most polymers are composed of hydrocarbon chains. Within each chain the atoms are bonded together utilizing covalent bonding. Between chains the interaction is much weaker than covalent bond strength which allows the chains to move with respect to each other. The molecular weight of these macromolecules can be of the order of millions as compared to tens for ordinary molecules. The simplest polymer molecule is the polyethylene (-CH_2=CH_2-) which is the main component to fabricate everyday plastic bottles. The molecular weight is on the order of 10^4 to 10^6.

At sufficiently low temperatures, regular polymer chains have a degree of translational ordering. As with all partly crystalline materials, a melting temperature, T_m, exists where the polymer becomes amorphous. A second-order phase transition to the glassy state also exists, T_g, above which the polymer is soft and pliable and below which it is hard and brittle. The glassy transition is characterized by increased molecular motion, such as chain rotation, which leads to dramatic changes in the mechanical properties of the material. In composite liquid crystal/polymer systems, both transitions are suppressed by plasticization, where the liquid crystal acts as a solvent for the linear polymer chains, resulting in a swollen network from the absorbed liquid crystal.

There are three main types of polymerization reactions which can be used to create polymer dispersed liquid crystal systems: chain, step, and ring-opening polymerization.[45] In chain polymerization, one end of the double bond becomes chemically active and can covalently link to another double bond. The new double bond becomes chemically activated, and can react with another monomer, and so on. In step polymerization, each reactive species can couple to only one other monomer to achieve a polymer the monomers must be at least di-functional with each end of the molecule reacting to form a chain. In ring-opening polymerization one of the reactants contains a cyclic structure that is subject to attack, the coupling reaction involves the opening of a ring.[46]

The number of reactive sites on an individual monomer is known as its functionality. A monofunctional molecule can react with only one other monomer to form a dimer, and no further reactions can take place. Di-functional monomers can react with each of two other monomers, resulting in a linear polymer chain. Monomers with three or more reactive sites form a branched or cross-linked structure, leading to a polymer network. These polymer structures are shown in Figure 1.18. The degree of cross-linking can dramatically affect the chemical and physical properties of the resulting polymer, even among similar monomers.

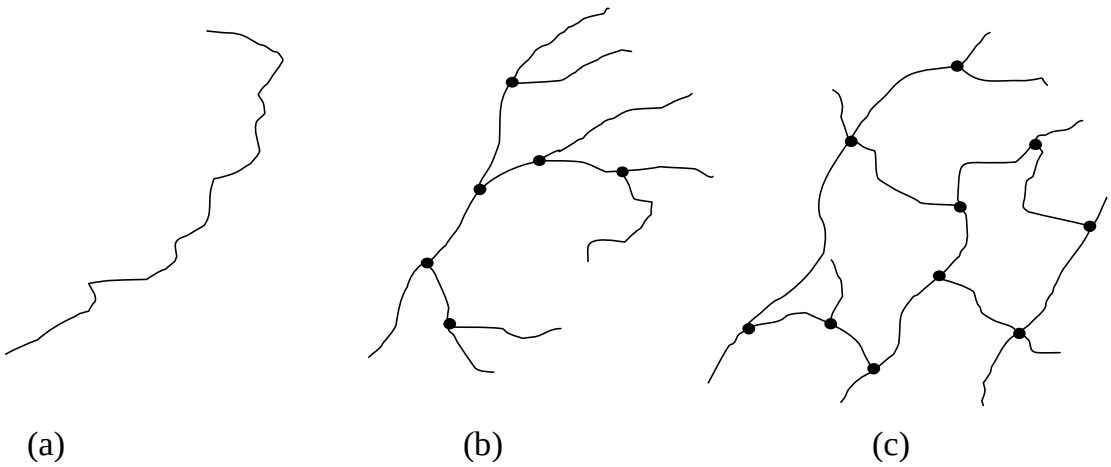

Figure 1.18. Structure of (a) linear, (b) branched and (c) crosslinked polymers.

The work described in this dissertations employs the chain polymerization method, because the chains tend to grow rapidly which causes a uniform phase separation in the liquid crystal-polymer systems. There are three stages to chain polymerization: *initiation*, *propagation*, and *termination*.[47] *Initiation* begins when a photoinitiator, I, absorbs a photon, $h\nu$, to react with a coinitiator, C, which in turn creates an activated species C^*. This species then reacts with a monomer, M, to complete the initiation process. The reaction kinetics are:

$$I + h\nu \rightarrow I^* \tag{1.25}$$

$$I^* + C \rightarrow C^* \tag{1.26}$$

$$C^* + M \rightarrow M\bullet \tag{1.27}$$

After initiation, the *propagation* stage begins, with more monomers added as the activated species moves to the end of the chain with each addition:

$$M\bullet + M \rightarrow (M\bullet)_2 \tag{1.28}$$

$$(M\bullet)_n + M \rightarrow (M\bullet)_{n+1} \tag{1.29}$$

The third stage, *termination*, occurs by one of two methods; combination or disproportionation. In combination, two propagating chains react to form a single chain and terminate the reaction:

$$(M\bullet)_m + (M\bullet)_n \rightarrow (M\bullet)_{n+m} \tag{1.30}$$

In disproportionation, a hydrogen atom is transferred from one chain to another, the free radicals are neutralized, and two chains result:

$$(M\bullet)_m + (M\bullet)_n \rightarrow (M\bullet)_{n+m} \tag{1.31}$$

1.3 Liquid Crystals/Polymer Dispersions

The phase separation of liquid crystal/polymer systems can lead to many interesting morphologies which attract a lot of interests not only to the richness of physical phenomena but also because of their diverse electro-optical application potential. In the following section a brief introduction of liquid crystal/polymer dispersions with high and low loadings of polymer as well as various photo-initiated curing techniques will be discussed.

1.3.1 Polymer-Dispersed Liquid Crystals

Polymer dispersed liquid crystals (PDLCs) are composite materials composed of discrete micron-sized nematic liquid crystal droplets randomly dispersed throughout a rigid polymer binder geometry. The droplet size can be controlled during the polymerization process and is usually comparable in size to the visible wavelength (1μm or less). The material is typically formed between transparent conducting Indium Tin Oxide (ITO) coated glass substrates, across which a voltage can be applied. In the case where homeotropic anchoring of the liquid crystal molecules to the polymer binder is preferred,

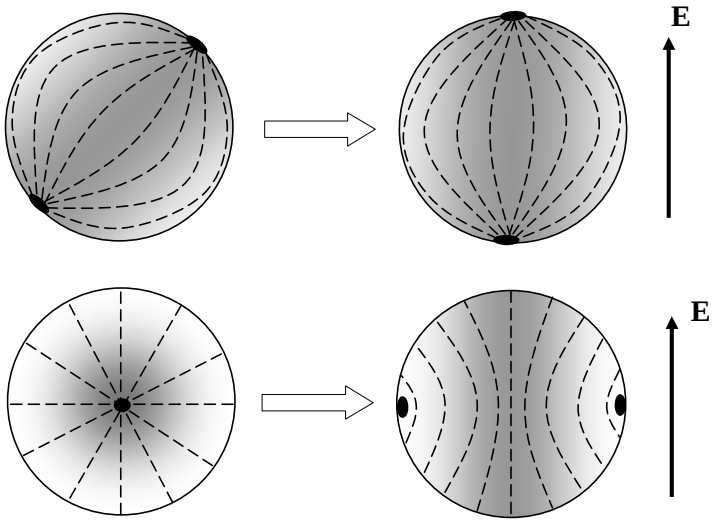

Figure 1.19. Various nematic director configurations in spherical cavities. Homogeneous parallel anchoring results in the bipolar (top-left) and aligned bipolar (top-right) configurations. Homeotropic anchoring yields radial (bottom left) or axial (bottom right) configurations .

elastic energy minimization results in a radial director configuration (See Figure 1.19).

If homogeneous parallel anchoring is preferred the nematic liquid crystal assumes a bipolar configuration. Anchoring is dictated by the interaction of the liquid crystal molecules with the polymer and can be controlled by proper choice of materials.[48] In most cases of interest, homogeneous anchoring is preferred and bipolar configurations result. In the absence of an external filed, the bipolar axes are randomly dispersed throughout the material. There exists a refractive index mismatch between the liquid crystal droplets and the polymer binder. The material incoherently scatters light, taking on an opaque, white appearance. Application of sufficient voltage across the electrodes reorients the bipolar droplets, aligning the director symmetry axes along the field direction. By design, the materials are chosen such that the polymer refractive index, n_p, is approximately equal to the ordinary index of the liquid crystal, n_o. Light propagating

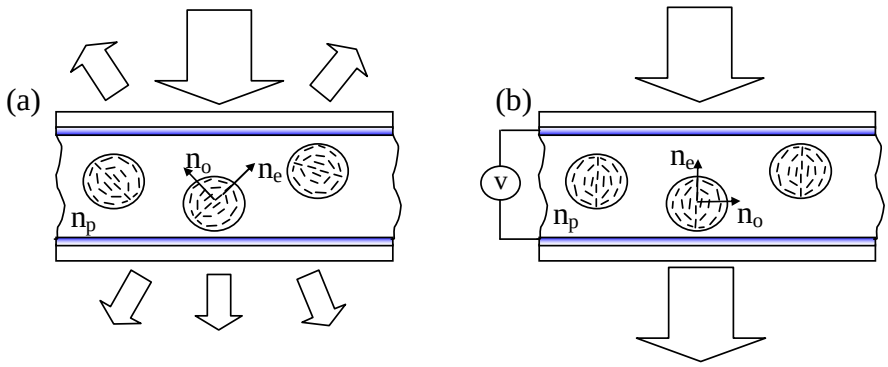

Figure 1.20. The operation of a polymer dispersed liquid crystal (PDLC) in the scattering state (a) and transparent state (b).

along the optical axis will no longer experience a refractive index mismatch and the material appears transparent. A schematic illustrating the operation of a typical PDLC is shown in Figure 1.20.

Several methods exist for making for making PDLC's.[45] These can be divided into two classes: phase separation[49] and encapsulation.[50] Phase separation methods begin with a homogeneous mixture, from which the liquid crystal component is phase separated out into droplets. The phase separation can be initiated several ways. In solvent induced phase separation (SIPS) the liquid crystal is dissolved with the polymer in a common solvent. Evaporation of the solvent results in a phase separation between the residual polymer and liquid crystal. In thermally induced phase separation (TIPS) process the liquid crystal is dissolved in a polymer melt. Cooling shifts the mixture to a region of the phase diagram favoring a two-phase system and phase separation occurs. Polymerization induced phase separation (PIPS) start with a homogeneous prepolymer-liquid crystal system where the polymerization process is initiated by irradiation.[51] The monomer used is sensitized to the radiation with the addition of a small amount of a photoinitiator. Polymerization results in a phase separation of the liquid crystal droplets.

PDLC's formed by encapsulation methods are also know as nematic curvilinear aligned phases (NCAP). These are formed by the dispersion of a liquid crystal into a water-borne polymer to form an emulsion. This is then coated onto a substrate. The droplets are formed in the emulsification process before the film is coated and allowed to dry.

1.3.2 Polymer-Stabilized Liquid Crystals

When the liquid crystal concentration is much higher than the concentration of polymer (typically 5% polymer concentration) the liquid crystal material represents the continuous binder while the crosslinked polymer is dispersed in the anisotropic fluid. This configuration is called polymer stabilized liquid crystals (PSLCs).[52, 53] In these systems the electro-optical behavior of the liquid crystal is not influenced significantly, whereas the mechanical strength is increase dramatically. Due to the dilute polymer network the index mismatch and scattering is negligible.

The general idea of PSLCs is the stabilization and alignment of a low-molecular mass liquid crystal by elastic interactions between the dispersed polymer network and liquid crystals as seen in Figure 1.21. Usually the photopolymerization process is used since full polymerization of a low concentration of monomer take a very long time. The monomer can be either isotropic or mesogenic. Depending on the order of liquid crystal and monomer properties the polymer network can be isotropic of anisotropic. The polymer morphology captures the orientational order. Thus the polymer network supports alignment of liquid crystals.

Compared to PDLCs, PSLCs can be electrically active under low voltage since a very small amount of polymer is dispersed in the liquid crystal host. The aligning effect of a dilute polymer network in PSLCs was modeled as an effective polymer field by several authors.[54, 55, 56] At low concentrations, this effective polymer field is estimated to

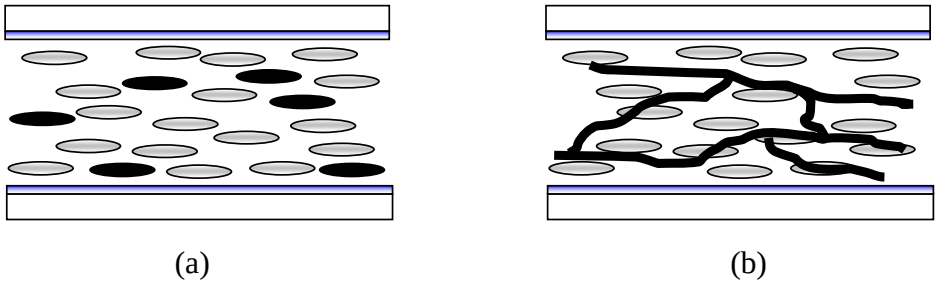

Figure 1.21. Schematic illustration of a polymer stabilized liquid crystal (PSLC) sample: (a) before curing and (b) after curing.

be proportional to the polymer concentration c, which implies that the polymer bundles are considered to be isolated objects. At high concentrations ($\sim$ 5-6 %), Kosseyev and co-authors showed the influence of the polymer network on electro-optical response is beyond the effective polymer field model and a virtual surface model is presented. In this model, the aligning effect of the polymer bundle is correlated.

1.3.3 Holographic Polymer-Dispersed Liquid Crystals

Holographic polymer dispersed liquid crystals (H-PDLCs) are a slightly evolved form of the photo-PIPS formed PDLC mentioned above. Two major differences distinguish the H-PDLCs: firstly, in H-PDLCs the liquid crystal droplets are significantly smaller than in PDLCs, typically on the order of $\sim$ 10 - 100nm, whereas droplets are typically micrometer-sized in PDLCs; secondly, the droplets in H-PDLCs are confined to well-defined planes, instead of randomly dispersed throughout the polymer binder. Light in the visible part of the spectrum has wavelength larger than the average droplet size in H-PDLCs and incoherent scattering from individual droplets is minimal. However, the arrangement of droplets in planes results in a periodic average refractive index change between the droplet-rich planes and polymer-rich planes, which coherently scatter light. Application of an electric field across an H-PDLC cell aligns the liquid crystal droplet

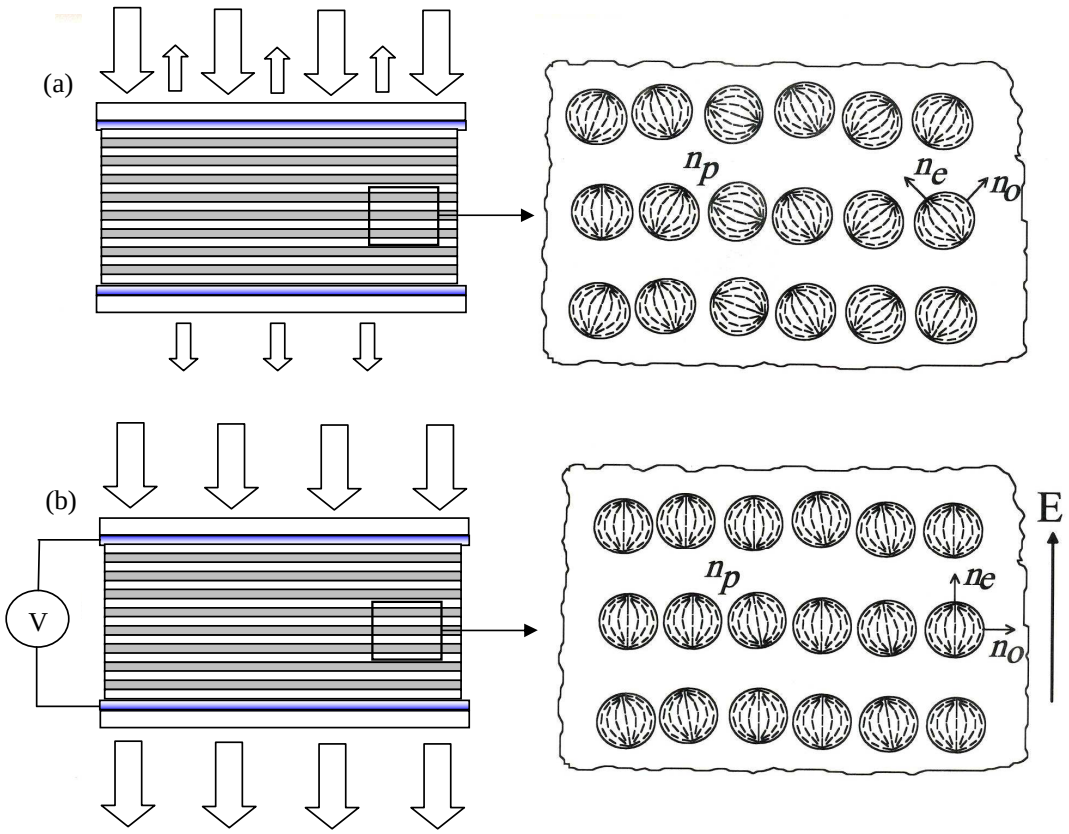

Figure 1.22. Illustration of a holographically formed PDLC in a reflecting mode (a) and in transparent mode (b).

directors and erases the refractive index modulation. In this case the material becomes completely transparent. Figure 1.22 shows the typical H-PDLC.

Switchable gratings formed in PDLCs were first investigated by researchers at Hughes Research Laboratories in 1988.[57, 58] Margerum and co-workers reported a patented switchable transmission grating formed by a masked exposure of UV-curable PDLCs. The anisotropic exposure resulted in a corresponding modulation of the droplet density and the corresponding index grating diffracted incident light. the index grating was erased on application of an electric field due to on-axis index matching on the droplets and polymer binder. Around the same time Ingwall and co-workers reported a

device formed by back-filling cured holographic Polaroid DMP film with a nematic liquid crystal.[59, 60] The photopolymer was swollen by the absorbed liquid crystal, which collected as droplets in voids in the planes with low polymer density. An applied electric field index-matched the droplets to the polymer and the index grating was erased. The fields required to switch these devices were extremely high and the multi-step fabrication was costly and slow.

In 1993, Bunning and co-workers reported the first switchable transmission gratings formed by a holographic anisotropic photo-PIPS process.[61, 62] Their work included the development of a materials set which was sensitive to visible wavelengths. Shortly thereafter, Tanaka and co-workers reported the first H-PDLC Bragg reflection gratings.[63] The high color purity, low form-factor and ease of formation immediately appealed to the flat panel display community as well as military and other commercial uses.

The potential of a simple and inexpensive switchable grating technology for device applications is great, however H-PDLCs are still in their infancy. A complete understanding of these materials requires an in-depth knowledge of polymer photochemistry, liquid crystal science, multi-phase composite and optical holography. Understanding of the parameters is critical to their formation and performance are limited and mostly derived from empirical studies and extrapolation of data from simple better-understood systems.

1.4 Holographic Principle

In conventional imaging technology the image is recorded on a photo-sensitive substrate such as silver salt. All information recorded on the film is the intensity (or amplitude) distribution with the information of relative phase of the electric field is absent. In 1948 Gabor proposed the idea of holographic imaging.[64] Holography is the process of recording the complete information of electric field both amplitude and relative phase

and consequently a real three-dimensional image can be reconstructed.[65] Since most recording materials are only sensitive to the amplitude of light, with few sensitive to polarization direction, it is necessary to convert the phase information to the amplitude information. The interference of two monochromatic and coherent beams is utilized to accomplish this task.

Interference is the superposition of two or more coherent waves resulting in a new wave pattern which was discovered by Young.[66] As most commonly used the wave pattern forms through the interference of waves with the same frequency (i.e. monochromatic waves). When two or more mutually coherent monochromatic waves are superimposed the intensity varies from point to point. The superimposed electric field of N beams is given by

$$\mathbf{E}_{tot} = \sum_{j=1}^{N} \mathbf{E}_j(\mathbf{r}) e^{-i\omega t} = \sum_{j=1}^{N} \mathbf{E}_j e^{i(\mathbf{k}_j \cdot \mathbf{r} - \omega t)} \tag{1.32}$$

The total irradiance is proportional to the time-average of the square amplitude of the electric field

$$\mathcal{I}(\mathbf{r}) \propto \langle \mathbf{E}_{tot} \cdot \mathbf{E}_{tot}^{*} \rangle = \frac{1}{2} \sum_{j=1}^{N} \sum_{l=1}^{N} \mathbf{E}_j(\mathbf{r}) \cdot \mathbf{E}_l(\mathbf{r}) \tag{1.33}$$

Many methods exist for the recording and playback of a hologram, and a simple experimental setup is shown in Figure 1.23. The essential elements of any holographic apparatus are a reference beam, and object beam, and a recording film. The reference beam serves as an unscattered background to illuminate the film. The object beam is reflected off of or transmitted through the subject of the hologram, and carries a wavefront containing all the information necessary to the three-dimensional reconstruction of the object image (see Figure 1.24 (a)). The film is photosensitive recording media, and may be either a thin (surface) of thick (volume) film. After exposure, the film is developed. The hologram can then be played back with a reference beam which includes the reference wavelength and is incident along the same path as the original recording beam, an image

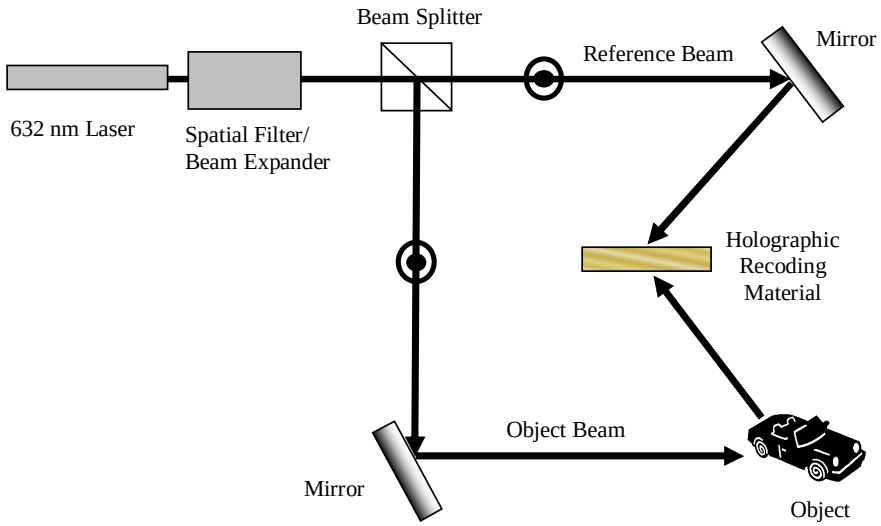

Figure 1.23. Basic experimental apparatus for the recording of a hologram.

of the object appears at the location where the original object was located (see Figure 1.24 (b)).

The ideal recording materials for holography should be sensitive to the recording laser wavelength. Many practical material sets have been used in holography such as silver halide emulsions, dichromated gelatins, photoresists and photopolymers.[67] Liquid crystal/polymer mixtures with small amounts of photoinitiators are also suitable to record holograms with high spatial resolutions ($\sim$ 100 nm) which is the thrust of this dissertation topic.

1.5 Summary

The properties of liquid crystal/polymer dispersions were discussed from the basic principles of liquid crystal and polymer physics. The goal of this dissertation is to study holographically patterned liquid crystal/polymer dispersions from both a physical and

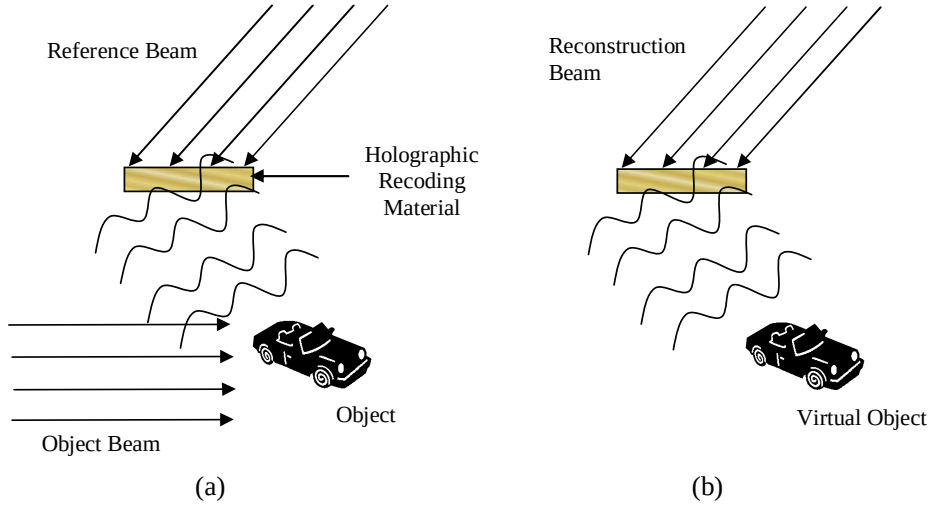

Figure 1.24. (a) The recording of a simple hologram, and (b) the playback of the hologram.

application perspective. Before proceeding to experimental results, topics concerning H-PDLCs will be covered in full in the next chapter.

CHAPTER 2

HOLOGRAPHIC POLYMER DISPERSED LIQUID CRYSTAL PROPERTIES

2.1 Holographic Polymer Dispersed Liquid Crystals: Modes of Operation

Holographic polymer-dispersed liquid crystals are active holographic elements fabricated in polymer dispersed liquid crystal materials. Usually a periodic planar structure is fabricated through an interference of two mutually coherent plane waves. The holographic exposure initiates photopolymerization resulting in a diffusion of liquid crystal to the dark regions of the the interference pattern and monomer diffusion into the bright regions of the interference pattern.[68] The monomer is subsequently polymerized thereby locking-in a periodic structure of alternating liquid crystal rich and polymer rich layers. the liquid crystal rich regions include randomly oriented sub-micrometer droplets. In some H-PDLC materials the liquid crystal droplets prefer to align along some particular direction. The size of liquid crystal droplets depends on a number of factors: most importantly exposure time, laser beam intensity, photoinitiator concentration and the concentrations of liquid crystal and polymer. The random orientation of symmetry axes of the liquid crystals ("off state") and the index of refraction mismatch between the liquid crystal droplets and the polymer matrix create a coherent scattering condition given the periodic nature of the morphology. This is in contrast to the incoherent scattering condition of a conventional PDLC where the droplets are randomly dispersed in the polymer matrix. The light can be reflected or diffracted efficiently by H-PDLCs. The optical properties of H-PDLC gratings can be electrically controlled since the liquid crystal droplets can re-orient under the influence of an external electric field. Specifically, if

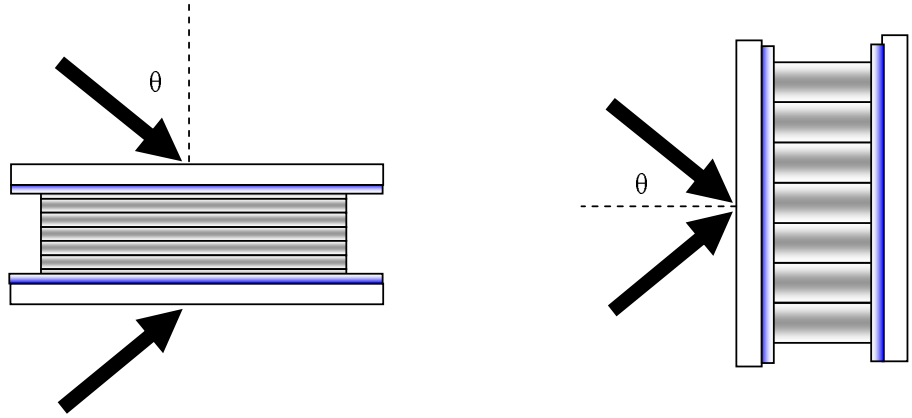

Figure 2.1. Holographic configurations for reflective (a) and transmissive (b) H-PDLCs.

the ordinary refractive index of the liquid crystal, n_o, matches the refractive index of the polymer, n_p, then the index modulation of H-PDLCs can be eliminated with a sufficient electric field creating a transparent state ("on-state"). Also any states between on and off are achievable. Depending on the geometries of the holographic apparatus there are two main categories of H-PDLCs, reflective and transmissive, as seen in Figure 2.1.

2.1.1 Two-Beam Interference

The interference of two linearly polarized plane waves with wavelength λ in a homogeneous dielectric medium can be written as

$$I(\mathbf{r}) = I_1 + I_2 + 2\sqrt{I_1 I_2}\cos(\Theta)\cos\left[(\mathbf{k}_1 - \mathbf{k}_2)\cdot\mathbf{r} + \phi\right] \tag{2.1}$$

$$= I_o\left(1 + V\cos\left[(\mathbf{k}_1 - \mathbf{k}_2)\cdot\mathbf{r} + \phi\right]\right) \tag{2.2}$$

where $\mathbf{k}_1$ and $\mathbf{k}_2$ are wave vectors, I_1 and I_2 are the intensities of the two beams, Ω is the angle between the polarization direction of the two beams, ϕ is the relative phase between the beams and $V = 2\cos(\Theta)\sqrt{I_1 I_2}/(I_1 + I_2)$ is termed the fringe constant of the interference.

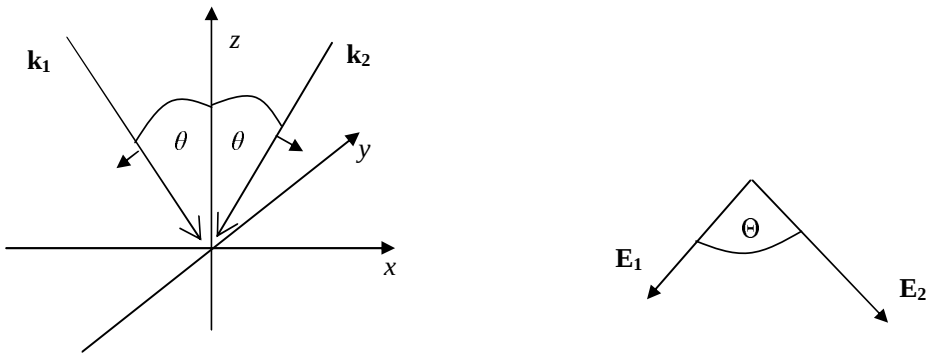

Figure 2.2. Geometry of two incident beams and associated polarizations.

If we define $\mathbf{k}_1$ and $\mathbf{k}_2$ to lie in the xz-plane symmetric about the z-axis as seen in Figure 2.2, the interference can be rewritten as

$$I = I_o\,(1 + V\cos(\Lambda x)) \tag{2.3}$$

where

$$\Lambda = \frac{\lambda}{2n\sin(\theta)} \tag{2.4}$$

is the period of the interference (pitch) and n is the refractive index of the medium. In principle the pitch Λ varies from $\lambda/2n$ to infinity.

2.1.2 Reflection Mode Holographic Polymer-Dispersed Liquid Crystals

Reflective holographic polymer-dispersed liquid crystals are stratified structures composed of liquid crystal rich and polymer rich layers parallel to the substrates, as seen in Figure 2.1 (a), which are recorded with the interference pattern of two counter-propagating beams. Tanaka and coworkers recognized the potential of PDLC materials in reflective displays and reported reflection mode Bragg gratings formed holographically in 1994.[69] A very narrow band of light ($\sim$ 20 nm) can be reflected from these reflective mode H-PDLCs. Tanaka and company proposed using H-PDLC materials as reflective full-color displays due to the high color purity and ease of formation. Three primary colors

(red, green and blue) can be fabricated using different wavelength lasers[69] or even the a single laser.[70] In order to achieve high efficiency and low scattering, tiny droplets of liquid crystal ($\sim$ 100 nm of less) are expected to be formed.[71] The optimization of exposure conditions has also shown that high intensity holographic exposure is desired to enhance phase separation.[72]

Ideally the pitch of H-PDLC gratings, Λ, captures the repetition of the interference

$$\Lambda = \frac{\lambda_W}{2n\cos(\theta_W)} \tag{2.5}$$

where θ_W is the incident angle inside the H-PDLC material, n is the average index of the material and λ_w is the laser wavelength. Based on Bragg's law, this reflective grating reflects light with the wavelength

$$\lambda_R = 2n\Lambda\cos(\theta_R) = \frac{\lambda_w\cos(\theta_R)}{\cos(\theta_w)} \tag{2.6}$$

where θ_R is the incident angle of the reading beam. Specifically, if the writing and reading beams are normally incident, the reflective wavelength is that of the writing laser. Practically, the reflection wavelength of this type of hologram is slightly less than the wavelength of the writing beam, which is due to effects of polymer shrinkage.[73] This phenomenon is generally true in other holographic materials as well.[67]

Normally there is no polarization dependence observed in reflection efficiency, which implies there is no preferred order of liquid crystal droplets in the holographic plane. The average refractive index of the liquid crystal can be written as

$$\bar{n}_{LC} = \sqrt{\frac{2n_o^2 + n_e^2}{3}} \tag{2.7}$$

Due to the fact that the phase separation is incomplete the average refractive index of the liquid crystal rich layers (n_{LC}) is slightly less than $\bar{n}_{LC}$. The index of polymer rich layers, (n_p is a function of the index of the polymer and $\bar{n}_{LC}$. The index modulation (n_1) is some

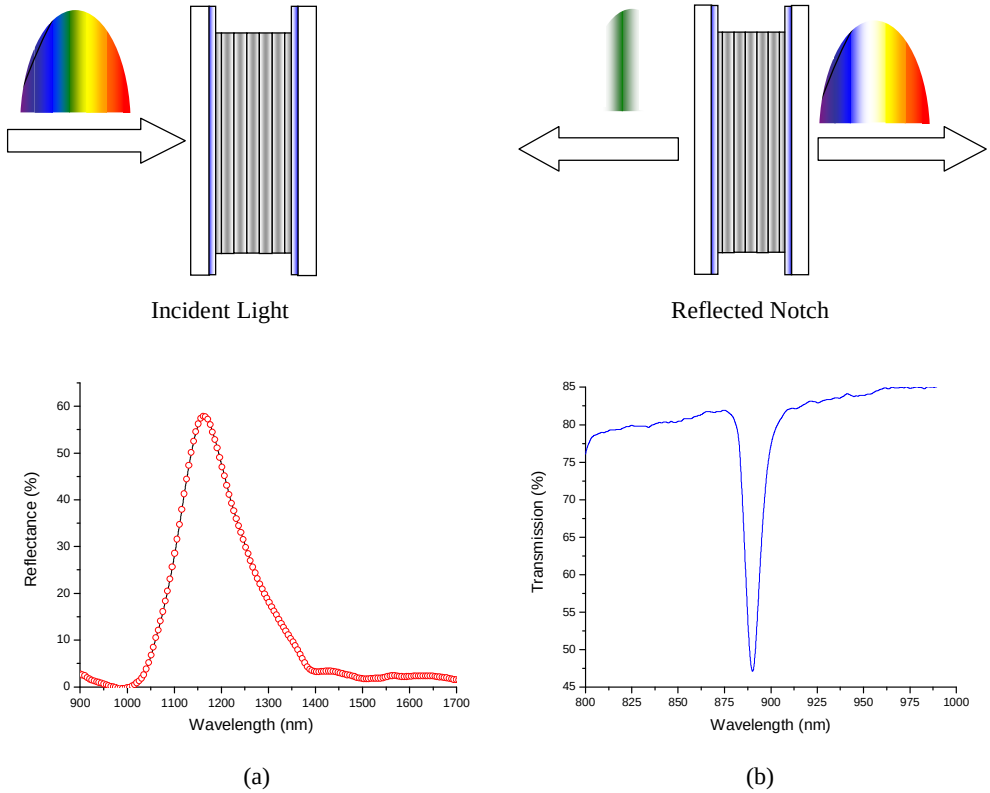

Figure 2.3. The operation of a reflective H-PDLC. (a) Reflection spectrum of a 10 μm sample fabricated via the 632 nm line of a HeNe laser. (b) The transmission spectrum of a different H-PDLC sample fabricated to reflect a different IR region.

fraction of $\bar{n}_{LC} - n_p$ (~ 0.1 for most H-PDLC material sets) and the typical value of n_1 is on the order of 10^{-2}. If the ordinary index of the liquid crystal, n_o, is approximately matched to the index of the polymer rich layers, n_p, this index modulation can be erased in less than a millisecond (typical values 200 μs) by applying a sufficient electric field to align the liquid crystal molecules and the material will be optically homogenous provided the dielectric anisotropy of the liquid crystal is positive ($\Delta\epsilon > 0$).[74]

In order to fabricate colored as well as IR holograms lasers having wavelengths of 632 nm and 670 nm were primarily utilized. In Figure 2.3 (a) an optimized reflection spectrum of an IR hologram with thickness 10 μm which is created *via* a 632 nm HeNe

laser is presented. The peak efficiency is $\sim 60\%$ and the width of the reflection band is approximately 180 nm. The reduced reflection efficiency and widening of the spectral notch is due to the relative thickness, (L/Λ), decreasing for longer pitch gratings as well as high angular incident writing angles. Narrower reflection bands can be achieved by reducing the liquid crystal load in the prepolymer mixture. Varying reflection wavelength can be obtained by adjusting the writing angle of the laser θ_W. The measured transmission spectra of an addition IR sample is shown in Figure 2.3 (b). Here The peak efficiency is $\sim 32\%$ and the width of the reflection band is approximately 14 nm.

By adjusting the material sets and exposure conditions, Bowley and co-workers demonstrated a variable wavelength reflector which can shift the reflection wavelength by applying a voltage.[75] The polymer rich layer refractive index n_p was chosen to be between n_o and n_{LC}. By applying an intermediate strength field, the index of liquid crystal rich layers n_{LC} matched n_p and the grating can be diminished. If the applied field is beyond this intermediated value n_{LC} becomes less than n_p and a shorter wavelength reflection grating is formed. Compared to other reflective H-PDLCs where n_p matches n_o, the variable reflector has a relatively low reflection efficiency. A reversible mode reflective H-PDLC can also be fabricated based on a similar idea.

An alignment-controlled reflective H-PDLC has been demonstrated by Kato and co-workers in NTT Corp in Japan.[76] Before holographic exposure, homogeneous alignment layers were coated on the glass substrates. In order to capture this alignment in the resulting H-PDLC gratings they used a mixture with a very high concentration of liquid crystal (66%) and some liquid crystal monomer (14%) which is expected to permanently lock the alignment. A slanted holographic geometry (14.5^o) was utilized to avoid specular reflections. The resulting H-PDLC reflected both polarizations of light very weak at zero-field (reverse mode). By applying an electric filed the H-PDLC reflected light parallel to the alignment direction with 70% reflectance on one polarization was obtained.

Even higher voltage reduced the efficiency since the index modulation was reduced. The application of this device is limited given the polarization selectivity.

2.1.3 Transmission Mode Holographic Polymer-Dispersed Liquid Crystals

In transmission H-PDLCs the holographic planes are perpendicular to the substrates which are created in the interference pattern of two propagating laser beams (See Figure 2.1 (b)). The pitch of the grating, Λ, is determined by

$$\Lambda = \frac{\lambda_W}{2n \sin(\theta_W)} \tag{2.8}$$

The typical pitch of transmission gratings which can effectively diffract visible light or near IR is 1 to 5 μm.

Figure 2.4 presents the operation principle of a typical transmission H-PDLC. In the filed-off state the grating strongly diffracts light which can be operated in Bragg of Raman-Nath regime depending on the pitch and thickness of the sample. Ny applying an electric field the diffracted order can be diminished. The direct application of transmission H-PDLC is an active beam steering or optical switch.[77, 78, 79, 80] Sutherland and co-workers first reported the fabrication of high efficiency ($\sim$ 50% - 80%) transmission H-PDLCs in the Bragg regime.[81] They utilized the 514 nm line of Ar^+ laser to sensitize their materials. The resulting liquid crystal droplet size was ≤ 0.2 μm and the gratings could be modulated with a field as low as 11 V/μm. From the diffraction efficiency they estimated an index modulation (n_1) of around 1 x 10^{-2}. Due to this relatively small index modulations narrow angular selectivity ($\sim 1^o$) was observed.

Compared to reflective H-PDLCs, most transmission H-PDLC are polarization sensitive. This was reported and commented on by Sutherland et al.[82] Compensating the coupling coefficient difference for TE and TM waves they found that TM waves (see section on 2.4.2) have a slightly larger effective index modulation. This indicates the liquid

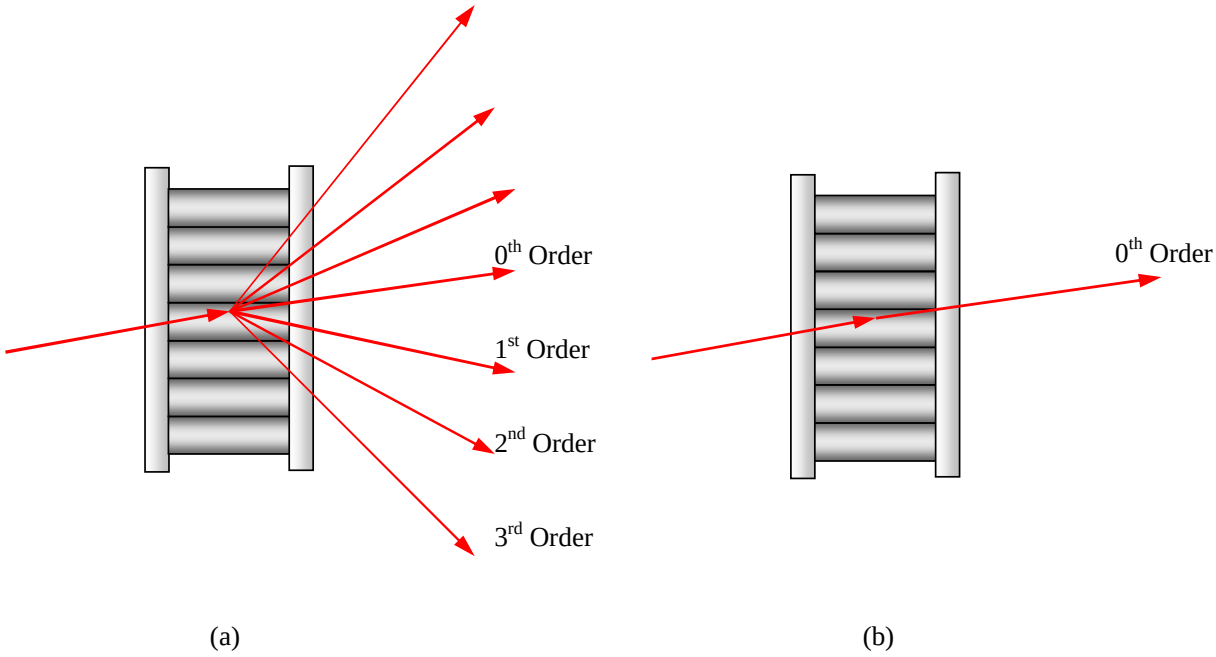

Figure 2.4. Schematic illustration of a transmission mode H-PDLC in the "on-state" (a) and "off-state" (b).

crystal droplets are optically anisotropic and hove some orientational order perpendicular to the holographic planes. This polarization dependence has also been observed in other material set.[83, 84, 85, 86]

Jazbinsek and co-workers investigated and characterized the dielectric anisotropy of liquid crystal droplets in transmission mode H-PDLCs.[87] Through the use of SEM they found ellipsoid shaped droplets formed in liquid crystal rich planes. By fitting their experimental data on diffraction efficiencies of polarized light to coupled wave theory in anisotropic medium they found that the index modulation along the grating vector is higher and the dielectric anisotropy is higher in short pitch H-PDLCs.

In some material sets the liquid crystal is highly aligned along some specific direction which results in H-PDLC transmission gratings diffracting only one polarization of light. A phenomenological polymer scaffolding model was presented by Vardanyan and

co-workers to explain this orientational order of liquid crystals and electro-optic response of the H-PDLCs.[85] In this model, polymer scaffoldings, which may be formed in incomplete phase separation and connect the holographic planes, strongly align the liquid crystal molecules homogeneously in liquid crystal rich planes. Effectively a polymer field forms and influences the electro-optic response and optical anisotropy of the system. The reason that the scaffoldings are along the grating vector direction is unclear. The anisotropic diffusion process could be the answer.

To fabricate a polarization-insensitive diffraction device for practical applications such as telecommunications is essential. Boiko and co-workers demonstrated a stacked H-PDLC device which diffracts both TE and TM waves efficiently.[86] This device consists of a passive polarization rotator device sandwiched between two independently address H-PDLC gratings. The single transmission H-PDLC which was fabricated had a high diffraction efficiency contrast of TM and TE light ($\sim$ 30%) at 1550 nm. The passive polarization-rotator is created from a reactive mesogen film. The thickness of the polarization rotator can be optimized for a particular wavelength of light to achieve $\pi/2$ polarization rotation, Thus the unperturbed TE wave is converted to TM waved and it can be diffracted efficiently by the second grating. After the stacked device, the diffraction efficiency for unpolarized light can be as high as 98%. Since both H-PDLC gratings are independently addressed this device is also able to selectively switch only one polarization.

Fuh and co-workers investigated a polymer-ball-type H-PDLC which was created through a high liquid crystal load prepolymer mixture with additional azo dye.[88, 89] Compared to conventional H-PDLCs containing liquid crystal droplets the polymer-ball-type H-PDLCs involve the polymer balls in a continuous liquid crystal matrix. The polymer-ball-type H-PDLC gratings were created through a two-step polymerization process. First a UV exposure is used to make a PDLC film. Then the PDLC film is exposed

to high intensity visible interference pattern ($\sim 2\text{W/cm}^2$). The absorption band of the azo dye covered the wavelength of the viable laser.[89] The resulting grating has a strong polarization dependence on the writing beam. At zero-field state, the H-PDLC looks opaque from strong scattering. The scattering effect of TM waves is much stronger than that of TE waves and no transmitted beam is observed. The TE wave can be diffracted weakly. These gratings can be switched under very low fields (2.5 V/μm) due to the high load of liquid crystal. They also observed these gratings have a memory effect on the polarization of the witting beams which is attributed to the absorption of azo dye doped in PDLC materials. This polymer-ball-type grating is not suitable for reflection applications since the scattering loss is much stronger than other materials.

2.1.4 Reflection Mode Holographic Polymer-Dispersed Liquid Crystals

Conventional H-PDLC technology allows for electric field effects to diminish or completely remove the index modulation, (Δn), allowing for little to no diffraction to occur. With subsequent removal of the applied electric field the index modulation returns and diffraction effects are restored. Very little research has been done on the so-called "reverse-mode" operation of H-PDLC gratings.[90, 91] In which the diffraction efficiency increases as a result of the applied electric field. The realization of a reverse-mode diffraction grating requires the use of liquid-crystalline diacrylates, or better known as reactive mesogens. Much work has been done on the study of reactive mesogens and their use via bulk polymerization processes.[92, 93, 94, 95] Instead of flood lit polymerization, one could utilize novel holography methods and with the ability to control alignment of reactive mesogens via rubbed substrates these materials can allow for reverse mode operation of an H-PDLC. When the photopolymerization is induced by interfering coherent beams (holographic method), a diffractive grating is produced with regions of constructive interference becoming fixated by polymerization and regions of destructive

interference remaining a fluid like monomer. Upon application of an electric filed, the monomeric regions will align with the field, increasing Δn to approximately the birefringence of the reactive mesogen. This increase in Δn will produce a corresponding increase in diffraction efficiency and thus a reverse-mode H-PDLC.

2.2 Holographic Polymer Dispersed Liquid Crystals: Materials

A fundamental aspect of liquid crystal/polymer research is the development of materials. At first glance, one needs only to combine ingredients following a given recipe. In essence, this is an accurate description, however, the difficult part comes when we try to create a new recipe. There are certain techniques that are required to produce a good mixture, and certain key ingredients to making it perform. All formulations have two underlying components: monomer and liquid crystal. In addition, a material set may include a photoinitiator dye, co-initiator, surfactant, and/or solvent. The ratios of these components, and in fact the presence of the components at all, is determined through optimization methods. All of the monomers used in H-PDLCs allow for photopolymerization, however each one has its own absorption curve. To compensate for absorption curves that fall outside the laser wavelength, a photoinitiator dye combined with a co-initiator allows free radical polymerization to occur. We set out to develop a system that would utilize the 632.8 nm line of the HeNe laser as well as the 670 nm line of the common red diode laser. The systems components were formulated empirically with the constitutes that are discussed in the next few sections with results discussed in detail in Chapter 3.

2.2.1 Liquid Crystal Materials

The prepolymer syrups used in H-PDLC formation are mixed from several components, most of them being commercially available. Nematic liquid crystal materials with

a high birefringence and a positive dielectric anisotropy are typically used for normal operational mode H-PDLCs. A high birefringence gives the greatest possible refractive index modulation between the polymer and liquid crystal droplet layers forming the grating structure. This is important for maximizing grating efficiency. A large dielectric anisotropy is desired to minimize the drive voltage. Also, the liquid crystal should exhibit a nematic phase that is stable over a sufficient temperature range that any device application may be utilized. A list of commonly used liquid crystal materials used for H-PDLC technology, with some specifications are shown in Table 2.1

Table 2.1. Liquid crystal materials commonly utilized for H-PDLCs

Liquid Crystal	Δ n	n_o	$\Delta\epsilon$	T_{NI}
E7	0.2253	1.5211	+13.8	58^{o}C
BL038	0.2720	1.5270	+16.4	100^{o}C
TL205	0.2175	1.5270	+5.0	87^{o}C

The liquid crystal materials listed in Table 2.1 are eutectic mixtures. These are mixtures of several liquid crystal compounds mixed in the appropriate ratios so as to maximize the nematic temperature range of the material. E7, for example, is composed of four different liquid crystal molecules. These are seen in Figure 2.5. Eutectic liquid crystals further complicates the photo-induced polymerization process given that some of the liquid crystal compounds may have a better solubility in the polymer binder than others. The phase separation process can lead to a separation of the individual liquid crystal components. This has been observed in PDLCs[96], but has not been investigated in H-PDLCs. Smectic liquid crystals have also been reported in H-PDLC materials.[97] Date and co-workers, using liquid crystals with a smectic A phase, reported a film that was electrically writable and thermally erasable.

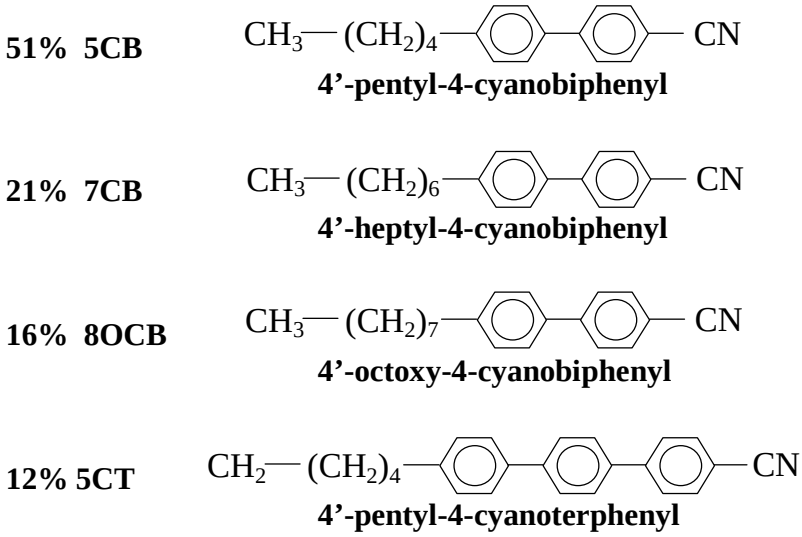

Figure 2.5. Constituents of the eutectic nematic liquid crystal E7.

Liquid crystal loadings are significantly smaller in H-PDLC prepolymers than in PDLC systems. This is due to a significantly smaller desired droplet volume fraction in H-PDLCs. An ideal H-PDLC, assuming that the liquid crystal must be confined to discrete droplets, is composed of a single layer of close-packed spherical droplets in alternating planes adjacent to planes of equal thickness consisting only of the polymer binder. The diameter of the droplets extends the depth of the plane. For such a geometry the volume fraction, v_{plane}, of the spheres in the plane is given by

$$v_{plane} = \frac{\pi}{3\sqrt{3}} \tag{2.9}$$

The volume fraction of droplets in the film is half this, or

$$v = \frac{\pi}{6\sqrt{3}} \tag{2.10}$$

$$v = \approx 30 \tag{2.11}$$

This volume fraction turns out to be the same for close packed ellipsoids with semi-major axis aligned. H-PDLCs are thus prepared with approximately a 30% liquid crystal

loading. This is contrasted with an 80% loading for PDLC systems. H-PDLC materials sets, optimized empirically, usually contain slightly less than 30% liquid crystal by weight, as some residual liquid crystal remains in the swollen polymer binder.

2.2.2 Monomers and Oligomers

The chemical nature of the polymers used in H-PDLC materials is extremely important to many aspects of H-PDLC formation and performance. The type of monomer dictates the polymerization mechanism (i.e. step-growth or chain-growth), which determines the formation kinetics (i.e. liquid-liquid or liquid-gel demixing) and the film's morphology. In addition, the type of polymer affects the liquid crystal/polymer interaction which dictates the miscibility of the liquid crystal in the polymer and the liquid crystal anchoring to the polymer binder which effects electro-optical performance.

Thiol-ene and acrylate chemistries have been the most heavily applied photopolymerization processes in H-PDLC film formation. Thiol-ene based systems are usually employed with the commercially available optical adhesives form Norland Products, such as Norland Optical Adhesive NOA-65. These have been extensively used in PDLC systems and consists of a mixture of trimethylolpropane diallylether, trimethylolpropane tristhiol, isophorone disocyanate ester and benzophenone as a photoinitiator.[98]

Acrylate chemistries are probably more widely used in H-PDLC systems. Usually a multifunctional acrylate is used to provide crosslinking between the polymer chains. Functionality plays an extremely important role in polymerization kinetics and the mechanical properties of the cured polymer matrix. This is discussed for our HeNe formulation in section 3.1 of this dissertation. Early H-PDLC systems used the pentaacrylate monomer dipentacrythritol hexa-/penta-acrylate (DPHPA).[82] Also, improved performance using blends of mixed functionality urethane resins has been demonstrated.[99] A list of chain-polymerizable acrylate monomers more commonly utilized is seen in Table

Table 2.2. Monomers commonly used for H-PDLC prepolymers

Monomer	**Functionality**	**Supplier**
DPHPA	5	Sigma-Aldrich
SR399	5	Sartomer
SR295	5	Sartomer
CN135	1	Sartomer
Ebecryl 4866	3	UCB Radcure
NOA65	3	Norland

2.2. All these materials have a refractive index of $n_p \approx 1.5$. Karasawa and Taketomi reported a significant dependance of the polarization dependance of H-PDLC transmission gratings on polymer chemistry.[100] They investigated a number of different polyester-based and urethane-based systems and found a broad variance in the diffraction properties of similarly prepared films. They speculated that the difference in polarization dependance between formulations was due to different anchoring conditions at the liquid crystal/polymer interface.

In all acrylate systems the co-monomer 1-Vinyl-2-Pyrrolidone (NVP) is also included. This monofunctional monomer is referred to as both a chain-extender[101] and a crosslink promoter[82]. NVP dramatically affects the reaction rate of photocured acrylate polymers, suggesting that it may behave as an oxygen scavenger (oxygen inhibits the polymerization reaction). Bunning and coworkers investigated the effect of varying the amount of NVP in their formulations.[82] They reported that reducing NVP increases gelation times and increases the size of the liquid crystal droplets, consistent with slowing reaction rates. NVP is also an excellent solvent which facilitates ease of mixing of the prepolymer materials.

2.2.3 Photoinitiators and Coinitiators

A photoinitiator is required to sensitize the prepolymer syrup to the wavelength of the laser radiation used in the anisotropic photoinduced polymerization process. For this purpose methylene blue is employed into the mixture for sensitizing to the 632 nm wavelength of the HeNe laser. The absorption peak of methylene blue is shown in Figure 2.6 with a peak absorption band occurring at 670 nm. The blue color bleaches out during the laser exposure, however residual dye can be detrimental to the performance of the H-PDLC, giving the film a distinctive blue hue. More importantly, the long-term photostability of photopolymerized system is a concern due to the presence of unreacted photoinitiators. Photoinitiator which are not consumed in the polymerization process can produce free radicals at later times which can degrade the polymer and liquid crystal over time. Photoinitiators may also remain dissolved in the liquid crystal, suppressing the clearing temperature and further degrading the electro-optical properties of the H-PDLC.

Initiation of free radical polymerization requires a coinitiator in conjunction with the photoinitiator. The coinitiator n-Phenylglycine (NPG) or p-toluensulfinic acid are used with methylene blue. The initiator and coinitiator are usually dissolved in NVP and then mixed with the desired liquid crystal/monomer system. On exposure to HeNe laser, photoabsorption by the photoinitiator methylene blue results in an excited triplet state followed by fluorescence or intersystem crossing to the triplet state. The methylene blue triplet functions as an electron donor, producing an NPG or p-toluensulfinic acid radical. Free radical polymerization is then initiated by this radical. The polymerization reaction proceeds and is dependant on the local radiation intensity and photoinitiator and coinitiator concentrations.

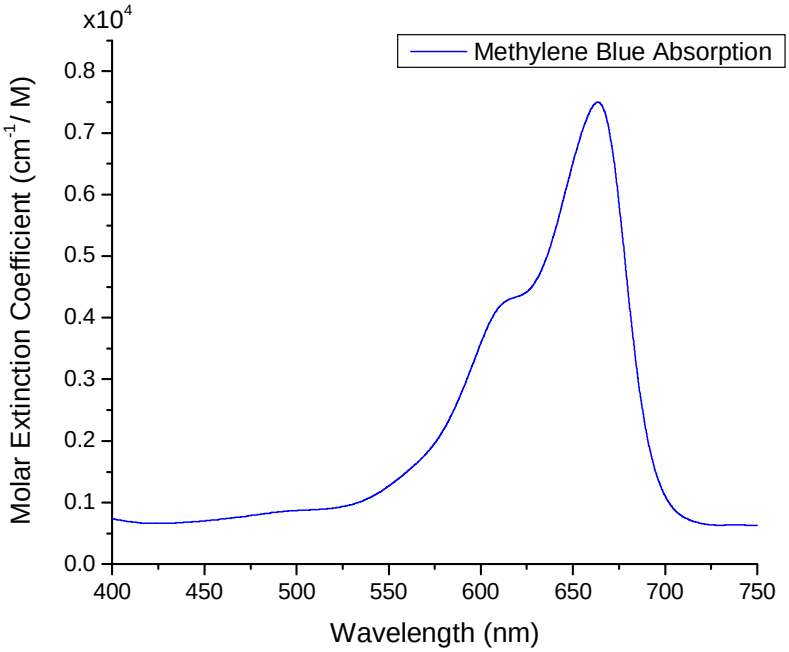

Figure 2.6. The absorption spectrum of the photoinitiator Methylene Blue.

2.3 Holographic Polymer Dispersed Liquid Crystals: Formation Kinetics

The formation kinetics of H-PDLCs has attracted a lot of attention recently. The understanding of formation mechanisms is important in the fabrication of high performance H-PDLCs. Several authors have studies this subject using *in-situ* measurements of diffraction efficiency of transmission H-PDLCs.[102, 103, 104, 105, 106] A typical in-situ experiment to monitor the formation kinetics of transmission H-PDLCs is seen in Figure 2.7. During the formation of a transmission grating the diffraction of a probing beam with a wavelength which is not sensitive to the H-PDLC material is monitored by a detector. Normally the direction of the probing beam is set to meet the Bragg condition. The intensity of the first order diffracted beam is recorded as a function of exposure time.

Before the invention of H-PDLCs the formation of holographic gratings in photopolymer systems was studied by Carre and co-workers.[107] They found there were

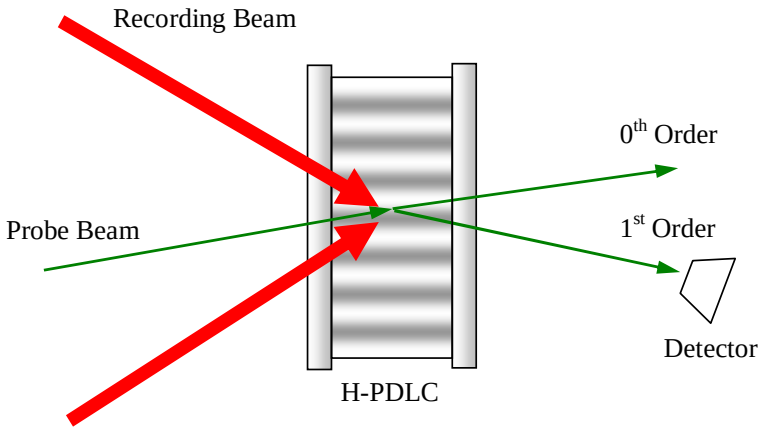

Figure 2.7. Illustration of an *in-situ* experimental setup to monitor the formation kinetics of H-PDLCs.

three main regions during formation: (1) a short induction period without photopolymerization until all inhibitors have reacted, (2) fast photopolymerization with increasing diffraction efficiency and bleaching of dyes, and (3) a plateau of diffraction efficiency when the photo-oxidant dye (photoinitiator) is irreversibly bleached. The similar behavior of transmission H-PDLC grating formation was first observed by Sutherland and co-workers.[82] The induction period was quite short and measurable diffraction efficiency could be observed 250 ms after exposure. In the first 30 seconds the diffraction efficiency was nearly zero which was explained as the nucleation time for phase separation. After that the diffraction efficiency rapidly increase to $> 25\%$ in 50 seconds. The time of rapid rise in diffraction efficiency was involved with the growth and final development of periodic liquid crystal domains. The reaction was terminated after about 100 s by blocking the recording beam. Shortly after the diffraction efficiency increased slightly and then attained a plateau. Sutherland and co-workers explained this by the fact that polymer chains will continue to grow in the dark before they terminate by radical trapping or interaction with another radical.[82]

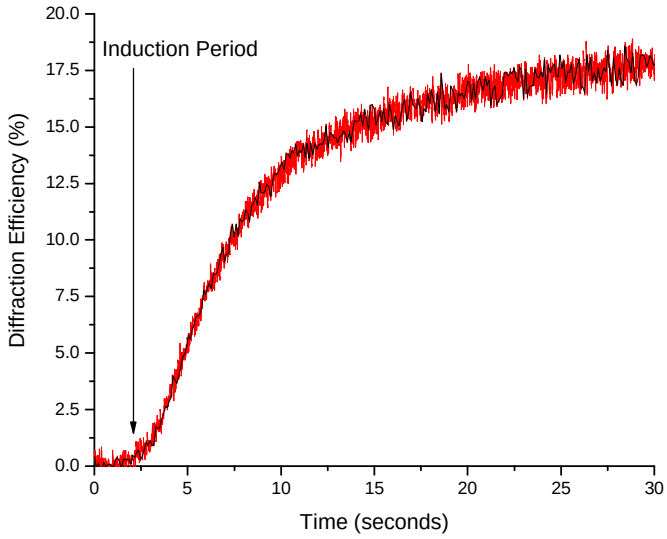

Figure 2.8. Example of diffraction efficiency vs. cure time for a sample cured utilizing HeNe interference pattern.

An example of the measured diffraction efficiency during grating formation is shown in Figure 2.8. Here, $t = 0$ corresponds to the start of the exposure of the sample to HeNe interference pattern. We see an initial induction period, corresponding to the time during which all reaction inhibitors (e.g. oxygen) have reacted. The diffraction intensity is then seen to increase dramatically as the rapid free-radical polymerization reaction takes place and the monomers and liquid crystal diffuse into the bright and dark fringes respectively. In some cases a distinct kink in the growth curve is observed, corresponding to the onset of phase separation. This marks an increase in the rate at which the diffraction efficiency increases. This increase, corresponding to an increase in the refractive index modulation of the grating, is most likely due to the onset of a nematic phase in the liquid crystal and depletion of liquid crystal from the monomer binder characteristic of PIPS process by nucleation-growth mechanisms.[108] The diffraction efficiency then plateaus as the polymerization reaction terminates and formation kinetics ceases. In some cases the

diffraction efficiency peaks and then decreases as the liquid crystal droplets grow large enough to scatter light.

2.3.1 Formation Theory

H-PDLC prepolymer materials consist of reactive monomers and inert low molecular weight liquid crystals (see section 2.2.1). The monomers are usually sensitized to the laser wavelength by the addition of a photoinitiator and is necessary a coinitiator. The prepolymer is typically a homogeneous, isotropic liquid prior to exposure. Irradiation to an intensity grating initiates a photopolymerization reaction in the sample. The rate of polymerization for a free radical reaction is proportional to the square toot of the intensity.[47] The reaction rate will thus be highest in the bright interference fringes, and the polymer chains will increase rapidly in these regions. Monomers are rapidly depleted in these regions and a monomer concentration grating is established, resulting in the diffusion of monomers from the dark fringes into the bright fringes. As the molecular weight of the polymer chains in the bright fringes increases, the chemical potential of the liquid crystal in these regions increases and the liquid crystal diffuses into the dark fringes as a result.

The highly crosslinked, rapidly growing network form a continuous network in the bright regions. This continuous network is know as a gel and the time at which it occurs is the gel point ($t = t_{gel}$). This is also characterized by a divergence in the viscosity of the polymerization product. This does not imply that diffusion, and thus the polymerization reaction, ceases entirely, as yet unreacted monomers, oligomers and the liquid crystal is still able to diffuse through the network. As the cure continues the sol-gel system is driven into a region of the phase diagram in which a single phase system is no longer stable. At this point phase seperation of the liquid crystal occurs ($t = t_{ps}$). In conventional PDLCs the free energy would now be minimized by a separation into two phases. However, in

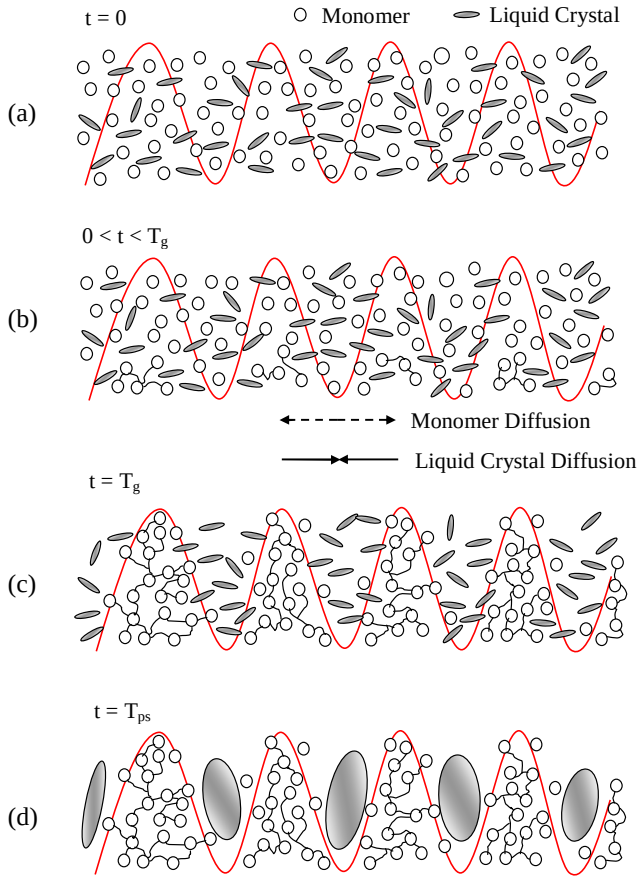

Figure 2.9. Illustration of H-PDLC formation. On exposure, (a), prepolymer is homogeneous. Monomers diffuse into the bright fringes and liquid crystal is forced into the dark fringes, (b). A continuous network marks the gel point, (c). Phase separation takes place in a liquid-gel demixing process, (d), as the cure deepens.

H-PDLCs the volume fraction of liquid crystal is significantly greater in the dark fringes than in the bright. Phase separation occurs exclusively in the dark fringes where liquid crystal droplets form. This process is illustrated schematically in Figure 2.9.

2.3.2 Diffusion Model

Bowley and co-workers were the first to rigorously solve a reaction-diffusion model numerically to understand the formation kinetics of transmission H-PDLC is visible materials.[68] The following discussion is in the spirit of this reaction-diffusion model.

The reaction-diffusion model assumes that there is a built-in concentration gradient inside the H-PDLCs during the photopolymerization process which induces diffusion of oligomers to bright regions of the interference pattern. Subsequently the liquid crystal molecules counter-diffuse to dark regions of the interference pattern (see Figure 2.9). The spatio-temporal mass density of each oligomer, ϕ_i^m, is governed by the differential equation

$$\frac{\partial \phi_i^m(z,t)}{\partial t} = \frac{\partial}{\partial z}\left(D_i(z,t)\frac{\partial \phi_i^m(z,t)}{\partial z}\right) - F_i(z,t)\phi_i^m(z,t) \tag{2.12}$$

which is the Fick's law modified with a photopolymerization term. $F_i(z,t)$ is the local polymerization rate for each monomer which is related to various parameters, such as the local light intensity, effective functionality and photoinitiator concentration. $D_i(z,t)$ is the local diffusion constant for each monomer/oligomer. It is assumed to be a function of space and time since the growing polymer network will affect the diffusion behavior of the monomers/oligomers. Similarly the reaction equation of polymer concentration ϕ_i^p is given by

$$\frac{\partial \phi_i^p(z,t)}{\partial t} = F_i(z,t)\phi_i^m(z,t) \tag{2.13}$$

The empirical expression

$$D_i(z,t) = D_{i0}e^{-\sum_i \alpha_i \phi_i^p(z,t)} \tag{2.14}$$

is utilized since the diffusion constant can be changed several orders during polymerization.[109] The expression describes the evolution of the diffusion constant, which describes the effect of the increased inhibition of diffusion of each oligomer through the increasingly dense polymer network. D_{i0} is the diffusion constant of the pure monomer. Both D_{i0} and the decay constant, α_i, are strongly dependant on the molecular weight of the monomer.

The photopolymerization reaction rate is also determined from an empirical formula given by

$$F_i(z,t) = I(z)k_{Ri}(f, M_w)e^{-\sum_i \alpha_i \phi_i^p(z,t)} \tag{2.15}$$

Here f is the oligomer functionality and M_w the molecular weight for reactive species i, and k_R is the characteristic rate coefficient of each monomer that depends on the ratio of the free monomer polymerization rate to the polymeric chain termination rate. The reactive-diffusion model threats k_R as a phenomenological fit parameter. The exponential term in $F_i(z,t)$ gives the same spatio-temporal dependence as the diffusion constant, as the reaction is expected to be diffusion limited. The reaction rate is also proportional to the local intensity of the interference pattern, given by

$$I(z) = I_o\left(1 + V\cos(Kz)\right) \tag{2.16}$$

where $I_o = I_1 + I_2$, with I_1 and I_2 the intensity of each individual beam and V is the fringe visibility (contrast). V is taken taken normally to be between 0.4 - 0.8 to account for any "dark polymerization." K is the grating vector. For one-photon polymerization instead of proportional to the intensity, I_o, the polymerization rate is expected to be proportional to the square root of the exposure intensity.[110]

The liquid crystal molecules are expected to counter-diffuse to the dark regions of the interference pattern. The liquid crystal molecules, having significantly lower molecular weight than the monomer/oligomers, are know to have a larger diffusion constant ($D_{LC} \sim 10^{-7}$ cm^{2}s^{-1}) than the monomer/oligomers, and the diffusion time steps taken to describe the monomer redistribution are considered infinitely long for the liquid crystal. The liquid crystal redistribution is thus governed by local volume conservation, which can be mathematically expressed as

$$\phi^{LC}(z,t) = 1 - \sum_i \left[\phi_i^m(z,t) + \phi_i^p(z,t)\right] \tag{2.17}$$

This kinetic model determines the dynamic spatial composition profile of an H-PDLC prior to phase separation. The refractive index profile can be determined as

$$n(z,t) = \langle n_{LC}\rangle\phi^{LC}(z,t) + \sum_i \left[n_m\phi_i^m(z,t) + n_p\phi_i^p(z,t)\right] \tag{2.18}$$

where n_p and n_m are, respectively, the polymer and oligomer indices, and $\langle n_{LC} \rangle = (2n_o + n_e)/3$.

When the interference pattern is 2D/3D it will generate a 2D/3D diffusion process and the formation kinetics can be described by a set of 2D/3D diffusion equations:

$$\frac{\partial \phi_i^m(\mathbf{r},t)}{\partial t} = \nabla \cdot [D_i(\mathbf{r},t) \nabla \phi_i^m(\mathbf{r},t)] - F_i(\mathbf{z},t)\phi_i^m(\mathbf{r},t) \tag{2.19}$$

and

$$\frac{\partial \phi_i^p(\mathbf{r},t)}{\partial t} = F_i(\mathbf{r},t)\phi_i^m(\mathbf{r},t) \tag{2.20}$$

This model has been employed to describe the formation of a transverse 2D photonic crystal in H-PDLC materials and estimate the liquid crystal droplet order parameter.[111]

2.4 Holographic Polymer Dispersed Liquid Crystals: Light Propagation

In classical electromagnetic theory the state of electromagnetic excitations is described by two vectors, the electric field **E** and the magnetic induction **B**. The motion of equation of these two vectors is governed by Maxwell's equations[112]

$$\begin{aligned} \nabla \times \mathbf{H} - \frac{1}{c}\frac{\partial \mathbf{D}}{\partial t} &= \frac{4\pi}{c}\mathbf{j} \\ \nabla \times \mathbf{E} - \frac{1}{c}\frac{\partial \mathbf{B}}{\partial t} &= 0 \\ \nabla \cdot \mathbf{D} &= 4\pi\rho \\ \nabla \cdot \mathbf{B} &= 0\mathbf{j} \end{aligned} \tag{2.21}$$

where **D** and **H** are the vectors of electric displacement and the magnetic field. ρ and **j** are the local charge and current densities.

To allow for the determination of the field vectors **E** and **B**, a set of material equations is necessary to be considered

$$\mathbf{j} = \sigma \mathbf{E}$$

$$\mathbf{D} = \epsilon \mathbf{E} \tag{2.22}$$

$$\mathbf{B} = \mu \mathbf{H}$$

Here σ is the conductivity, ϵ is the dielectric constant and μ is the magnetic permeability. Generally speaking, these parameters related to material properties are tensors and functions of $\mathbf{E}$ and $\mathbf{B}$. In dielectric materials, σ is negligibly small.

If the material is homogeneous and there is no free current and charge in the material, i.e. $\mathbf{j} = 0$ and $\rho = 0$), the Maxwell's equations can be transformed to the wave equations

$$\nabla^2 \mathbf{E} - \frac{\epsilon\mu}{c^2} \frac{\partial^2 \mathbf{E}}{\partial t^2} = 0 \tag{2.23}$$
$$\nabla^2 \mathbf{H} - \frac{\epsilon\mu}{c^2} \frac{\partial^2 \mathbf{H}}{\partial t^2} = 0$$

These equations indicate light (electromagnetic wave) propagates with the velocity

$$v = \frac{c}{\sqrt{\epsilon\mu}} \equiv \frac{c}{n} \tag{2.24}$$

in the dielectric medium. Here $n = \sqrt{\epsilon\mu}$ is the index of refraction of the medium. For nonmagnetic materials, the magnetic permeability μ is close to unity. Clearly the monochromatic plane wave

$$\begin{pmatrix} \mathbf{E} \\ \mathbf{H} \end{pmatrix} \propto e^{i\mathbf{k}\cdot\mathbf{r} - \omega t} \tag{2.25}$$

is a solution of equation (2.23). Here $\mathbf{k} = 2\pi n/\lambda \hat{\mathbf{k}} \equiv n k_o \hat{\mathbf{k}}$ is the wave propagation vector and $\omega = kc/n(\omega)$, which is the dispersion relation of the dielectric medium. By the zero divergence of D and B there are only two independent polarizations (*transverse* modes) even though the fields are three-dimensional vectors.[112]

Strong diffraction always occurs when the amplitude or phase of light is spatially periodically modulated on a scale which is comparable to the wavelength of light. This can be realized in two ways: spatially modulated absorption coefficient or spatially modulated

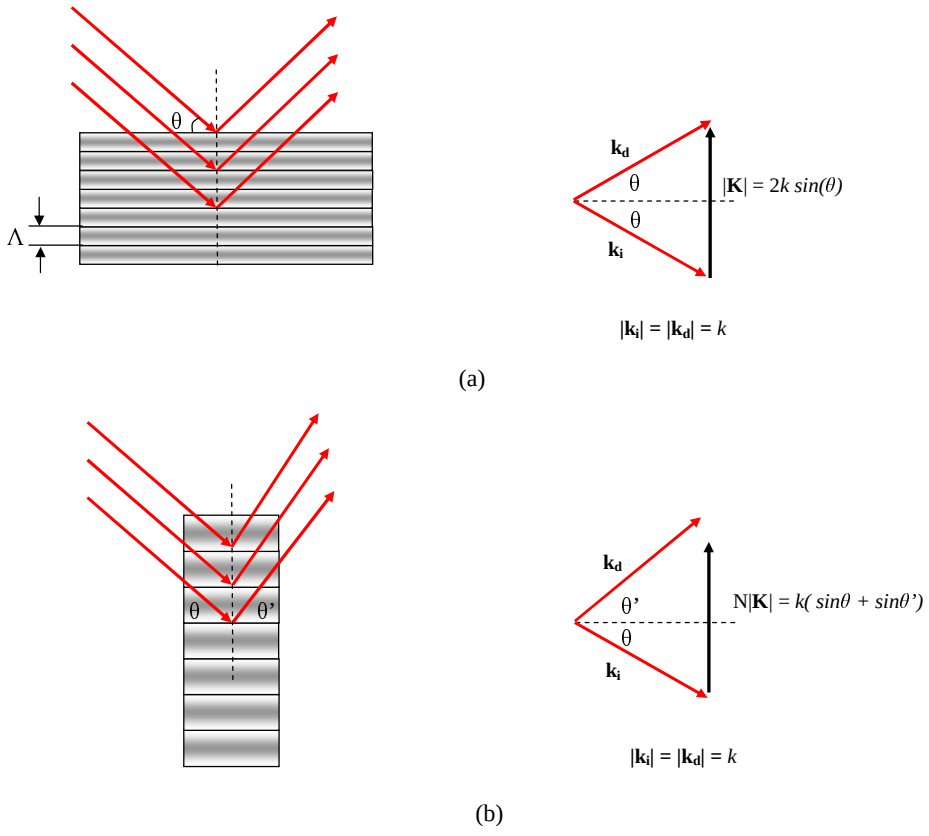

Figure 2.10. Diffraction of a monochromatic plane wave from a 1D volume grating (a) and a thin grating (b). The component of momentum perpendicular to the grating vector **K** is conserved in both cases.

optical path (modulated refractive index or thickness). The corresponding structures are called amplitude and phase gratings. The focus of this dissertation is on high efficiency diffraction elements, namely H-PDLC diffractive gratings. For this reason, we will focus our attention on transparent media and only on lossless phase gratings will be discussed.

For a one-dimensional phase grating the variation in the index of refraction can be expressed as a Fourier series

$$n(z) = n_o + \sum_{k=1}^{\infty} n_k \cos\left(\frac{2k\pi z}{\Lambda}\right) \tag{2.26}$$

where Λ is the spatial period or the pitch of the grating. If the refractive index modulation parameters n_k are much smaller than the average refractive index n_o the plane wave solution is still a good approximation to the wave equation.

For most cases it is sufficient to consider only the first Fourier component of the modulation such that

$$n(z) = n_o + n_1 \cos\left(\frac{2k\pi z}{\Lambda}\right) \tag{2.27}$$

The typical value of n_1 is of the order 10^{-1} to 10^{-3}. Figure 2.10 (a) shows the diffraction from a 1D *volume grating*. We assume that the planes are infinite so that the reflections from the surfaces ar specular. The path difference for two diffraction/reflection beams from two adjacent planes is $2\Lambda\sin(\theta)$, where θ is the angle between the incident direction and the grating planes. Constructive interference conditions require that the phase difference is an integer number (N) of 2π. Which leads to

$$2n_o\Lambda\sin(\theta) = N\lambda \tag{2.28}$$

This is the well-known *Bragg Law* and $\theta \equiv \theta_B$ is called the *Bragg angle*.[113] The grating vector $\mathbf{K}$ is defined to be perpendicular to the fringe planes and of strength $k = 2\pi/\Lambda$. The Bragg law can be understood as the momentum conservation of $\mathbf{k}_i + \mathbf{k}_d = \mathbf{K}$ if we define the grating vector $\mathbf{K}$ as the momentum of the grating. However when the incident angle slightly deviates from the Bragg angle relatively weak diffraction can also be observed. In this case the momentum is no longer conservative.

For a *thin grating*, as shown in Figure 2.10 (b), multiple diffraction orders other than the specular reflection can be obtained. From the viewpoint of quantum mechanics, the momentum of the grating is no longer well-defined for a thin grating. The Bragg's law for a thin grating is obtained from the constructive interference condition

$$n_o\Lambda\left(\sin(\theta) + \sin(\theta')\right) = N\lambda \tag{2.29}$$

In order to determine if a gating is a volume grating or a thin grating a dimensionless parameter (Klein-Cook parameter) is defined[113]

$$Q = \frac{2\pi\lambda L}{n_o \Lambda^2} \tag{2.30}$$

where L is the thickness of the grating. When $Q \ll 1$, the grating is a thin grating and the diffraction is in the *Raman-Nath regime*. When $Q \gg 1$, the grating is a volume grating and the diffraction is in the *Bragg regime*. The diffraction behaviors of these gratings can be described by Raman-Nath theory[114] and coupled wave theory[115], respectively. These theories will be discussed in detail in the following sections. The discussion on Raman-Nath and coupled wave theory have been adapted from Yeh.[113]

2.4.1 Raman-Nath Theory

In Raman-Nath theory the grating is treated as a spatially modulated phase retardation film since $\Lambda \gg \lambda$.[114] Thus, the electric filed of the transmitted wave can be expressed as

$$\mathbf{E}_t = \mathbf{E}_o e^{-i\phi - i(\omega t - \mathbf{k}\cdot\mathbf{r})} \tag{2.31}$$

where

$$\phi = \int \frac{\omega}{c} \Delta n ds \tag{2.32}$$

where the integral is over the ray path within the region $0 < x < L$. If L is small enough, the integral can simply be written as

$$\phi \simeq \delta \cos(\mathbf{K} \cdot \mathbf{r}) + Constant \tag{2.33}$$

where $\delta = \frac{2\pi L n_1}{\lambda \cos\theta}$. By using the identity for Bessel's function

$$e^{-\delta cos(x)} = \sum_{m=-\infty}^{\infty} J_m(\delta)(-i)^m e^{-imx} \tag{2.34}$$

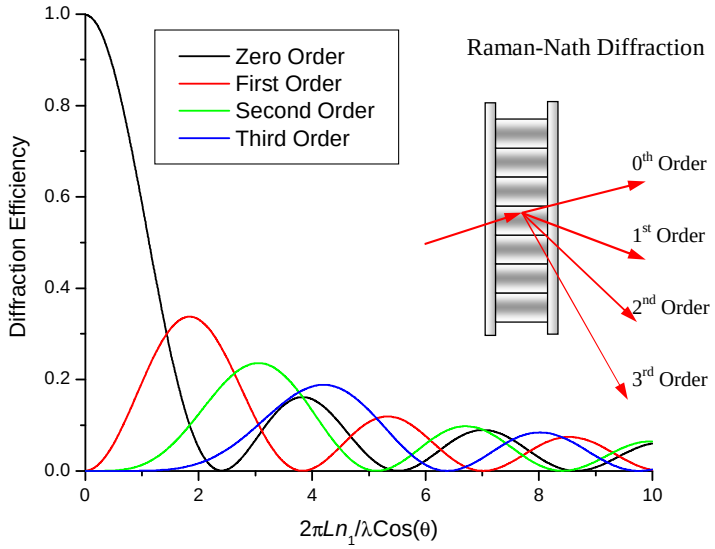

Figure 2.11. The Raman-Nath diffraction efficiencies of the zeroth, first, second and third orders. The maximum efficiency of the first order is 35%.

the electric field of the transmitted wave can be written as

$$\mathbf{E}_t = \mathbf{E}_o \sum_{m=-\infty}^{\infty} J_m(\delta)(-i)^m e^{i\omega t - i(\mathbf{k}-m\mathbf{K})\cdot\mathbf{r})} \tag{2.35}$$

Therefore the diffraction efficiency for the mth order Raman-Nath diffraction is given by

$$\eta_m = J_m^2(\delta) = J_m^2\left(\frac{2\pi L n_1}{\lambda\cos(\theta)}\right) \tag{2.36}$$

The identity for Bessel's function $\sum J_m^2(\delta) = 1$ indicates the energy is conserved.

In Figure 2.11 we calculate the diffraction efficiencies of the zeroth, first, second and third orders *via* equation (2.36). The maximum efficiency of the first order 34% is reached when $2\pi L n_1/(\lambda\cos\theta) = 1.84$. Note that the treatment as a spatially modulated phase retarder (equation (2.31)) is an approximate solution of Maxwell's equations.

2.4.2 Coupled Wave Theory

In 1969 a coupled wave theory was developed by Kogelnik for thick dielectric gratings ($Q \gg 1$).[115] In this approach the refractive index profile was assumed to be

sinusoidal and the dielectric medium is isotropic. He also assumed that a polarized monochromatic light propagates in the periodic medium and the diffracted beam can be coupled with the incident beam. The incident angle on the periodic medium was at or near the Bragg angle, which is the situation of most interest. At the condition, only the main diffracted order was considered and the other orders were neglected.

Due to the difference of the boundary conditions the coupling for transverse electric (TE) and transverse magnetic (TM) waves should be different. For simplicity, we only derive the coupled wave theory for TE waves. The theory of TM waves can be obtained by substituting the coupling coefficients.[115] In TE mode the directions of the electric field for the incident and diffracted beams are the same and we can use scalar wave equations to solve the problem. Inside the periodic medium the electric field can be expressed as

$$\mathbf{E} = \mathbf{A}_1 e^{i(\omega t - \mathbf{k}_1 \cdot \mathbf{r})} + \mathbf{A}_2 e^{i(\omega t - \mathbf{k}_2 \cdot \mathbf{r})} \tag{2.37}$$

where $\mathbf{k}_1$ and $\mathbf{k}_2$ are the wave vectors of the transmitted and diffracted beams, respectively. $\mathbf{A}_1$ and $\mathbf{A}_2$ are the amplitudes of the waves. The grating configuration is shown in Figure 2.12. The incident beam ($\mathbf{k}_1$) lies in the xz-plane and the electric filed $\mathbf{A}_1$ is along the y-direction. The wave vectors are related to the frequency by

$$|\mathbf{k}_1| = |\mathbf{k}_2| = \frac{n_o \omega}{c} \tag{2.38}$$

in the index modulation n_1 is much smaller than n_o. The boundary conditions of the fields restrict the wave vector $\mathbf{k}_2$ to also lie in the xz-plane and $\mathbf{A}_2$ lie along the y-direction.[116] The electric field can thus be written as the scalar form

$$E = A_1 e^{i(\omega t - \alpha_1 x - \beta_1 z)} + A_2 e^{i(\omega t - \alpha_2 x - \beta_2 z)} \tag{2.39}$$

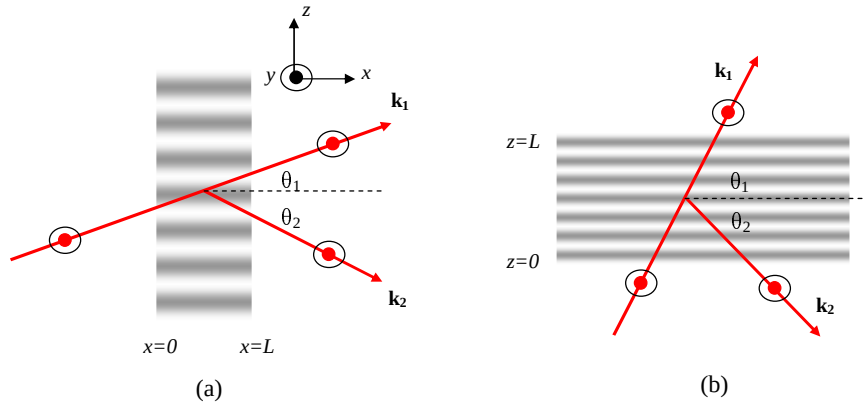

Figure 2.12. The configurations for coupled wave analysis (a) transmission grating; (b) reflection grating.

where $\alpha_{1,2}$ are the x-components of the wave vectors $\mathbf{k}_{1,2}$ and $\beta_{1,2}$ are the z-components of the wave vectors. The electric field satisfies the scalar wave equation

$$\left(\nabla^2 + \frac{\omega^2}{c^2} n^2\right) E = 0 \tag{2.40}$$

2.4.2.1 Coupled Wave Theory for Transmission Gratings

For transmission gratings we expect that the amplitudes $A_{1,2}$ are functions of x as required by the boundary conditions and we assume the grating is infinite along the z direction. Substituting equation (2.39) into the wave equation (2.40) we have

$$\begin{aligned}\sum_{j=1,2}\left[\left(\frac{d^2}{dx^2} - 2i\alpha_j \frac{d}{dx}\right) A_j e^{i(\omega t - \alpha_j x - \beta_j z)}\right] \\ = -\frac{\omega^2}{c^2} 2 n_o n_1 \cos(Kz) \sum_{j=1,2} A_j e^{i(\omega t - \alpha_j x - \beta_j z)} \\ -\frac{\omega^2}{c^2} n_1^2 \sum_{j=1,2} A_j e^{i(\omega t - \alpha_j x - \beta_j z)}\end{aligned} \tag{2.41}$$

Considering n_1 is of the order 10^{-1} to 10^{-3} we can neglect the second order term n_1^2. On the other hand, since the index modulation n_1 is small we expect the amplitudes A_j are

slowly varying functions and the second order derivative d^2A_j/dx^2 is negligible. Thus equation (2.41)can be rewritten as

$$-2i\alpha_1\frac{dA_1}{dx}e^{-i\alpha_1 x-i\beta_1 z}-2i\alpha_2\frac{dA_2}{dx}e^{-i\alpha_2 x-i\beta_2 z}$$

$$=-\frac{\omega^2}{c^2}n_o n_1\left(e^{-iKz}+e^{iKz}\right)\left(A_1e^{-i\alpha_1 x-i\beta_1 z}-A_2e^{-i\alpha_2 x-i\beta_2 z}\right) \tag{2.42}$$

Separating the two propagating components we deduce the coupled wave equations:

$$\frac{dA_1}{dx}=-i\kappa_{12}A_2e^{-i\Delta\alpha x}$$

$$\frac{dA_2}{dx}=-i\kappa_{21}A_1e^{i\Delta\alpha x} \tag{2.43}$$

where

$$\kappa_{12}=\frac{\pi n_1}{\lambda\cos(\theta_1)}\qquad\kappa_{21}=\frac{\pi n_1}{\lambda\cos(\theta_2)}$$

$$\Delta\alpha=\alpha_2-\alpha_1=\frac{2\pi}{\lambda}n_o\left(\cos(\theta_2)-\cos(\theta_1)\right) \tag{2.44}$$

provided the z-component of the momentum is conserved:

$$\beta_2=\beta_1\pm K \tag{2.45}$$

Equation (2.45) indicates the direction of the diffracted beam, which is illustrated in Figure 2.12 (a). The coupled wave equations (2.43) can be analogous with the equation of motion for a coupled pendulum. The energy is transferred and oscillating between two beams (transmitted and diffracted) with respect to position. The coupling and energy transfer depend on the index modulation n_1 and the phase matching condition.

When $\theta_2=\pm\theta_1$ the phase match $\Delta\alpha=0$ occurs. The solution $\theta_2=\theta_1$ is a trivial one which corresponds to no diffraction order. $\theta_2=-\theta_1$ indicates the Bragg condition

$$\theta_1=-\theta_2=\theta_B=\pm\sin^{-1}\left(\frac{\lambda}{2n_o\Lambda}\right) \tag{2.46}$$

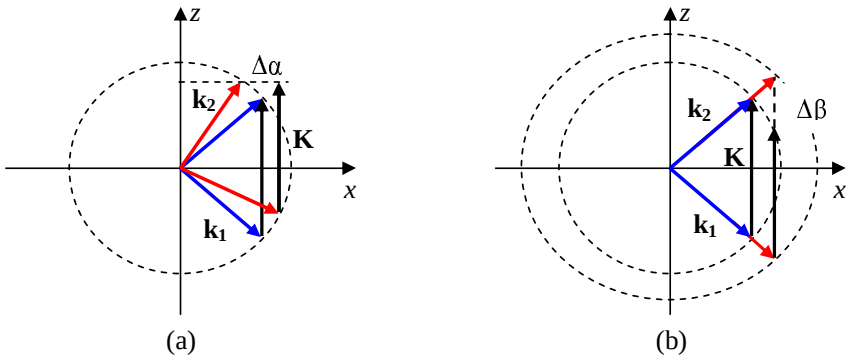

Figure 2.13. Schematic illustration of the phase mismatching conditions for a transmission grating (a) and a reflection grating (b). Blue wave vectors represent the phase matching conditions.

At the Bragg condition the coupled waved equations (2.43) become

$$\frac{dA_1}{dx} = -i\kappa A_2$$
$$\frac{dA_2}{dx} = -i\kappa A_1 \tag{2.47}$$

with

$$\kappa = \frac{\pi n_1}{\lambda \cos(\theta_B)} \tag{2.48}$$

Combining with the boundary condition $A_2(0) = 0$ we have the solution for an incident monochromatic plane wave

$$A_1(x) = A_1(0)\cos(\kappa x) \qquad A_2(x) = -iA_1(0)\sin(\kappa x) \tag{2.49}$$

This solution satisfies the conservation of energy as it must. The diffraction efficiency of the grating with a thickness K meeting the Bragg condition η_B can be defined as

$$\eta_B = \frac{|A_2(L)|^2}{|A_1(0)|^2} = \sin^2(\kappa L) \tag{2.50}$$

Ideally the grating achieves the maximum efficiency when $\kappa L = \pi/2$ and if $\kappa L > \pi/2$ it is called over-modulated.

When the phase mismatch occurs (see Figure 2.13 (a)) the incident angle $\theta_1 = \theta_B + \Delta\theta$ deviates from the Bragg angle and the Bragg condition (2.28) requires the diffraction angle $\theta_2 = -\theta_B + \Delta\theta + \mathcal{O}(\Delta\theta^2)$. The phase mismatch can be expressed as

$$\Delta\alpha = -2k\Delta\theta\sin(\theta_B) = -K\Delta\theta \tag{2.51}$$

Similarly to the phase match situation we can solve the coupled wave equations (2.43) to get the solution for a single plane wave incidence.

$$A_1(x) = A_1(0)e^{i\frac{\Delta\alpha}{2}x}\left[i\frac{\Delta\alpha}{2s}\sin(sx) + \cos(sx)\right]$$

$$A_2(x) = -iA_1(0)e^{i\frac{\Delta\alpha}{2}x}\left(\frac{\kappa_{21}}{s}\right)\sin(sx) \tag{2.52}$$

where

$$s = \sqrt{\kappa^2 + \left(\frac{\Delta\alpha}{2}\right)^2} \tag{2.53}$$

The diffraction efficiency is then given by

$$\eta = \frac{|A_2(L)|^2\cos(\theta_2)}{|A_1(0)|^2\cos(\theta_1)}$$

$$\eta = \frac{\kappa^2}{\kappa^2 + (\Delta\alpha/2)^2}\sin^2\left[\kappa L\left(1 + \left(\frac{\Delta\alpha}{2\kappa}\right)^2\right)^{\frac{1}{2}}\right] \tag{2.54}$$

The factors $\cos(\theta_1)$ and $\cos(\theta_2)$ in equation (2.54) indicate the energy flow direction of incident and diffracted beams are different.

The diffraction efficiency of TM waves can also be deduced under the same approach. The only noted difference is the coupling coefficient

$$\kappa_{TM} = \cos(\Theta)\kappa \tag{2.55}$$

where Θ is the angle between the electric fields of incidence and diffracted beams. Generally speaking, the coupling coefficient of TM waves is smaller than that of TE waves for isotropic gratings.

Based on the coupled wave theory we calculate the diffraction efficiencies of TM and TM waves as functions of grating thickness L which are shown in Figure 2.14 (a)-(b). Here we plot three plots with varying index modulations n_1, namely $n_1 = 0.01$, $n_1 = 0.003$ and $n_1 = 0.05$. The grating pitch is chosen to be 1.5 μm and the index of the grating is assumed to be $n_o = 1.47$. The monochromatic light is chosen to be a He-Ne laser (λ =632.8 nm) and an infrared line at $\lambda = 1.25$ μm. For $\lambda = 632.8$ nm the Bragg angle θ_B is small. The diffraction efficiencies of TE and TM waves are nearly the same.

Figure 2.14 (c)-(d) plots the diffraction efficiencies as functions of the incident angle θ_1. The angular aperture of the Bragg direction $\Delta\theta_{1/2}$ is defined as

$$\Delta\theta_{1/2} = \frac{2\kappa}{K} = \frac{\kappa\Lambda}{\pi} \tag{2.56}$$

From the Bragg law (2.28) the angular selectivity is equivalent to the wavelength selectivity

$$\Delta\lambda_{1/2} = 2n_o\Lambda\cos(\theta_B)\Delta\theta_{1/2} = \frac{2\kappa\Lambda}{\pi}n)o\Lambda\cos(\theta_B) \tag{2.57}$$

which corresponds to the half-width of the transmission notch from a broadband light source.

2.4.2.2 Coupled Wave Theory for Reflection Gratings

As seen in Figure 2.12 (b) for the reflection gratings, the boundary conditions require $\alpha_1 = \alpha_2$ or $\theta_2 = -\theta_1$ and the amplitudes of $A_{1,2}$ are functions of z. Thus we can deduce the coupled wave equations for reflections gratings

$$\begin{aligned} \frac{dA_1}{dz} &= -i\kappa A_2 e^{-i\Delta\beta z} \\ \frac{dA_2}{dz} &= \kappa A_2 e^{i\Delta\beta z} \end{aligned} \tag{2.58}$$

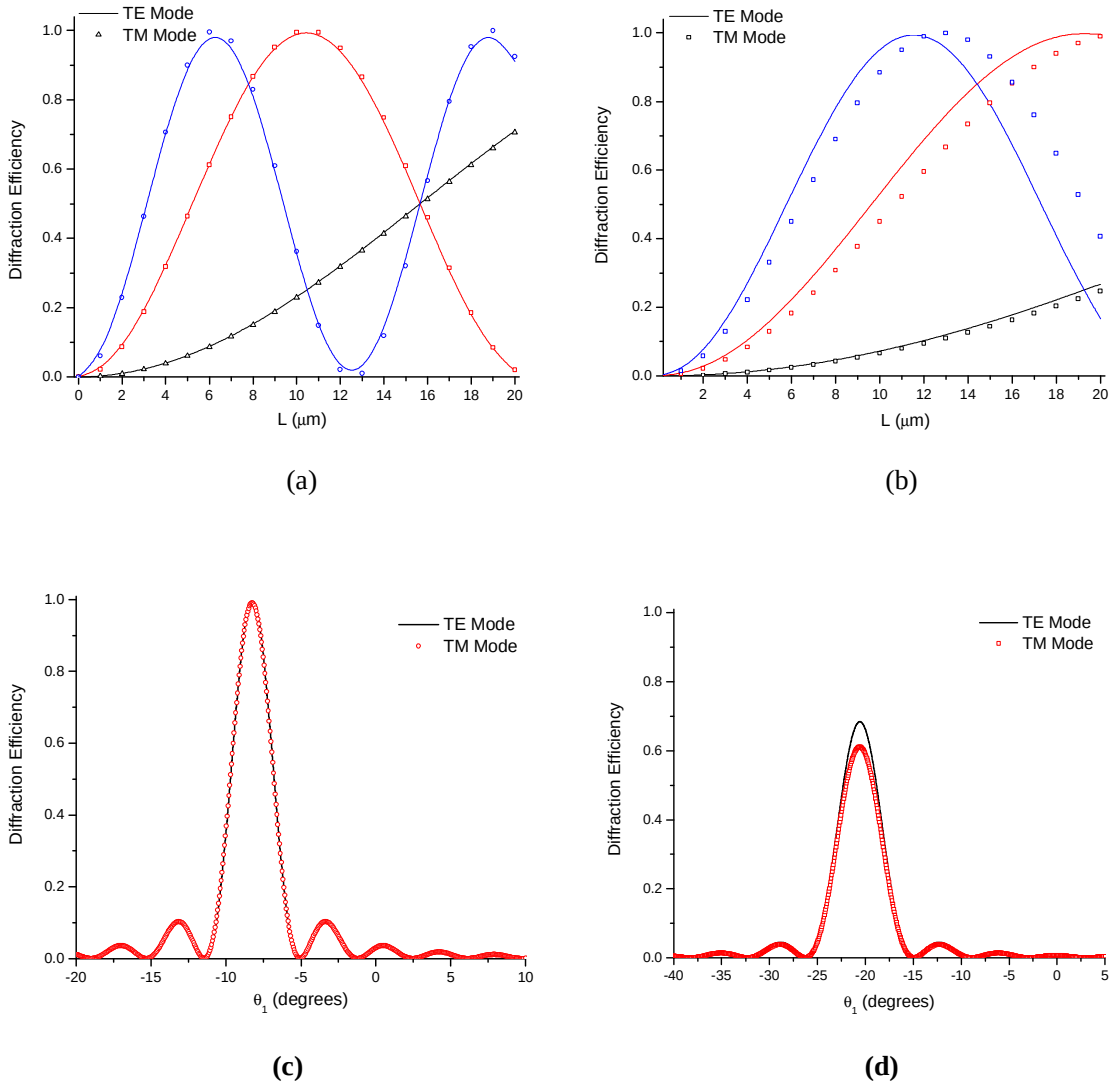

Figure 2.14. Calculated diffraction efficiency and angular selectivity of transmission gratings predicted by coupled wave theory. (a) Bragg diffraction efficiency of TE/TM waves vs. grating thickness L at 632.8 nm ($n_1 = 0.01$, $n_1 = 0.03$, $n_1 = 0.05$). (b) Bragg diffraction efficiency vs. grating thickness L at 1250 nm ($n_1 = 0.01$, $n_1 = 0.03$, $n_1 = 0.05$). (c) Polarized angular selectivity of a grating of thickness $L = 10\mu$m and n_1 =0.03 at 632.8 nm. (d) Polarized angular selectivity of a grating of thickness $L = 15\mu$m and $n_1 = 0.03$ at 1550 nm.

where

$$\Delta\beta = \beta_2 - \beta_1 \pm K \tag{2.59}$$

and

$$\kappa = \frac{\pi n_1}{\lambda sin(\theta_1)} \tag{2.60}$$

One can determine the reflection efficiency of reflection gratings by

$$\eta = \frac{|A_2(L)|^2}{|A_1(0)|^2} = \frac{|\kappa|^2 \sinh^2(sL)}{s^2 \cosh^2(sL) + \left(\frac{\Delta\beta}{2}\right)^2 \sinh^2(sL)} \tag{2.61}$$

where

$$s = \sqrt{|\kappa|^2 - \left(\frac{\Delta\beta}{2}\right)^2} \tag{2.62}$$

The width of the reflection band can be estimated as $\Delta\lambda/\lambda \sim n_1/(n_o \sin^2(\theta_1))$. When the phase matches $\Delta\beta = 0$ the peak reflection efficiency is given by

$$\eta_{max} = \tanh^2(\kappa L) \tag{2.63}$$

is achieved. Note that there is no over-modulation in reflection gratings. Figure 2.15 plots the reflectance and reflection spectra of isotropic gratings with different parameters. As seen in Figure 2.15 (a) and (b) theoretical the peak reflection can reach near 100% when $\kappa L \sim 2$. Figure 2.15 (c) simulates the reflection spectra of a grating with a peak reflection at 635 nm. The thickness of the grating is chosen to be 5 μm. Similarly the coupling coefficient for TM waves is given by

$$\kappa_{TM} = \kappa \cos(\Theta) \tag{2.64}$$

which implies the reflection of TM waves is always lower than that of TE waves as seen in Figure 2.15 (d). At incident an angle of 45^o the reflection efficiency of TM waves is exactly zero. This incident angle matches the angle given by Brewster's law. When the incident angle becomes more oblique the peak wavelength shifts to shorter wavelengths, which is predicted by Bragg's law.[116] For normal incidence ($\Theta = 0$) there is no polarization dependence for an isotropic grating.

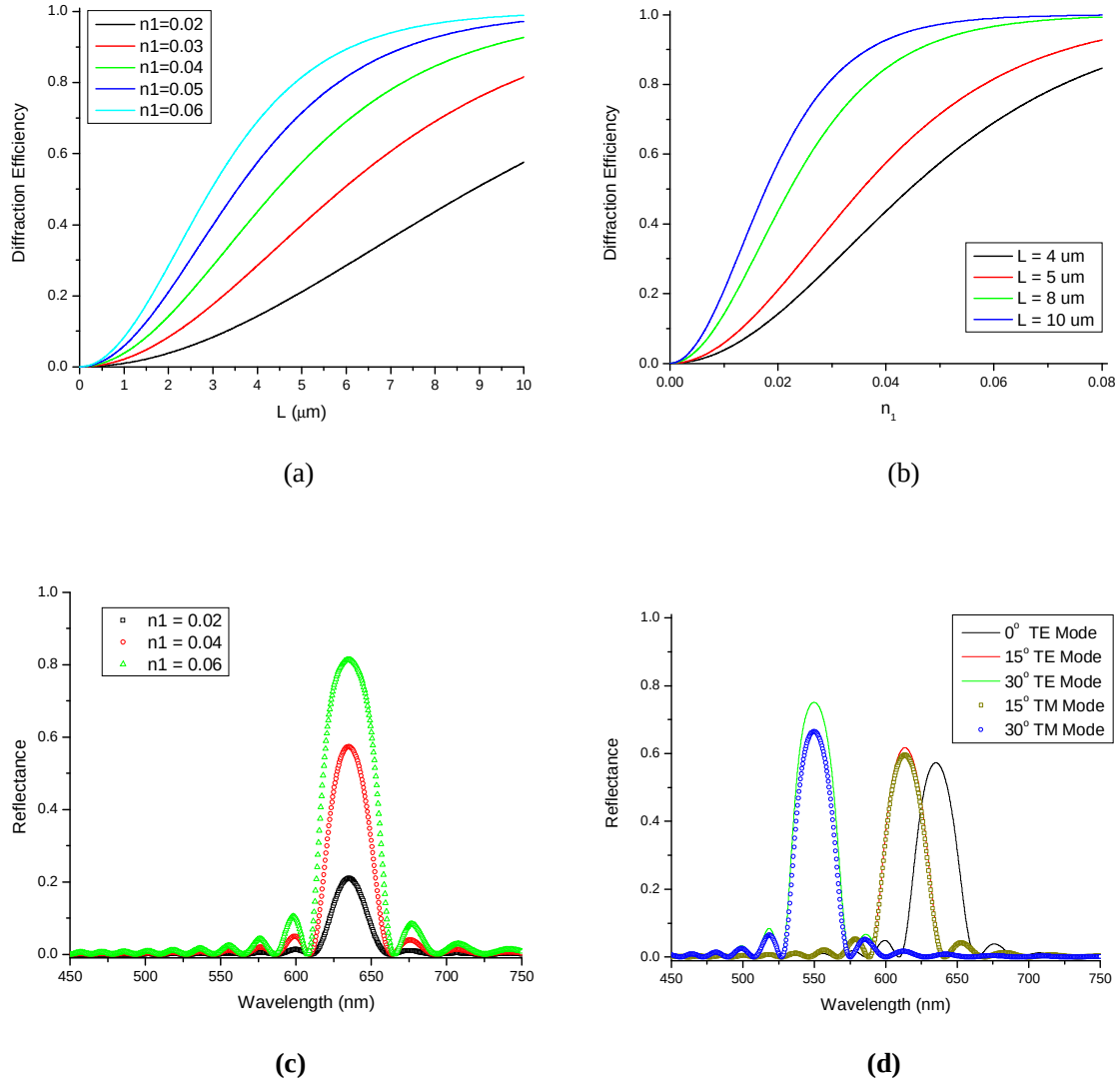

Figure 2.15. Calculated Bragg reflection efficiency predicted by coupled wave theory. (a) Peak reflection efficiency as a function of grating thickness L. (b) Peak reflection efficiency as a function of the index modulation n_1. (c) Reflection spectra of a grating with parameters $n_0 = 1.55$, $2n_o\Lambda = 635$ nm and $L = 5\mu$m. (d) Reflection spectra of oblique incidence (defined as 90^o - θ_1). The peak wavelength shifts to shorter wavelengths and the reflection efficiency of TE and TM waves have different tendencies.

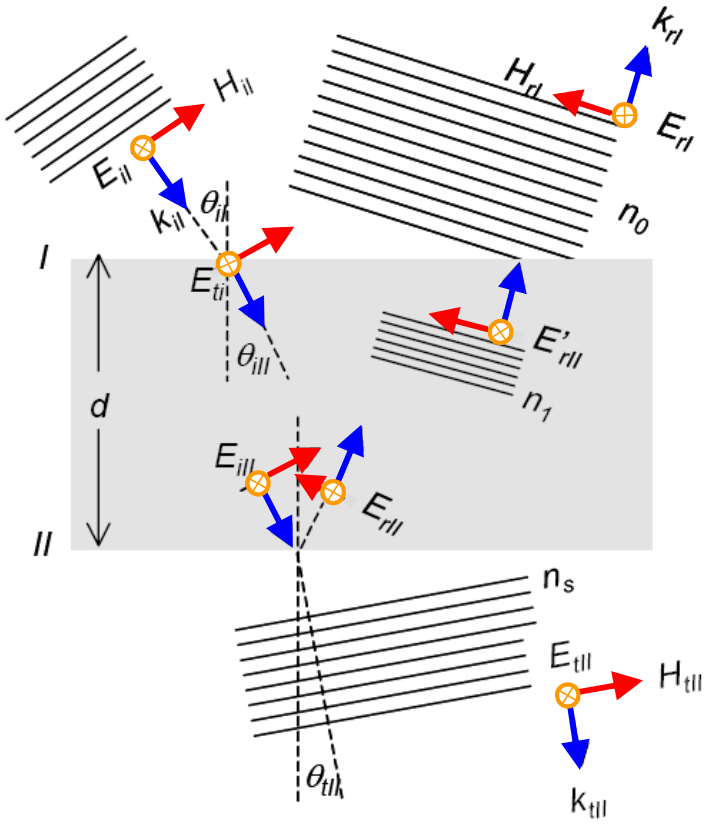

Figure 2.16. Electric and magnetic fields at the boundaries of a thin dielectric film.

2.4.3 2 x 2 Matrix Methods

An H-PDLC can also be modeled as a thin dielectric film sandwiched between two semi-infinite transparent media. The transmission and reflection characteristics can be modeled by considering the linearly polarized light shown in Figure 2.16, with each wave representing the sum of all possible waves traveling in that direction. The tangential components of the electric (**E**) and magnetic (**H**) fields must be continuous across the boundaries due to boundary conditions.

At boundary 1:

$$E_1 = E_{i1} + E_{r1} = E_{t1} + E'_{r2} \tag{2.65}$$

and

$$H_1 = \sqrt{\frac{\epsilon_o}{\mu_o}}(E_{i1} - E_{r1})n_o \cos(\theta_{i1}) = \sqrt{\frac{\epsilon_o}{\mu_o}}(E_{t1} - E_{r2}^{'})n_o \cos(\theta_{i2}) \tag{2.66}$$

since in a nonmagnetic media **E** and **H** are related the unit propagation vector and the index of refraction by

$$H = \sqrt{\frac{\epsilon_o}{\mu_o}} n\hat{\mathbf{k}} \times \mathbf{E} \tag{2.67}$$

At boundary2:

$$E_2 = E_{i2} + E_{r2} = E_{t2} \tag{2.68}$$

and

$$H_2 = \sqrt{\frac{\epsilon_o}{\mu_o}}(E_{i2} - E_{r2})n_1 \cos(\theta_{i2}) = \sqrt{\frac{\epsilon_o}{\mu_o}}(E_{t2} - E_{r2}^{'})n_s \cos(\theta_{i2}) \tag{2.69}$$

where n_s is the index of refraction of the substrate.

When a wave passes through a dielectric medium, it undergoes an optical path length shift of

$$h = \frac{2n_1 d \cos(\theta_{i2})}{2} \tag{2.70}$$

The phase difference is just the product of the free-space propagation number and h, which is $k_o h$, so

$$E_{t2} = E_{t1} e^{-ik_o h} \tag{2.71}$$

and

$$E_{r2} = E_{r2}^{'} e^{ik_o h} \tag{2.72}$$

Substituting into equation (2.68):

$$E_2 = E_{t1} e^{-ik_o h} + E_{r2}^{'} e^{ik_o h} \tag{2.73}$$

and equation (2.69) becomes

$$H_2 = \left(E_{t1} e^{-ik_o h} - E_{r2}^{'} e^{ik_o h}\right) \sqrt{\frac{\epsilon_o}{\mu_o}} n_1 \cos(\theta_{i2}) \tag{2.74}$$

Solving and substituting back into equations (2.65) and (2.66), we find

$$E_1 = E_2 \cos(k_o h) + \frac{H_2(i \sin(k_o h))}{\Upsilon_1} \tag{2.75}$$

and

$$H_1 = E_2 \Upsilon_1 i \sin(k_o h) + H_2 \cos(k_o h) \tag{2.76}$$

where

$$\Upsilon_1 = \sqrt{\frac{\epsilon_o}{\mu_o}} n_1 \cos(\theta_{i2}) \tag{2.77}$$

In matrix notation, these relationships can be written as

$$\begin{bmatrix} E_1 \\ H_1 \end{bmatrix} = \begin{bmatrix} \cos(k_o h) & \frac{i \sin(k_o h)}{\Upsilon_1} \\ i\Upsilon_1 \sin(k_o h) & \cos(k_o h) \end{bmatrix} \cdot \begin{bmatrix} E_2 \\ H_2 \end{bmatrix} = \mathcal{M}_1 \begin{bmatrix} E_2 \\ H_2 \end{bmatrix} \tag{2.78}$$

where $\mathcal{M}_1$ is the characteristic matrix relating the fields at the two adjacent boundaries. With two overlaying films, there are three boundaries and

$$\begin{bmatrix} E_2 \\ H_2 \end{bmatrix} = \mathcal{M}_2 \begin{bmatrix} E_3 \\ H_3 \end{bmatrix} \tag{2.79}$$

If we multiply both sides by $\mathcal{M}_1$, we find

$$\begin{bmatrix} E_1 \\ H_1 \end{bmatrix} = \mathcal{M}_1 \mathcal{M}_2 \begin{bmatrix} E_3 \\ H_3 \end{bmatrix} \tag{2.80}$$

In general, with p layers with specified values of n and h, the first layer and the last layer are related by

$$\begin{bmatrix} E_1 \\ H_1 \end{bmatrix} = \mathcal{M}_1 \mathcal{M}_2 .... \mathcal{M}_p \begin{bmatrix} E_{p+1} \\ H_{p+1} \end{bmatrix} \tag{2.81}$$

The characteristic matrix $\mathbf{M}$ for the entire system is the product of the individual 2x2 matrices:

$$\mathbf{M} = \mathcal{M}_1 \mathcal{M}_2 .... \mathcal{M}_p = \begin{bmatrix} m_{11} & m_{12} \\ m_{21} & m_{22} \end{bmatrix} \tag{2.82}$$

We can now determine the reflection and transmission amplitudes of a multi-layer stack. Examining boundary conditions leads to the definitions

$$\Upsilon_0 = \sqrt{\frac{\epsilon_o}{\mu_o}} n_o \cos(\theta_{i1}) \tag{2.83}$$

and

$$\Upsilon_s = \sqrt{\frac{\epsilon_o}{\mu_o}} n_s \cos(\theta_{t2}) \tag{2.84}$$

which leads to the matrix equation

$$\begin{bmatrix} E_{i1} + E_{r1} \\ (E_{i1} + E_{r1})\Upsilon_o \end{bmatrix} = \mathcal{M}_1 \begin{bmatrix} E_{t2} \\ E_{t2}\Upsilon_s \end{bmatrix} \tag{2.85}$$

If we define the reflectance and transmission as $R = E_{r1}/E_{i1}$ and $T = E_{t2}/E_{i1}$ respectively, then we can expand the matrices to find

$$1 + R = m_{11}T + m_{12}\Upsilon_s T \tag{2.86}$$

and

$$(1 - R)\Upsilon_o = m_{21}T + m_{22}\Upsilon_s T \tag{2.87}$$

To find the reflection and transmission characteristics of any film, one needs to compute **M** for each film and then substitute into the following equations:

$$R = \frac{\Upsilon_o m_{11} + \Upsilon_o \Upsilon_s m_{12} - m_{21} - \Upsilon_s m_{22}}{\Upsilon_o m_{11} + \Upsilon_o \Upsilon_s m_{12} + m_{21} + \Upsilon_s m_{22}} \tag{2.88}$$

and

$$T = \frac{2\Upsilon_o}{\Upsilon_o m_{11} + \Upsilon_o \Upsilon_s m_{12} + m_{21} + \Upsilon_s m_{22}} \tag{2.89}$$

To find either R or T for any configuration of films, we need only compute the characteristic matrices for each film, multiply them, and then substitute the resulting matrix elements into the above equations.

2.5 Holographic Polymer Dispersed Liquid Crystals: Electro-Optical Properties

The response of anisotropic nematic liquid crystal molecules in an electric field is a very interesting topic of study. When applying an electric field the nematic directors in bulk materials will relax to the lowest energy stat and align along or perpendicular to the direction of the external field depending on the dielectric anisotropy of the material. The reorientation of liquid crystal molecules are accompanied by the response of optical properties, such as the refractive index.

The minimum Frank free energy state of bulk nematic liquid crystals is on with a uniform director field **n**. When combining with different boundary conditions the minimum energy state may have a non-uniform **n** configuration. In order to study this problem we start from a simplified model as seen in Figure 2.17 (a). A semi-infinite bulk liquid crystal is homogeneously aligned along the z-direction in the yz-plane and an electric filed is applied along the z-direction. The anchoring strength is assumed to be infinite. If the liquid crystal molecules have positive dielectric anisotropy ($\Delta\epsilon > 0$) the molecules tend to be aligned along the direction of the external field. Neat the surface, the alignment of the surface will compete with the alignment of the external field and lead to a nun-uniform **n** configuration. There are several questions that aries from this situation: (1) is the electric field strong enough to change the macroscopic order or the scalar order parameter S (therefore the dielectric anisotropy), (2) is there a threshold field required to align the bulk liquid crystal material, (3) how does the alignment of the surface anchoring compete with the field effect and (4) what is the characteristic length of the non-uniform **n** configuration induced by the external field.

In the case of liquid crystal with positive dielectric anisotropy the external field tends to align the molecules along the direction of the applied field and stabilizes the

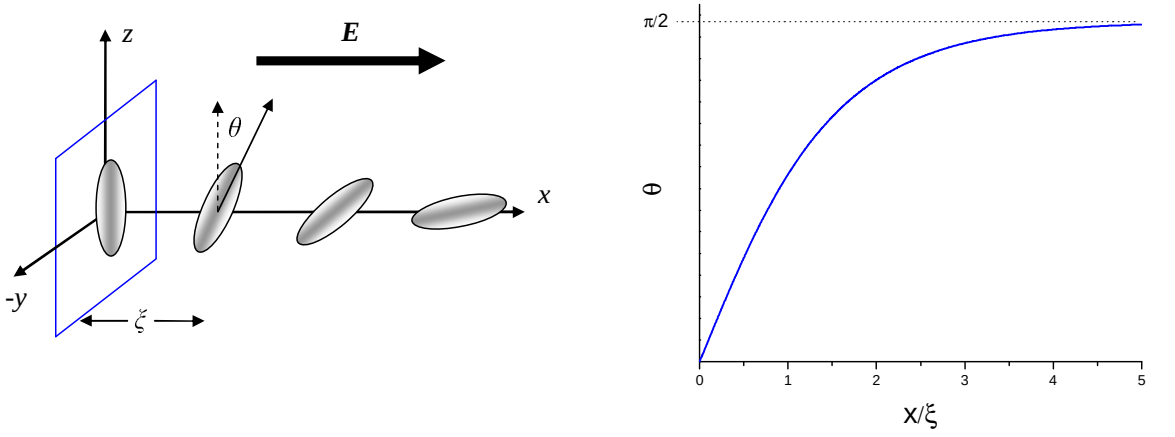

Figure 2.17. The electric field effect on a semi-infinite homogeneously aligned liquid crystal. (a) Schematic illustration of direction configuration and (b) the calculated deformation angle θ.

nematic order. The nematic-isotropic transition temperature increases due to the applied field by a value of[117]

$$\Delta T_{NI} = \frac{\delta\epsilon\epsilon_o E^2}{2\Delta H} \tag{2.90}$$

where $\delta\epsilon \equiv \epsilon - \epsilon_{iso}$ and ϵ_{iso} is the dielectric constant of liquid crystal in the isotropic phase. ΔH is the enthalpy of the nematic-isotropic transition and a typical value is $\sim$ 5 x 10^3 j·m^3. At the strength of 10V/μm external field $\sim$ 1 K increasing of nematic-isotropic transition temperature is expected. In the Landau-de Genne theory the order parameter S is the slow-varied function of $T - T_{NI}$.[118] If the temperature deviates from the nematic-isotropic transition point the changes in the nematic order and dielectric anisotropy are negligible.

The other remaining questions can be answered using Frank continuum theory. The Frank free energy of the semi-infinite liquid crystal per-unit-area can be expressed as

$$F = \frac{1}{2}\int dx \left[K\left(\frac{d\theta}{dx}\right)^2 - \Delta\epsilon\epsilon_o E^2 \sin^2(\theta)\right] \tag{2.91}$$

where θ is the angle between the director field $\mathbf{n}$ and the z-axis. Analogous to the Hamiltonian principle in classical mechanics and considering there is no deformation at infinity we have the "equation of motion"

$$\left(\frac{d\theta}{dx}\right)^2 - \frac{\Delta\epsilon\epsilon_o E^2}{K}\sin^2(\theta) = \frac{\Delta\epsilon\epsilon_o E^2}{K}\sin^2(\theta)|_{\theta=\frac{\pi}{2}} \tag{2.92}$$

This equation can be rewritten as

$$\left(\frac{d\theta}{dx}\right)^2 = \frac{1}{\xi^2}\cos^2(\theta) \tag{2.93}$$

where

$$\xi = \sqrt{\frac{K}{\Delta\epsilon\epsilon_o E^2}} \tag{2.94}$$

is called the coherent length of the applied electric field.[118] Considering $K \sim 10$ pN and $\Delta\epsilon \sim 10$ the value of the coherent length is 0.3 μm for $E = 1.0$ V/μm. Integrating over equation (2.93) we have the director field configuration of the minimum energy state

$$\theta(x) = \frac{\pi}{2} - 2\tan^{-1}(e^{-x/\xi}) \tag{2.95}$$

which is potted in Figure 2.17 (b). The response to an external field is thresholdless. One can see the physical meaning of the coherent length ξ is the characteristic penetration length of the surface alignments. Above the length ξ the director field $\mathbf{n}$ is nearly uniform.

2.5.1 Fréedericksz Transition in 1D Cell

In confined liquid crystal with an applied field it is more complicated that the previous simplified model. There are two characteristic lengths, the coherent length of the external field ξ and the physical dimensions of confinement D. When $D \gg \xi$ (high field limit) we can approximately model confined liquid crystal as bulk and most of the director fields are aligned by the external field. If these two length scales ar close these two alignment effects compete with each other. Fréedericksz first investigated the optical

response of homogeneously aligned cells in magnetic fields.[119] He found that the field strength above a threshold value is necessary to deform the liquid crystal directors, later called Fréedericksz transition. In the following sections we will discuss the Fréedericksz transition in 1D, 2D and 3D cases. The Fréedericksz transition is the basis of modern liquid crystal displays and H-PDLC technologies. The investigations of Fréedericksz transitions in simple 3D model will be helpful in the understanding of the electro-optical performances and properties of H-PDLCs.

2.5.1.1 Infinite Anchoring

The simplest confinement geometry in a homogenous aligned cell with thickness k as seen in Figure 2.18 (a). The anchoring on both surfaces is assumed to be infinite. Before applying an electric field the director in the cell is uniform. By taking the derivative of equation (2.93) the equation of motion for the static case can be expressed as

$$K\frac{d^2\theta}{dx^2} - \frac{K}{\xi^2}\sin(\theta)\cos(\theta) = 0 \tag{2.96}$$

which is associated with the boundary conditions

$$\theta|_{x=0} = \theta|_{x=d} = 0 \tag{2.97}$$

On the left side of equation (2.96) the first and second terms represent the torque due to deformation and external field. The balance of the elastic torque and external field torque leads to the equilibrium condition. From the symmetry argument at the cell center $d\theta/dx$ is expected to be zero. Defining the deviation angle at the cell center $\theta|_{x=d/2} = \theta_M$. Equation (2.96) can then be integrated to

$$\frac{d\theta}{dx} = \pm\frac{1}{\xi}\sqrt{\sin^2(\theta_M) - \sin^2(\theta)} \tag{2.98}$$

This leads to an analytic solution of the form

$$\frac{d}{2\xi}\sin(\theta_M) = \int_0^{\theta_M} \frac{d\theta}{\sqrt{1 - \sin^2(\theta)/\sin^2(\theta_M)}} = \sin(\theta_M)\mathcal{F}\left(\frac{\pi}{2}, \sin(\theta_M)\right) \tag{2.99}$$

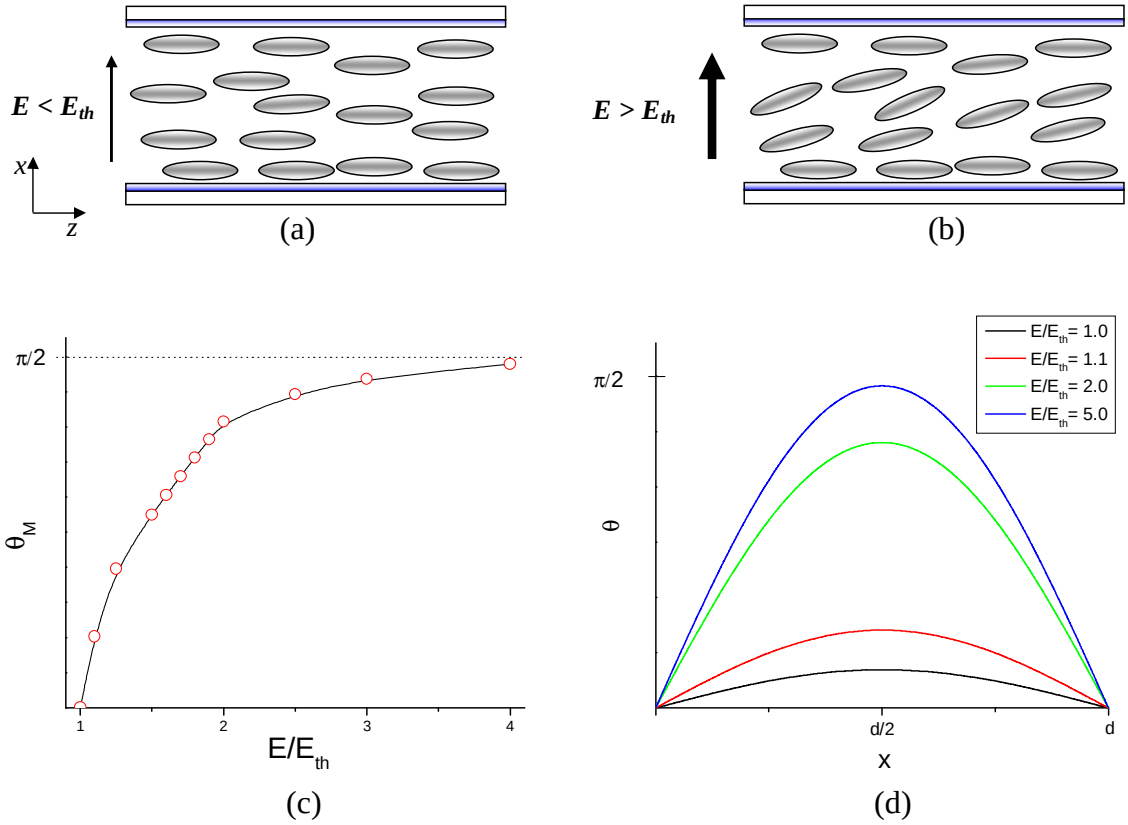

Figure 2.18. Fréedericksz transition in a homogeneously aligned sample. (a) When $E < E_{th}$ no deformations are generated. (b) When $E > E_{th}$ the directors in the cell center start to align first. (c) The maximum deviation angle θ_M at the center of the cell as a function of normalized electric field E/E_{th}. Near $\theta_M \sim 0$ we have $\theta_M \propto (E - E_{th})^{1/2}$. (d) The deviation angle θ in the cell is a sinusoid shape small angle approximation which is valid if $\theta < \pi/3$.

Here $\mathcal{F}\left(\frac{\pi}{2}, \sin(\theta_M)\right) = \int_0^{\pi/2} dx/\sqrt{1 - k^2 \sin^2(x)}$ is the first kind of elliptical integral.[120] It can be shown that at the limit $\theta_M \to 0$ we get $\xi = \pi d$ which implies there is a threshold value of

$$E_{th} = \frac{\pi}{2}\sqrt{\frac{K}{\Delta\epsilon\epsilon_o}} \tag{2.100}$$

and

$$V_{th} = \pi\sqrt{\frac{K}{\Delta\epsilon\epsilon_o}} \tag{2.101}$$

When the strength of electric field $E < E_{th}$ the field is not sufficient to align the director and no deformations are generated in the material. When $E > E_{th}$ the directors start to deviate from the original aligned direction. This reorientation of director field can be observed by the transmission measurement of polarized light. Under the small angle approximation ($\sin(\theta) \simeq \theta$) the deviation angle in the cell can be expressed as

$$\theta = \theta_M \sin\left(\frac{\pi x}{d}\right) \tag{2.102}$$

In Figure 2.18 (c) we plot the numerical calculation of θ_M as a function of E/E_{th}. Near $\theta_M \sim 0$ we have $\theta_M \propto (E - E_{th})^{1/2}$. This behavior implies that practice a pretilt angle is needed in the zero field state. If there is no pretilt angle, two degenerate states (clockwise and counterclockwise rotations) are possible. The numerical calculations of director profile are also seen in Figure 2.18 (d). When the maximum angle $\theta_M < \pi/3$ the small angle approximation is valid.

In order to calculate the dynamic response of the liquid crystals a viscous torque $\gamma d\theta/dt$ should be added to the equation of motion[121]

$$K\frac{d^2\theta}{dx^2} - \frac{K}{\xi^2}\sin(\theta)\cos(\theta) = \gamma\frac{d\theta}{dt} \tag{2.103}$$

from which one can determine the rise times τ_{on} and fall time τ_{off}

$$\tau_{on} = \frac{\gamma}{\Delta\epsilon\epsilon_o(E^2 - E_{th}^2)} \tag{2.104}$$

and

$$\tau_{off} = \frac{\gamma}{\Delta\epsilon\epsilon_o E_{th}^2} \tag{2.105}$$

Here γ is the rotational viscosity coefficient. Note that $E_{th}^2\tau_{off}$ is a constant which is related to the material properties. This is generally true in continuous liquid crystal elastic model.

2.5.1.2 Finite Anchoring

The previous discussionis restricted to infinite anchoring strength. If the strength of the homogenous alignment on both surfaces is finite the anchoring torque at the boundaries is necessary to be considered and the threshold voltage should be relaxed to a lower value. Under finite anchoring conditions the boundary conditions on both surfaces are modified as[122]

$$\frac{d\theta}{dx}|_S \pm \frac{W}{K}\sin(\theta)\cos(\theta) = 0 \tag{2.106}$$

and the equation of motion keeps the same form. Near the transition point $\theta \sim 0$ the sinusoid solution

$$\theta = \theta_M \sin(Ax + B) \tag{2.107}$$

is obtained. Utilizing equation (2.106) and (2.107) we can find the following

$$\tan(B) = \frac{AK}{W} \equiv Al \equiv Ad\omega \tag{2.108}$$

where $l \equiv K/W$ has the dimensions of length and a dimensionless parameter $\omega \equiv K/Wd$ denotes the anchoring strength. The typical value of W is on the order of 10^{-4} to 10^{-7} J/m^2. It is worth noting that the anchoring condition is correlated to the dimension of confinement. At the limit $W \to \infty(\omega \to 0)$ we have $B = 0$ which is in agreement of the previous result. On the other hand, from the symmetry of the problem we expect the deviation angles at both surfaces to be the same, which gives

$$Ad + 2B = \pi \tag{2.109}$$

Under strong anchoring limit, $\tan(B) \simeq B$, we can solve $A = \pi/(d + f(\omega)l)$ with $f(\omega) = 2$, giving a threshold voltage of

$$E_{th} = \frac{\pi}{d + f(\omega)l}\sqrt{\frac{K}{\Delta\epsilon\epsilon_o}} \tag{2.110}$$

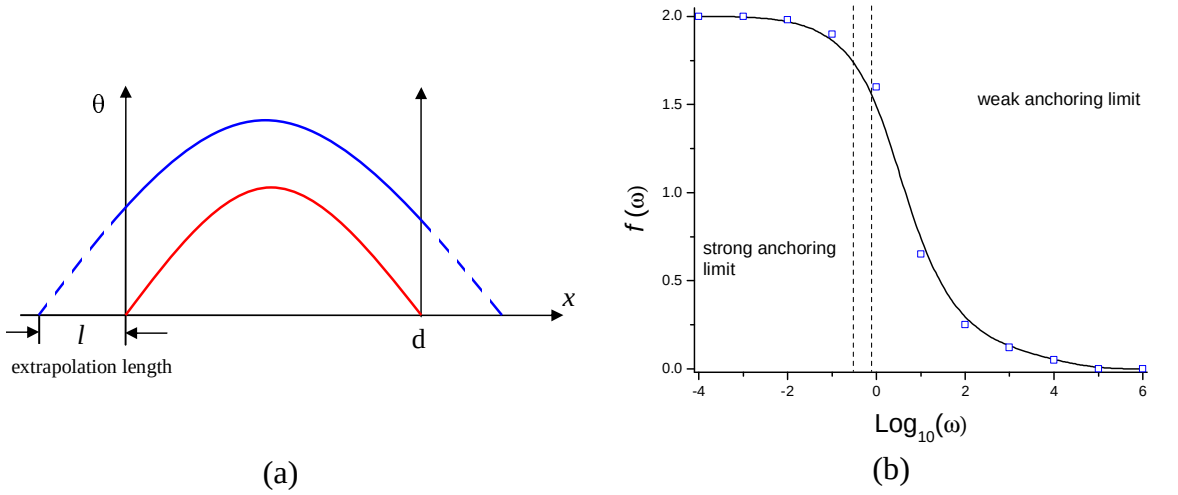

Figure 2.19. Finite anchoring of the cell surface. (a) the deviation angle θ is not fixed to be zero at the boundaries which can be extrapolated to be zero after extrapolation length l. (b) The numerical calculation of the dimensionless function $f(\omega)$ approaches 2. Between two dashed lines are the strong and weak anchoring limits.

Here the length l can be explained as a surface extrapolation length as seen in Figure 2.19 (a). For weak anchoring conditions the previous approximation is not valid and the function $f(\omega)$ relaxes to a lower value as seen in Figure 2.18 (b). Under the weak anchoring limit $\omega \rightarrow \infty$ the extrapolation length is much larger than the cell thickness d. Approximately we can express the threshold field as

$$E_{th} \simeq \sqrt{\frac{2W}{\Delta\epsilon\epsilon_o}d} \tag{2.111}$$

The expressions for response times (2.104) and (2.105) are still valid. Both weak and strong anchoring approximations are valid only for some particular values of ω as seen in Figure 2.19 (b). The criterion utilized to determine the validity is 10% error.

2.5.2 2D Periodically Modulated Cylindrical Confinement

The Fréedericks transitions in a cylindrical geometry with different alignment configurations have been studied.[123, 124] In the 2D transverse lattice H-PDLC we find the

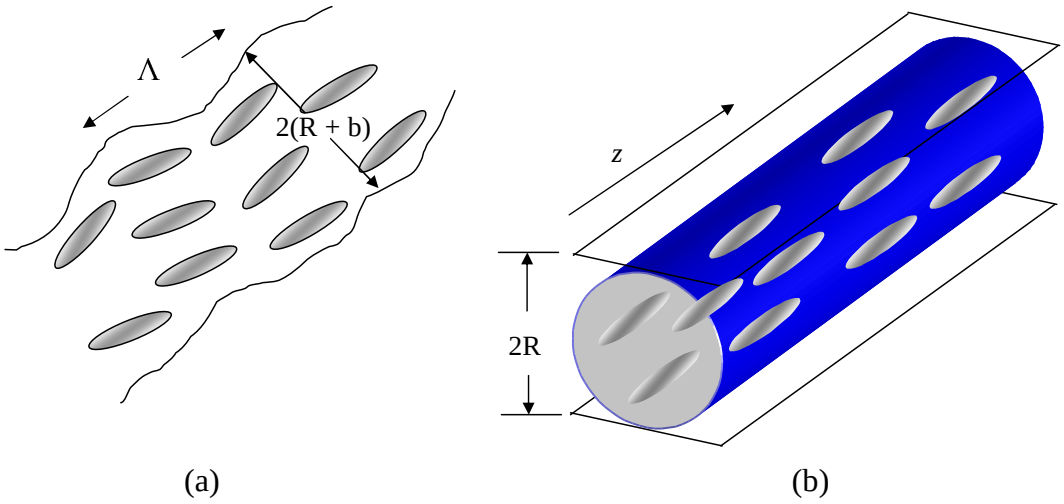

Figure 2.20. The modeled geometries for the confinement in 2D transverse lattices: (a) periodic modulated cylinder and (b) the ideal cylinder.

liquid crystal confined in cylindrical type geometries. Also the confined liquid crystals are normally highly aligned along the azimuthal direction. The electro-optic measurements of these H-PDLCs shows a strong threshold behavior ($E_{th} \sim 8\text{V}/\mu\text{m}$). Here we utilize previous studies to estimate the anchoring effects of liquid crystal/polymer interfacial interaction in these systems.

2.5.2.1 Infinite Cylindrical Confinement

First we model this geometry as a periodic modulated cylindrical geometry as seen in Figure 2.20 (a). In this model the roughness of liquid crystal/polymer interfaces is modeled as a periodic modulation. This approach has been employed in other systems.[18] Before calculating the Freedericksz transition in 2D we start with a pure cylindrical confinement with infinite anchoring strength as seen in Figure 2.20 (b). The director field on the surface is assumed to be aligned along the azimuthal direction (z-axis).

In cylindrical coordinates the equation of motion can be written as

$$\frac{d^2\theta}{d\rho^2} + \frac{1}{\rho}\frac{d\theta}{d\rho} + \frac{1}{\rho^2}\frac{d^2\theta}{d\phi^2} + \frac{1}{\xi^2}\sin(\theta)\cos(\theta) = 0 \tag{2.112}$$

Considering the equilibrium state should have the lowest energy. $\frac{d^2\theta}{d\phi^2}$ is expected to be zero given the angular dependence should be $\theta \sim \theta(\rho)\cos(\nu\phi)$, where ν is an integer. Clearly the state with $\nu = 0$ does not introduce deformations on the ϕ dimension. Under the small angle approximation ($\sin(\theta) \sim \theta$) the equation of motion can be written as

$$\frac{d^2\theta}{d\rho^2} + \frac{1}{\rho}\frac{d\theta}{d\rho} + \frac{1}{\xi^2}\theta = 0 \tag{2.113}$$

This is the Bessel's equation and a solution $\theta \sim J_o(\rho/\xi)$ is obtained.[125] The boundary condition restricts $J_o(R/\xi) = 0$. Therefore the threshold filed can be expressed as

$$E_{th} = \frac{\eta}{R}\sqrt{\frac{K}{\Delta\epsilon\epsilon_o}} \tag{2.114}$$

where $\eta = 2.4808$ is the first root of Bessel's function $j_o(x)$. The numerical value 2.4808 is slightly larger than the value for a square geometry $\pi/\sqrt{2} = 2.2214$ since the confinement of cylindrical geometry is tighter than the rectangle geometry.

2.5.2.2 Finite Anchoring

For finite anchoring condition the boundary condition leads to

$$\frac{d\theta}{d\rho}|_{\rho=R} + \frac{W}{K}\theta = 0 \tag{2.115}$$

Analogous with the 1D case the threshold field can be expressed as

$$E_{th} = \frac{\eta}{r + f_c(\omega)l}\sqrt{\frac{K}{\Delta\epsilon\epsilon_o}} \tag{2.116}$$

The dimensionless function f_c can be solved numerically, which is shown in Figure 2.21. Under strong anchoring limit it is not a surprise that $f_c(\omega) = 1$ compared to $f_c(\omega) = 2$ since in the 1D case we extrapolate to both surfaces.

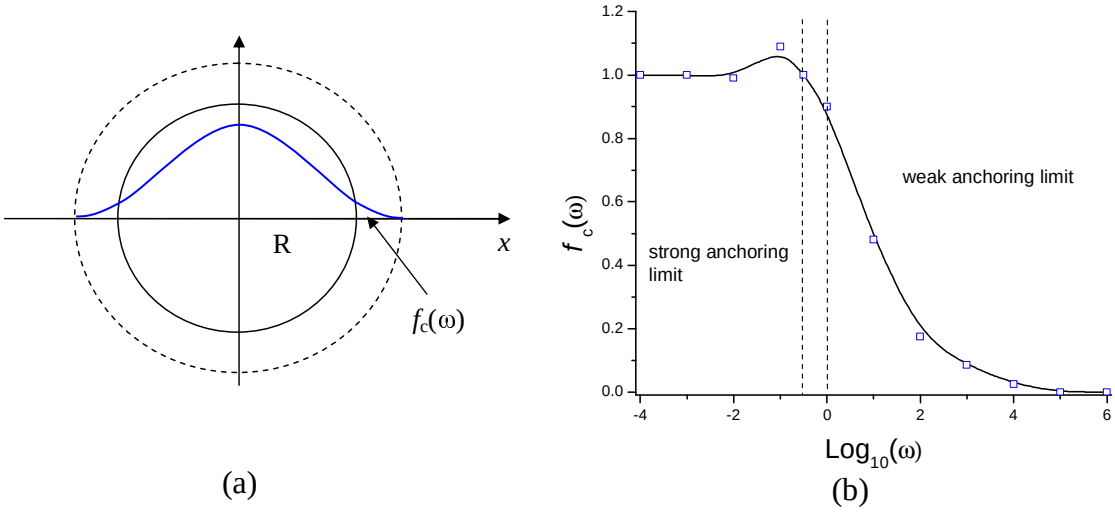

Figure 2.21. Finite anchoring on the cylindrical geometry. (a) The deviation angle is not fixed to be zero at the boundaries, which can be extrapolated to be zero after extrapolation length. (b) The numerical calculation of the dimensionless function $f_c(\omega)$. When $\omega \to 0$ (strong anchoring limit), the function $f_c(\omega)$ approaches 1.

2.5.3 Fréedericksz Transition in 3D Confinement: Wu' Model

In 1989 Wu and co-workers presented an ellipsoid droplet model to explain the electro-optic response of a conventional PDLC.[126] The director configuration in the droplet is assumed to be bipolar as seen in Figure 2.22 (a), which was verified by computer simulations with a homogeneous alignment on the surface.[127] The bipolar configuration is the most common configuration observed in PDLC systems. The director of the droplet **n** is also shown in Figure 2.22 (a). By applying an electric field the director **n** responds to the external field and reached an equilibrium state $\mathbf{n}_{eq}$. The geometry is seen in Figure 2.22 (b).

The free energy of the external field can be approximately expressed as

$$F_{em} = -\frac{1}{2}\Delta\epsilon\epsilon_o E^2 \sin^2(\lambda) \tag{2.117}$$

where λ is the angle between the director of the droplet n and the electric field E. Here we use the approximation that the director field distribution in the droplet is substituted

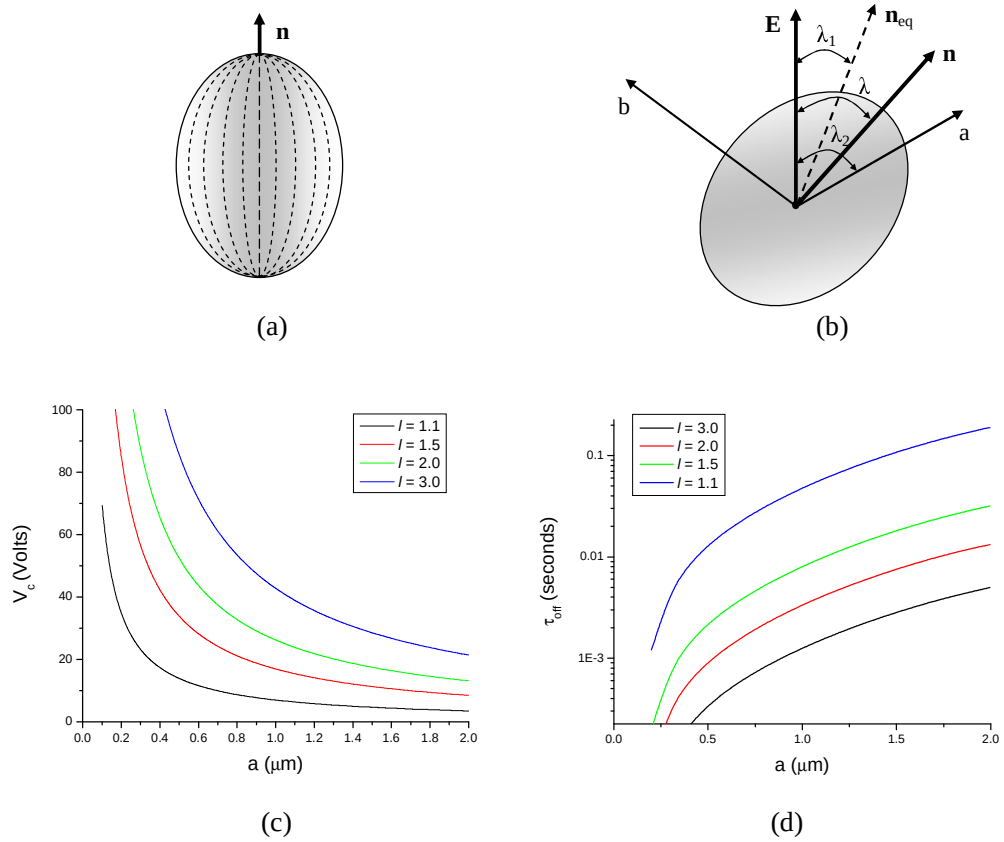

Figure 2.22. Wu's ellipsoid bipolar droplet model. (a) bipolar configuration of an ellipsoid droplet. (b) Illustration of the droplet director n under external field. (c) The critical voltage of a typical 5μm PDLC sample as a function of droplet radius a and aspect ratio of the droplet l. (d) The response time τ_{off} of a typical 5 μm PDLC sample as a function of droplet radius a and aspect ration l.

by the director of the droplet. Assuming a uniform field inside the droplet, the electric torque Γ_{em} is given by

$$\Gamma_{em} = \frac{dF_{em}}{d\lambda} = \frac{1}{2}\Delta\epsilon\epsilon_o E^2 \sin(2\lambda) \tag{2.118}$$

The elastic energy F_{el} can be expressed as

$$F_{el} = \frac{k}{2\rho^2} \tag{2.119}$$

where ρ is the radius of curvature at the spatial point. In Wu's model the radius of curvature

$$\rho = \sqrt{a^2\cos^2(\lambda_2-\lambda)+b^2\sin^2(\lambda_2-\lambda)} = a\sqrt{\cos^2(\lambda_2-\lambda)+l^2\sin^2(\lambda_2-\lambda)} \quad (2.120)$$

was taken to be the radius of curvature of the equator at the droplet edge. Here a and b are the lengths of the semi-major and semi-minor axes, respectively. $l = a/b$ is the aspect ratio of the droplet. Therefore the elastic torque Γ_{el} becomes

$$\Gamma_{em} = \frac{dF_{em}}{d\lambda} = -\frac{K(l^2-1)}{2a^2}\sin 2(\lambda_2-\lambda) \quad (2.121)$$

Balancing the elastic and electric torques we can find the direction of $\mathbf{n}_{eq}$

$$\lambda_1 = \frac{1}{2}\tan^{-1}\left(\frac{\sin(2\lambda_2)}{A+\cos(2\lambda_2)}\right) \quad (2.122)$$

where $A = \Delta\epsilon\epsilon_o E^2/K(l^2-1)$. Specifically, when $\lambda_2 = \pi/2$, there is a critical field given by

$$E_c = \frac{1}{a}\left[\frac{K(l^2-1)}{\Delta\epsilon\epsilon_o}\right]^{1/2} \quad (2.123)$$

In PDLC systems the electric field is not uniform since the dielectric constant of the polymer and liquid crystal are not the same. Under a single droplet approximation the electric field inside the droplet (E) and the applied voltage (V) have a relation[112]

$$E = \frac{3\epsilon_p}{2\epsilon_p+\epsilon_{lc}}\frac{V}{d} \quad (2.124)$$

and

$$E =_{\omega\to 0} \frac{3V}{d}\left(\frac{\sigma_{lc}}{\sigma_p}+2\right) \quad (2.125)$$

where ϵ_p and ϵ_{lc} are the dielectric constants of the polymer and liquid crystal, σ_p and σ_{lc} are the conductivities of the polymer and liquid crystal, and d is the thickness of the PDLC sample. Thus the critical voltage V_c can be expressed as

$$V_c = \frac{d}{3a}\left(\frac{\sigma_{lc}}{\sigma_p}+2\right)\left[\frac{K(l^2-1)}{\Delta\epsilon\epsilon_o}\right]^{1/2} \quad (2.126)$$

Similar with the 1D case, by introducing viscosity torque $\gamma\partial\lambda/\partial t$, we can deduce the response times

$$\tau_{on} = \frac{\gamma}{\Delta\epsilon\epsilon_o E^2 + K(l^2-1)/a^2} \tag{2.127}$$

and

$$\tau_{off} = \frac{\gamma a^2}{K(l^2-1)} \tag{2.128}$$

In Figure 2.22 (c) and (d) the critical voltage V_c and response time τ_{off} is calculated for a 5 μm sample as a function of the radius of the droplet a. Different aspect ratios, l, are considered. The parameters are set to be $K = 10$ pN, $\sigma_{lc}/\sigma_p = 25$, $\Delta\epsilon = 10$ and $\gamma = 0.1$ Pa·s. For a PDLC film with $a = 1\mu$m and $l \sim 1.5$ the value of $V_c \sim 15$ V and $\tau_{off} = 8$ ms are obtained.

2.6 Summary

This chapter has discussed the major topics concerning holographic polymer dispersed liquid crystals; such as different modes of operation (transmission and reflection), materials systems used to fabricate H-PDLCs, formation kinetics, light propagation in H-PDLC periodic dielectric medium and electro-optical properties. This chapter serves as a basis as well as a reference for the experimental results section that follows.

CHAPTER 3

HOLOGRAPHIC POLYMER DISPERSED LIQUID CRYSTAL EXPERIMENTAL STUDIES

3.1 Formation and Materials

We have investigated the effects of monomer functionality on the formation and switching characteristics of holographic gratings synthesized in polymer-dispersed liquid crystal cells by using 632.8 nm wavelength of a He-Ne laser. Here we present results for the micro-structure, diffraction efficiency, and switching characteristics for both Raman-Nath and Bragg transmission gratings utilizing E8/E7 liquid crystals along with monomers having varying functionality from 2.0 to 4.0. For monomers having functionality greater than 2.5 it is seen that a large increase in diffraction efficiency up to the theoretical limit $\eta \approx 34\%$ in Raman-Nath is achieved while an efficiency of 50% is achieved in Bragg regime, with fields required for switchable gratings being around 17 MV/m.

3.1.1 Experimental Details

The diffraction efficiency and switching characteristics of H-PDLCs were studied by recording holograms with the experimental setup shown in Fig. 3.1. A thermally stabilized 0.8 mW He-Ne laser beam (labeled as the write beam) is expanded and re-collimated to 0.5 cm diameter by a beam expander. The use of a thermal feedback stabilizer for the He-Ne laser was to allow for long time periods (typically 30-60 min) of temporal stability during the cure process at the current power densities used in the experiment. The re-collimated beam is then split into two beams directed at the H-PDLC mixture to form an interference pattern. The H-PDLC, mounted on a 360-degree mount, is rotated such that the probe beam enters the H-PDLC along the normal to

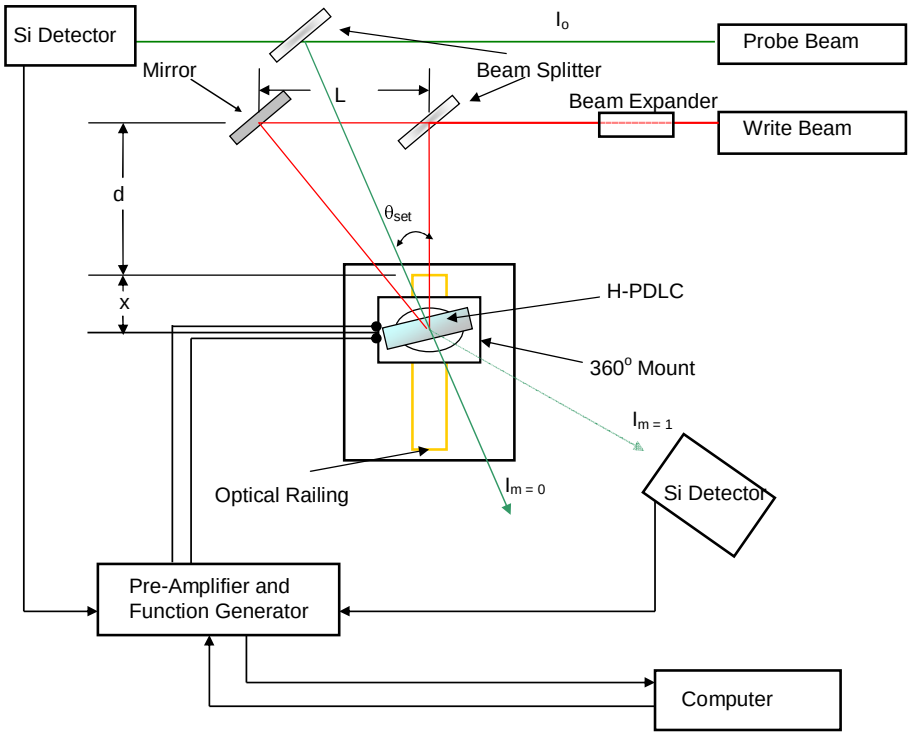

Figure 3.1. Optical setup for Recording a two-beam transmission mode H-PDLC.

the H-PDLC surface and simultaneously bisects the angle ($2\theta_{set}$) between the two pump beams. The irradiance of the two pump beams incident at the holographic medium are 0.25 mW/cm^2. The angle θ_{set} is given by,

$$\theta_{set} = \frac{1}{2}\tan^{-1}\left(\frac{L}{(d+x)}\right) \tag{3.1}$$

The corresponding value of the grating period (Λ) is related to θ_{set} according to,

$$\Lambda = \frac{\lambda_{pump}}{2\sin(\theta_{set})} \tag{3.2}$$

Before starting the curing process the intensity of the impinging pump beam was measured and was utilized in determining the self-diffraction efficiency measurements during the cure process. The diffraction efficiency (η), defined by

$$\eta = \frac{I_{m=1}}{I_o} \tag{3.3}$$

is obtained by measuring the intensity of the incident probe beam (I_o) and the intensity of the first-order diffraction beam ($I_{m=1}$) using Si-photodiodes and associated electronic modules. For the determination of the switching characteristics of the gratings, an Advance Instruments oscillator was used to apply external electric fields to H-PDLCs.

For the synthesis of the H-PDLC's, such as with our PDLCs[128, 129], we utilized different mixtures of a polymerizable matrix and a thermotropic liquid crystal, E8 (Merck), with a nematic mesophase at room temperature. Photo-polymerization of the monomers was initiated by using a photoredox-catalysis mixture, consisting of a photo-oxidant dye, Methylene Blue, and co-initiator, *p*-toluenesulfonic acid. All samples were prepared with 30 wt% Liquid crystal, 68 wt% polymerizable matrix material and 2 wt% photoredox-catalysis mixture. Prior to mixing with the monomer and LC, the photoredox-catalysis mixture was diluted with de-ionized water at a ratio of 25mL de-ionized water to 1.0g of Methylene Blue and 0.8g of *p*-toluenesulfonic acid producing concentrations of 0.12 x $10^{-3}M$ and $0.21M$ respectively. Our polymerizable matrix consisted of a mono-functional acrylic oligomer (CN-135), with a functionality slightly larger than one and a tetrafunctional crosslinker (functionality 4), pentaerythritol tetraacrylate (SR-295), at various fractions of the total monomer mass. Most of the oligomer units are hydroxyl-terminated, making them somewhat unreactive in crosslinking chemistry during photo-polymerization. The majority of the crosslinking in the cure process is done with pentaerythritol tetraacrylate. Chemical structures of the photoredox-catalysis mixture and polymerizable matrix components used are given in Fig. 3.2. (Note that the exact chemical composition of oligomers, such as CN-135, are not revealed by the raw material suppliers for reasons of confidentiality.) Both CN-135 and SR-295 were obtained from Sartomer and used as received. The photoinitiator, Methylene Blue, as well as the co-initiator, *p*-toluenesulfonic acid (Reagent grade), were from ScienceLab and were used without purification.

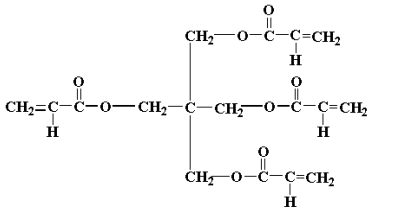

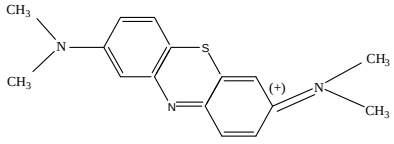

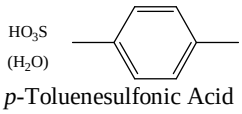

Figure 3.2. Chemical structure of monomer: pentaerythritol tetraacrylate (SR295) and photoredox-catalysis mixture agents: Methylene Blue and *p*-toluenesulfonic acid.

The H-PDLC polymerizable matrix mixtures were formulated to yield composite monomer functionalities that were calculated from the relative percentages of each constitute monomer. The oligomer/monomers CN-135 and SR-295 were mixed with the average functionality being calculated from[130]

$$\mathcal{F} = \sum_i \phi_i f_i \tag{3.4}$$

where ϕ_i is the percent mass of monomer i with a functionality f_i. By varying the fractional percent of the oligomer and the monomer we obtained values of functionality ranging from 1 to 4 in half step increments. The polymerizable matrix mixtures and their percent weight along with calculated average functionalities used in this study are shown in Table 3.1. These functionality values, in general, indicate the average number of acrylate double bonds which have an inherent reactivity during crosslinking. Generally speaking: the lower the functionality, the lower the reactivity.

Table 3.1. Polymer mixtures used to study the effects of crosslinking.

	CN-135	SR-295	$\mathcal{F}$
Sample-1	1.00	0	1
Sample-2	0.83	0.17	1.5
Sample-3	0.65	0.35	2
Sample-4	0.50	0.50	2.5
Sample-5	0.35	0.65	3
Sample-6	0.17	0.83	3.5
Sample-7	0	1.00	4

All samples were prepared by introducing the H-PDLC material, *via* capillary action, between ITO glass plates pre-gapped employing UV optical adhesive (NOA-65) and fiber spacers (10 μm), at about 1% by mass. The average H-PDLC cell thickness of 10 μm, was confirmed by cross-section analysis utilizing optical microscopy. The structures of the cured gratings were examined by using a 400x Nikon Optiphot polarizing microscope.

3.1.2 Results

For each of the different H-PDLC samples, shown in Table 3.1, two types of measurements were carried out: (1) time evolution of the self-diffraction efficiency of the grating and (2) optical microscopy of the grating structure after saturation of the diffraction efficiency (cured gratings). We adjusted the experimental parameters to provide θ_{set} = 3.5^o which according to eqn. (2) corresponds to Λ = 5.2 μm.

The time evolution of the measured first-order (m=1) self-diffraction efficiency for the H-PDLC samples are shown in Fig. 3.3. The cure-time for all samples was approximately 50 min. We observe significantly different values of the final diffraction efficiencies (η_{max}) depending upon the functionality of the polymerizable matrix. For example, in the case of Sample-7, which is characterized with a functionality of 4, η_{max}

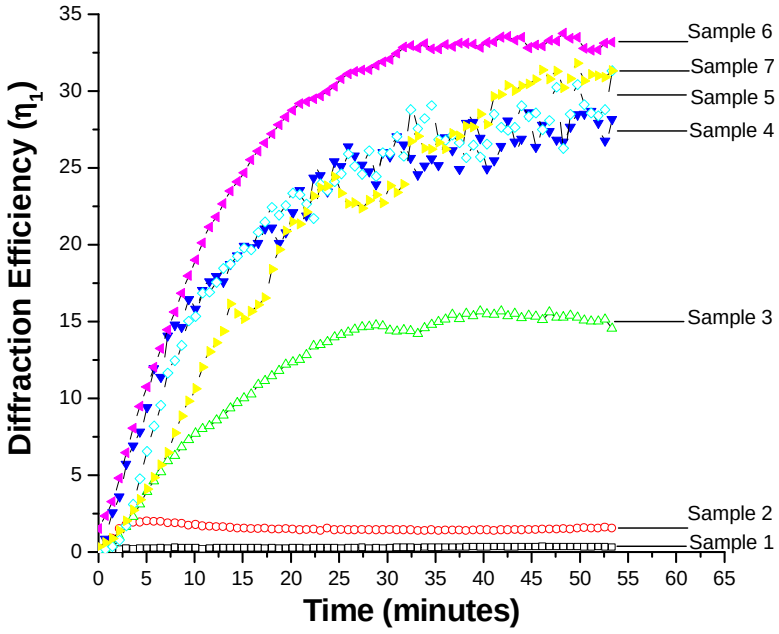

Figure 3.3. Time dependent self-diffraction efficiency for H-PDLC samples with varying polymerizable matrix functionality.

$\approx$ 30% while for Sample-2, with a functionality of 1.5, η_{max} is only about 1%. Fig. 3.4 summarizes the final diffraction efficiency for the first-order diffracted beam vs the average functionality of the grating. The increase in diffraction efficiencies is quite pronounced after an average functionality of $\mathcal{F} = 2.0$. The diffraction efficiency appears to peak for an average functionality of approximately $\mathcal{F} = 3.5$ with efficiencies nearly 34%. Increasing the average functionality beyond this shows a small depreciation in diffraction efficiency to around 30% for $\mathcal{F} = 4.0$. Although there is a small change in diffraction efficiencies achieved for average functionalities between $\mathcal{F} = 2.5$ and $\mathcal{F} = 4.0$ their is a difference in the polymerization rate, morphology and grating formation rate as seen in Fig. 3.3, with Sample-7 having a longer time evolution and steeper slope of formation than the other gratings. This could be attributed to the initial amount of inhibitors in SR-295 and also viscosity and diffusive effects. At either rate, this effect does not in any way effect the final diffraction efficiency achieved by the sample.

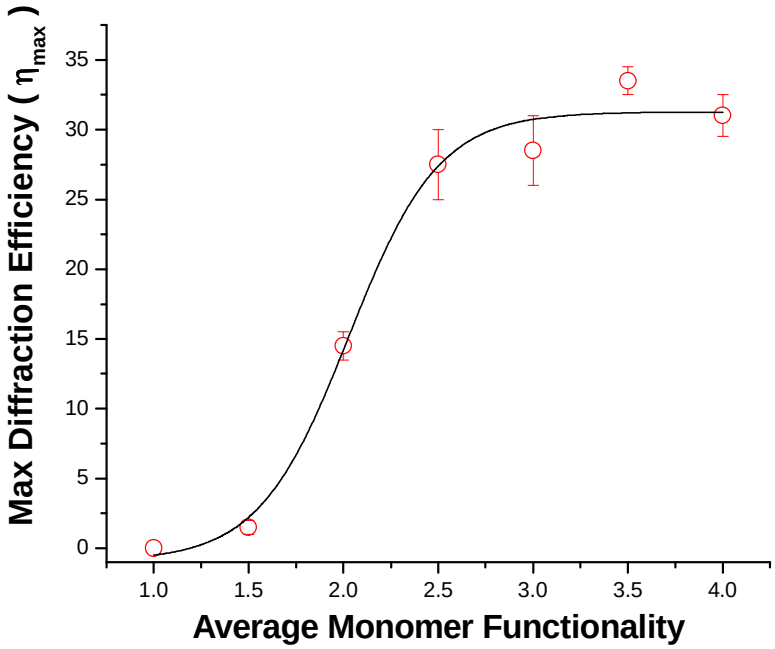

Figure 3.4. Average functionalities of polymerizable matrix mixtures plotted with maximum achieved diffraction efficiency (η_{max}).

Given the low functionality of Sample-1 we never observed formation of a sufficient diffraction grating in the time period studied. This may be due to the *softness* of the cure. With lower functionality monomers the LC droplets have a longer period to coalesce and become larger than critical size for grating use (sub-micron size), see Fig. 3.5. As the functionality increases in the polymer matrix the photo-polymerization process reacts much more rapidly in crosslinking and establishing a grating formation, producing a more pronounced grating morphology with higher diffraction efficiencies. An additional sample utilizing the same formulation of Sample-1 was allowed to cure for several hours. The outcome was a small formation of varying degrees of stratified LC/polymer zones, but no substantial diffraction efficiency was observed. Observation of this addition sample yielded a significant bleaching of the photo-oxidant dye over a period of a few hours, at which time the photo-polymerization process is complete and their are few polymer

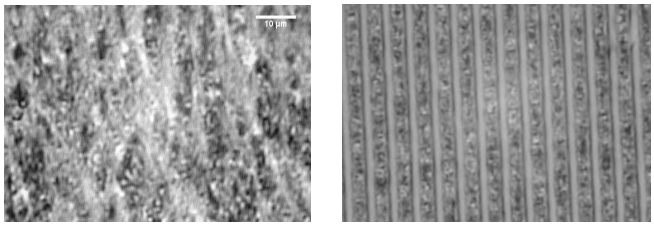

(a) (b)

Figure 3.5. Micrographs of samples with functionality of one $\mathcal{F} = 1$ (a) and functionlaity of $\mathcal{F} = 3.5$ (b).

chains that will continue to cure before they terminate crosslinking and the grating is fully cured.

The increase in diffraction efficiency for samples with increasing functionality is consistent with the established grating morphology as seen in Fig. 3.6. Here we examine the effect of functionality on the phase-separated morphology of the H-PDLC samples. We see from the micrographs of fully cured H-PDLC gratings that the dark regions are rich in E8 liquid crystals, the brighter regions are monomer rich. The grating microstructure of H-PDLC samples with average functionalities of 3.0, 3.5 and 4.0 (Samples-5,6,7) consist of spatially periodic liquid crystals domains of perceivable liquid crystal size distributions separated by polymer planes. The liquid crystal domains appear to be globulous of sizes ranging from 0.5μm to 3.0μm. Some long range connectivity among the liquid crystal domains is also seen for the higher functionality samples. The liquid crystal domains are less distinct and even imperceivable for the samples with functionalities less than 3.0. With functionality 2.5 and less, the liquid crystal domains suddenly become much smaller, the liquid crystal-rich regions are devoid of any perceivable liquid crystal domains and resemble the typical scaffolding appearance of H-PDLCs. If the time for the liquid crystal to diffuse across $\Lambda/2$ is slow compared to the time for full polymerization to occur, the growth of droplets is diminished and vitrification and entrapment occurs and the grating morphology is not developed (Sample-1). On the other hand if

the time for the liquid crystal to diffuse is much faster compared to polymerization rates the liquid crystal has sufficient time to migrate across the distance $\Lambda/2$ (Sample-6). The consequence is that most, if not all, the liquid crystal is squeezed into channels caused by the growing polymer network. This results in a "perfect" grating formation in which all the liquid crystal is concentrated in the low intensity region of the interference pattern and the polymer is concentrated in the hight intensity region. The phase separation in the lower functionality samples have a grating morphology, but what appears to be an absence of visible liquid crystal domains. This absence of visible liquid crystal domains might be partially attributed to an entrapment effect. This effect could be brought about by low functionality monomers diffusing into the high intensity regions of the interference pattern while a LC/monomer mixture remains in the low intensity regions. As the polymer network continues to grow it reaches a point where continued growth and coalescence of the liquid crystal droplets is stopped. In the case of entrapment the polymer network growth stopes but a gelation of LC/monomer occurs and phase separation of the liquid crystal is incomplete. So less liquid crystal is able to phase separate out and create large regions of liquid crystal in the low intensity regions and in turn reduce the diffraction efficiency

It is also interesting to note from the micrographs that the ratio of the width of liquid crystal regions to the polymer regions increases with an increase in average functionality from 1.0 to 3.0. This ratio indicates the relative contributions of each of those regions in a single grating spacing. In the case of the gratings with functionality 3.5 and 4.0, the ratio the width of liquid crystal and polymer regions is again expected to follow the same trend. With Sample-6 and Sample-7 we see, given the appearance of large liquid crystal globulous, the liquid crystal has phase separated out and we suspect the ratio of liquid crystal to polymer to have even increased over that of Sample-5. These effects in LC/polymer ratios are understood to be directly related to monomer

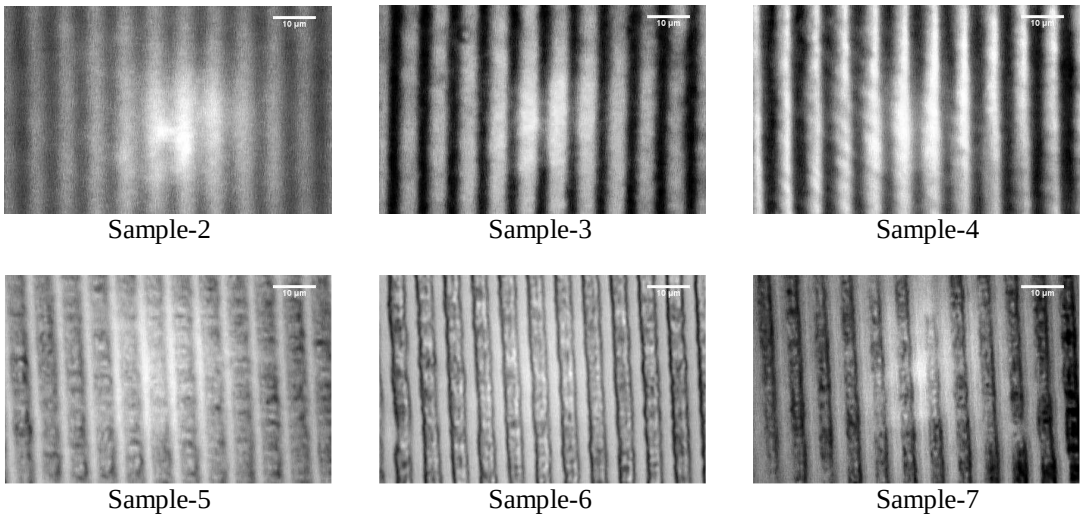

Figure 3.6. Micrographs of H-PDLC samples utilizing varying functionalities of polymerizable matrix. Scale bar is 10μm for each micrograph.

consumption and solubilities in the curing process which in turn is related to phase separation of the liquid crystal and monomer during the grating formation[131].

We have made measurements of the diffraction efficiencies of the H-PDLC samples over relatively long periods (weeks) and observed that the diffraction efficiency, having remained at the η_{max} value for some time, declines after several weeks for the samples. Although the grating morphology is developed within minutes some changes occur on a time scale of hours and days that affect the diffractive properties of the gratings. Because the kinetics of polymerization may be faster than those for the liquid crystal to diffuse some of the liquid crystal may be trapped in a non-equilibrium state following final grating formation. During the period following final grating formation the polymer network undergoes post-polymerization of trapped radicals or a polymer network relaxation leading to a migration and coalescing of liquid crystal. These post-reaction process serve to bring about a more stable equilibrium and may lead to increased scattering and decline in diffraction efficiency. We observed that samples with higher functionalities remained stable for longer time periods. This could be attributed to the stability of the polymer

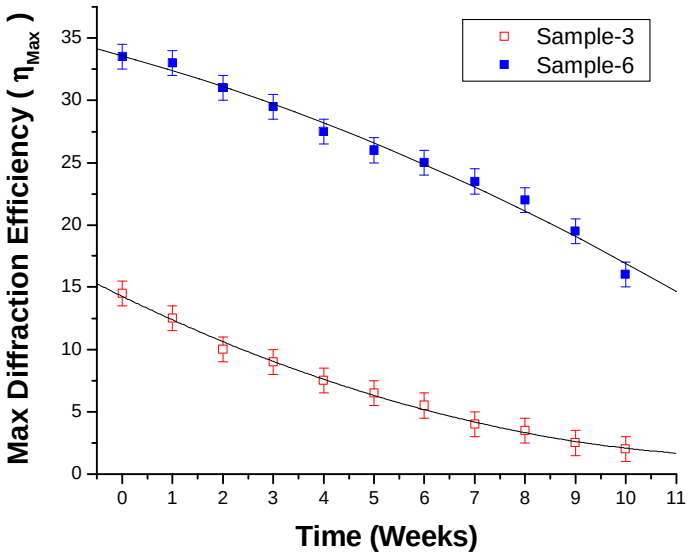

Figure 3.7. Time stability diffraction efficiency for H-PDLC samples.

matrix and higher liquid crystal phase separation that occurred during the cure process which lead to a more chemically stable grating structure initially and less diffusive and coalescing was needed to stabilize the grating. Fig. 3.7 shows the time dependent stability of two of the samples with varying functionalities, particularly Sample-3 and Sample-6. Here we see a decrease in diffraction efficiency of both samples over a 10 week period in which the samples were allowed to remain under ambient conditions. The total change in diffraction efficiency for both samples is 13% for sample-3 and 17% for Sample-6. While the diffraction efficiency has remained constant, within observation error, for several weeks in Sample-6 with up to seven orders of diffraction observed, a decline in efficiency below 25% took six weeks to achieve. These changes over an extended time period of observation could also be attributed to electro-optical degradation from applied switching fields and possible thermodynamic fluctuations about the glass temperature of the polymer thus softening the polymer itself allowing for diffusive/gelation mechanisms to take effect. This slow diffusive effect was verified by optical micrographs which showed

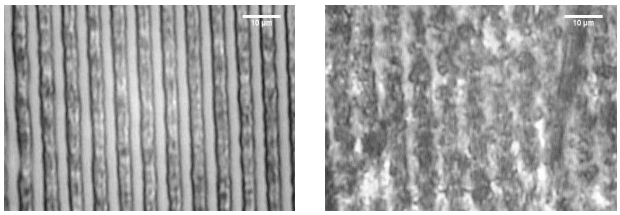

Figure 3.8. Micrographs of Sample-6 at (a) zero weeks and (b) ten weeks.

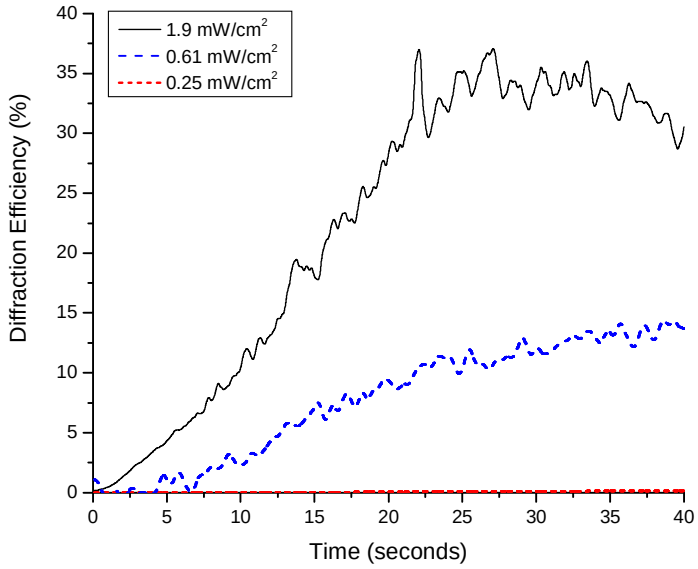

Figure 3.9. Effect of writing beam intensity of the grating formation kinetics.

a depreciation of the grating structure with large regions ($> 10\mu$m) of coalesced liquid crystal droplets forming sporadically within the grating structure (Figure 3.8). One thing to note on stability is that as the writing beam intensity increases the polymerization process proceeds much more rapidly to completion with very little residual diffusive processes with the liquid crystal/polymer occurring after the cure. Gratings written with an increased intensity have show little to no degradation in diffraction efficiency.

The effects of the writing beam intensity on the grating formation dynamics was studied by allowing the writing beam to be attenuated by a neutral density filter. The results are shown in Figure 3.9. Here we see the rapid response of grating formation to

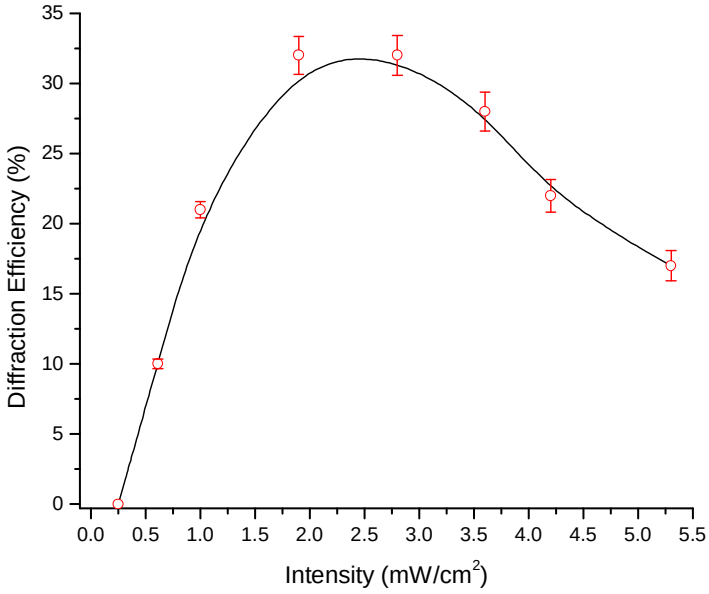

Figure 3.10. Effect of writing beam intensity of the overall achieved diffraction efficiencies.

the writing beam intensity. For intensities over 1.9 mW/cm^2 the diffraction efficiency and thus the morphology develops quite rapidly leading to a well defined grating structure in 30 seconds. As the intensity is decreased the grating development takes much longer to develop and establish a detectable diffraction efficiency. This effect with laser power does have a maximum value after which high intensities begin to cure the polymer to rapidly with detrimental effects to the overall achieved morphology and diffraction efficiency (see Figure 3.10). In Figure 3.10 we see the effects on the overall achieved diffraction efficiency in H-PDLC gratings that are exposed for 60 seconds.

Effects of externally applied electric fields on the first-order diffraction efficiency for all the H-PDLCs (excluding Sample-1 and Sample-2) were determined to be affected appreciably by the functionality of the monomer. These results are seen in Fig. 3.11. These data reveal the effects of functionality on the electro-optical characteristics of the diffractive grating. Here we have studied the effects of the rms-amplitude of a 1-kHz electric field on the diffraction efficiencies of the cured gratings. The diffraction

Table 3.2. Switching properties of H-PDLCs with varying functionalities

	Functionality ($\mathcal{F}$)	"Switch-Off" Fields
Sample-3	2	23 (MV/m)
Sample-4	2.5	23 (MV/m)
Sample-5	3	17 (MV/m)
Sample-6	3.5	16 (MV/m)
Sample-7	4	19 (MV/m)

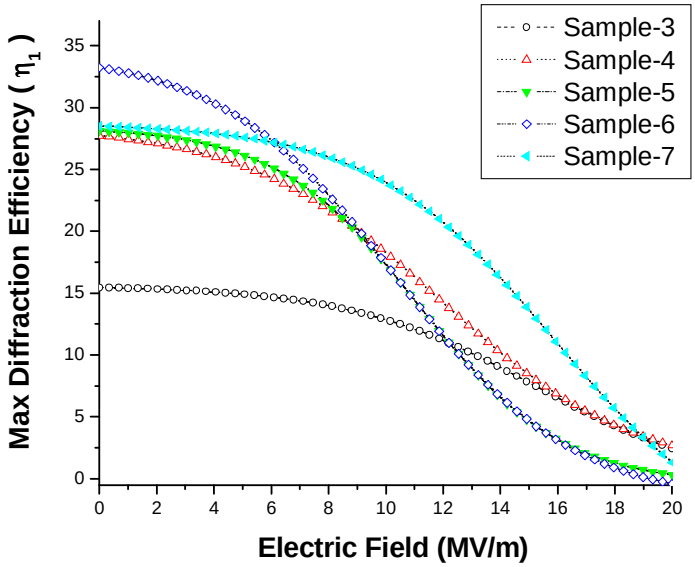

Figure 3.11. Electric field dependence of diffraction efficiency for H-PDLCs.

efficiencies of the gratings decreased with increasing rms-amplitude of the electric field. The diffraction efficiency of Sample-1 could not be obtained due to the non-formation of diffractive gratings during cure. A value for the "switch-off" ($\eta \approx 0$) electric field was extrapolated from the acquired data for samples with switching fields beyond 15 MV/m. The results of Fig. 3.11 are summarized in Table 3.2. Here we see that the switching fields vary from $>$ 20 MV/m for Sample-3 to 15 MV/m for Sample-6. These differences in the switching voltages of the gratings are attributed to effects related to H-PDLC morphology and/or LC/monomer interfacial effects that are obtained during the cure process (i.e. anchoring energies, LC director orientation; tangential or normal

to the interface, etc.). A comparison between the functionalities of the monomer show a somewhat inverse effect on the switching voltages; meaning the higher the functionality the higher the diffraction efficiencies but also lower the required switching fields. As the monomer functionality increases the micro-structure of the gratings becomes sharply defined and the LC is assumed to have phase separated out in larger ratios compared to the polymer. When this happens the larger majority of the LC has formed larger globules and thus lowering the switching fields required for LC director orientation. This observation is consistent with previously published results that show critical values for the switching electric fields for PDLCs decreases with an increase in the size of a spherical LC droplets.[132]

3.2 Raman-Nath and Bragg Transmission Gratings

In this section we discuss the formation of switchable holographic transmission gratings in polymer dispersed liquid crystals fabricated utilizing the 632.8 nm wavelength of He-Ne laser.[133] We discuss the structure, diffraction efficiency, and switching characteristics of the gratings. From a technological point of view, the constituent materials for the H-PDLCs and the recording laser wavelength are two of the most important parameters that influence the electro-optical properties and commercial usage of the gratings. Given the abundance and low cost of He-Ne lasers and red diode lasers, we have investigated the feasibility of recording an H-PDLC grating by utilizing the 633 nm wavelength of the He-Ne laser. Although, photopolymer gratings have been written using the He-Ne radiation,[14] to our knowledge, there are no published reports on H-PDLC gratings written with He-Ne lasers.

Table 3.3. Concentrations used for H-PDLC samples

	CN135	SR295	p-c mixture	E8
Sample-1	48%	25%	2%	25%
Sample-2	45%	23%	2%	30%

3.2.1 Experimental Details: Raman-Nath

We have used mixtures consisting of a polymerizable matrix and E8 liquid crystal. The matrix consisted of a monofunctional acrylic oligomer, CN135, with functionality slightly larger than one and a tetrafunctional cross linker, SR295, at various fractions of the total monomer mass. Most of the oligomer units are hydroxyl-terminated, making them unreactive in crosslinking chemistry during photocuring. Photopolymerization of the monomer was initiated by using a photoredox-catalysis mixture, consisting of a photo-oxidant dye, Methylene Blue, and *p*-toluenesulfonic acid (Merck). The samples were prepared by introducing the H-PDLC composite material, *via* capillary action, between ITO glass plates pre-cured with a pattern made by UV optical adhesive (NOA-65) and spherical ceramic particle spacers (SR1124, Sartomer), at about 1% by mass. The average PDLC cell thickness was 10 μm, as determined by cross-section analysis by optical microscopy. Prior to mixing with the monomer and LC, the photoredox-catalysis (p-c) mixture was diluted with de-ionized (DI) water at a ratio of 25mL of DI water to 1.0g of Methylene Blue and 0.8g of *p*-toluenesulfonic. The H-PDLC compositions of two H-PDLCs used in this study are shown in Table 3.3.

The diffraction efficiency and switching response of two H-PDLCs were studied by recording the holograms with the experimental setup shown in Fig. 3.1. A 0.8 mW He-Ne laser beam (labeled as the pump beam) is expanded and recollimated to 0.5 cm diameter by a beam expander. The recollimated beam is split into two beams directed

at the H-PDLC to form an interference pattern. The H-PDLC, mounted on a 360-degree mount, is rotated such that the probe beam enters the H-PDLC along the normal to the H-PDLC surface and simultaneously bisects the angle ($2\theta_{set}$) between the two interference beams. The irradiance of the two interference beams incident at the holographic medium are adjusted to be about equal with typical exposure irradiance of 0.25 mW/cm^2. The optical system of Fig. 1 allows for the two beams to interfere at any angle ($2\theta_{set}$), ranging from 1^o to 30^o. The angle θ_{set} is given by, $\theta_{set} = 1/2\tan^{-1}(L/(d+x))$ The corresponding value of the grating period (Λ) is related to θ_{set} according to,$\Lambda = \lambda_{pump}/2\sin(\theta_{set})$ The diffraction gratings written with the 633 nm wavelength of the He-Ne laser, under our experiment conditions, are characterized with grating periods ranging from about 0.63 μm to 18 μm. The diffraction efficiency (η), defined by $\eta = I_{m=1}/I_o$ was obtained by measuring the intensity of the incident probe beam (I_o) and the intensity of the first-order diffraction beam ($I_{m=1}$) using Si-photodiodes and associated electronic modules. For the determination of the switching characteristics of the gratings, again an Advance Instruments oscillator was used to apply external electric fields to H-PDLCs.

3.2.2 Results: Raman-Nath

In the present series of experiments, we adjusted the experimental parameters to provide $\theta_{set} = 3.5^o$ and a corresponding $\Lambda = 5.2$ μm. Two sets of measurements were made: (1) time evolutions of the self-diffraction efficiency of the grating, (2) optical microscopy of the grating structure after saturation of the diffraction efficiency (cured gratings). The structures of the cured gratings were examined by using 200x Nikon Optiphot microscope. A typical diffraction pattern, clearly showing the characteristic m = 0, 1, and 2 interference spots, and the micro-structure of two H-PDLC cured-gratings are shown in Fig. 3.12. Whereas the dark regions are rich in LC droplets, the brighter regions are polymer rich. The dark regions also correspond to minima in

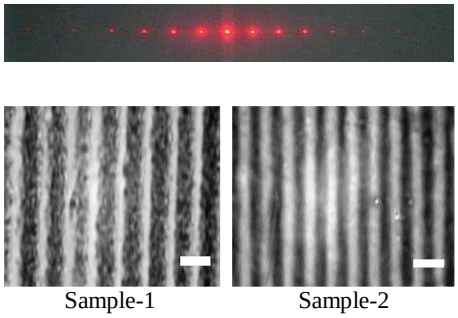

Figure 3.12. Typical diffraction pattern and gratings formed in two different H-PDLCs, listed in Table 3.3. The scale bar is 10 μm.

the interference pattern. These results can be understood by considering the chemical potential of the LC and polymer.[134, 135] The polymerization, due to the high rate of free radical production because of absorption in Methylene Blue, begins in the high-intensity regions of the interference pattern. The consumption of the monomers in these regions lowers their chemical potential, which in turn gives rise to diffusion of additional monomers from the lower-intensity regions towards the higher-intensity regions. During this process the LC molecules are not consumed by the polymerization process and their chemical potential increases in the high-intensity regions over that in the lower-intensity regions. Hence, there is diffusion of LC molecules from high to low-intensity regions to equalize the chemical potential within the interference pattern.

The time evolution of the measured first-order self-diffraction efficiency for both H-PDLCs is shown in Fig. 3.13. These data show typical three regions that characterize the dynamic growth of the diffraction grating. Initially there is a short induction period ($\leq$ 100 s) during which all inhibitors, e.g. oxygen or those supplied by the manufacturer to prevent accidental polymerization, have reacted. Next there is a period ($\sim$ 1500 s) of polymerization and photobleaching of the Methylene Blue with an associated rise in diffraction efficiency. Finally a plateau region occurs within which the polymerization is almost complete and the dye molecules are considered bleached. The temporal evolution

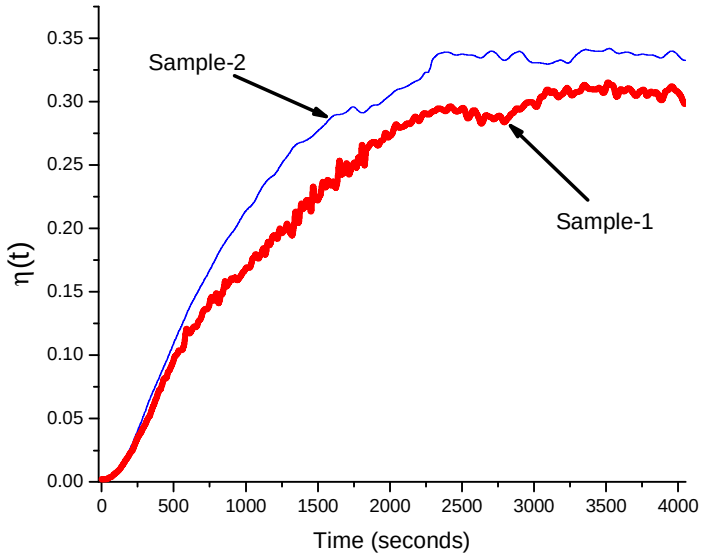

Figure 3.13. Time dependent diffraction efficiency for two different H-PDLCs.

of the gratings (Fig. 3.13) follows qualitatively the same behavior for both samples. We observe $\eta_{max} \approx 30\%$ and 35% for sample-1 and sample-2, respectively. It should be noted that the higher diffraction efficiency observed for sample-2 is consistent with a relatively sharper grating structure of this sample seen in Fig. 3.12. Additionally, the observed rise in the diffraction efficiency with time can be characterized with time constants of about 20 and 15 mts for sample-1 and sample-2, respectively. We have made measurements of the diffraction efficiencies of the H-PDLC samples over relatively long periods (weeks) and observed that the diffraction efficiency, having remained at the η_{max} value for a few days, declines slowly after a few weeks to be unmeasurable. This has been attributed to losses due to electric field degradation, thermal effects in the glass temperature of the monomer, and losses due to slow diffusive mixing between the polymer and the LC.

The H-PDLC was positioned in a rotational mount so the study of the angular selectivity could be evaluated. Fig. 3.15 shows typical results from these measurements.

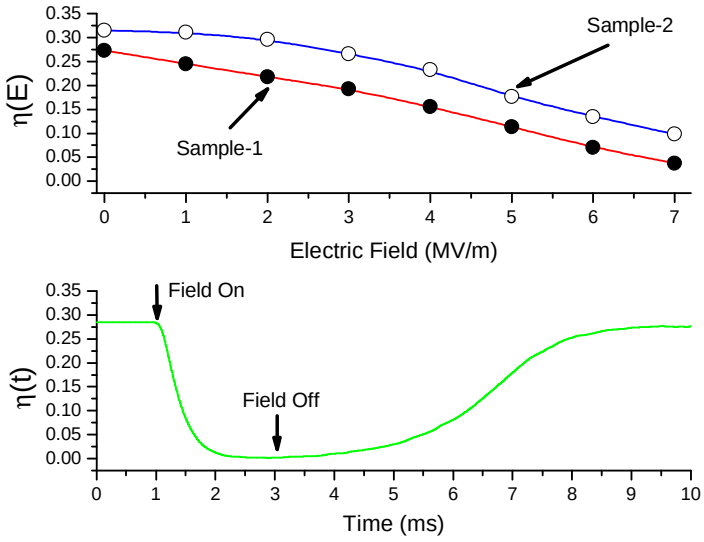

Figure 3.14. Electric field dependence of diffraction efficiency for H-PDLCs.

Here we fitted the first order diffraction efficiency of a Raman-Nath grating utilizing equation (2.36). The fitting parameters are given as $L = 10\mu$m, $\lambda = 632.8$ nm and $n_1 = 0.0182$. One sees the efficiency of the diffracted first order is very sensitive to the incident angle of the probe beam. In this sample the diffraction efficiency of 34% was normalized to one and an angular selectivity can be seen of about 10^o full width at half max.

The switching characteristics of the H-PDLCs, effects of externally applied electric fields on the first-order diffraction efficiency, are shown in Fig. 3.14. Here we present data from two differently conducted experiments. In one experiment, we have studied the effect of the rms-amplitude of 1-kHz electric field on the diffraction efficiencies of the cured gratings utilizing the probe beam in our experimental setup(0.3mW 633nm). The application of an electric field across an H-PDLC grating significantly changes the orientation of the LC droplets along the field direction and eliminates the spatial variation in the refractive index thus the diffraction grating is "erased". The diffraction efficiencies of both gratings are seen to decrease with increasing rms-amplitude of the electric field; the efficiency of sample-2 remaining higher than that of sample-1. A value for the "switch-

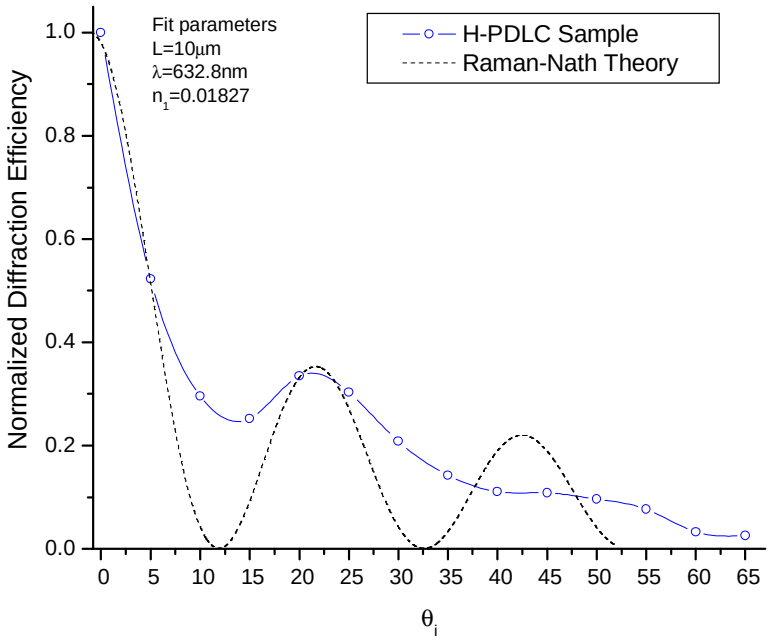

Figure 3.15. Diffraction efficiency as a function of incident angle for a Raman-Nath transmission grating.

off" electric field can be estimated to be approximately 10 MV/m from an extrapolation of these data. In the second experiment, we have investigated the effect of the application of a particular rms-amplitude of the electric field (7 MV/m @ 1 kHz) on the time constants for the decay and recovery of the grating efficiency. The diffraction efficiency of the grating, prior to the application of the electric field, is about 30%. Under the influence of 7 MV/m @ 1 kHz electric field (from about 1 until 3 ms), the diffraction efficiency decreases in time with a time constant of about 1 ms and reaches its lowest value at about 2.5 ms. Once this electric field is removed (at about 3 ms), the diffraction efficiency begins to recover and approaches its initial value of about 30% at about 8 ms. The recovery can be characterized with a relaxation time constant of about 4 ms. The differences in the switching characteristics of the two gratings are possibly due to effects related to H-PDLC morphology and/or LC/polymer interfacial effects. A comparison between the

LC droplet size distributions in these samples shows that sample-1 contains much larger LC droplets (average droplet sizes in sample-1 and sample-2 were ~ 1 and ≤ 0.25 μm, respectively). This observation is consistent with previously published results that the critical value for the switching electric field for a PDLC decreases with an increase in the size of the spherical LC droplets.[132]

3.2.3 Experimental Details: Bragg

The recipe for the prepolymer syrup was a solution of the monomer dipentaerythrol hydroxy penta acrylate (DPHPA), with 10-30 wt% of the liquid crystal E7, 10-30 wt % of the crosslinking monomer N-vinylpyrrollidone (NVP), millimolar range by weight of the coinitiator p-toluenesulfinic acid and 10^{-4} M of the photoinitiator dye Methylene Blue. This mixture was homogenized by ultra-sonification and spread between glass slides with 20μm spacers used to set sample thickness. Preparation, mixing and transfer of the prepolymer syrup onto the glass slides, ass in all our experiments, was done in the dark as the mixture is extremely sensitive to light.

After exposure, some samples were rapidly and completely cured by a 5-min exposure to a mercury lamp, while some samples were allowed to fully cure slowly under normal room lights for a period of hours to days. Fully cured samples showed no coloration since the Methylene Blue was completely bleached in the photocuring process. Samples were characterized for angular sensitivity and peak diffraction efficiency using HeNe laser probe beams techniques.

3.2.4 Results: Bragg

The effect of the liquid crystal on the diffraction efficiency was dramatic (see Figure 3.16). In the pure polymer grating, the peak diffraction efficiency was found to be around 2%, while with liquid crystal loadings of around 20% the peak diffraction efficiency rose to

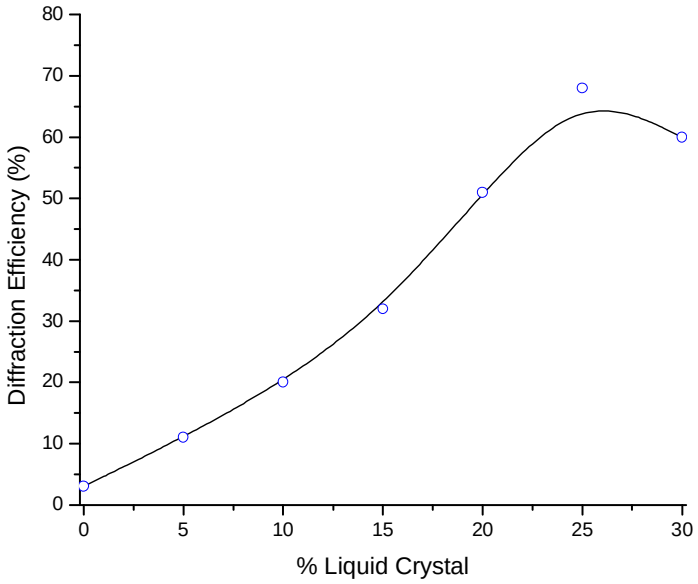

Figure 3.16. Effect of liquid crystal loading in prepolymer syrup for Bragg transmission gratings.

$\sim$ 70 %. While additional loading of liquid crystal served only to reduce the diffraction efficiency. Examples of peak diffraction efficiency and angular sensitivity are seen in Figure 3.17. The grating in Figure 3.17 was recorded with the 632.8 nm line of the HeNe laser and read with s-polarized light. The measured Bragg angle is -14.5^o. These give grating spacings of 845 nm which is in agreement with SEM analysis of the gratings. Theoretical curves in the Figures are fits utilizing coupled-wave theory assuming $n = 1.52$ and index modulation fit parameter of $n_1 = 9.28$ x 10^{-3}.

3.3 Bragg Reflection Gratings

Bragg reflection gratings are holographically recorded in polymer dispersed liquid crystal materials by using the 632.8 nm wavelength of He-Ne laser.[136] Mixtures of commercially available E8 nematic liquid crystal, penta-functional monomers and photo-oxidant dye Methylene Blue are employed. We demonstrate that Bragg reflection gratings can be formed in this acrylate photopolymer system with reflection efficiencies of 52%

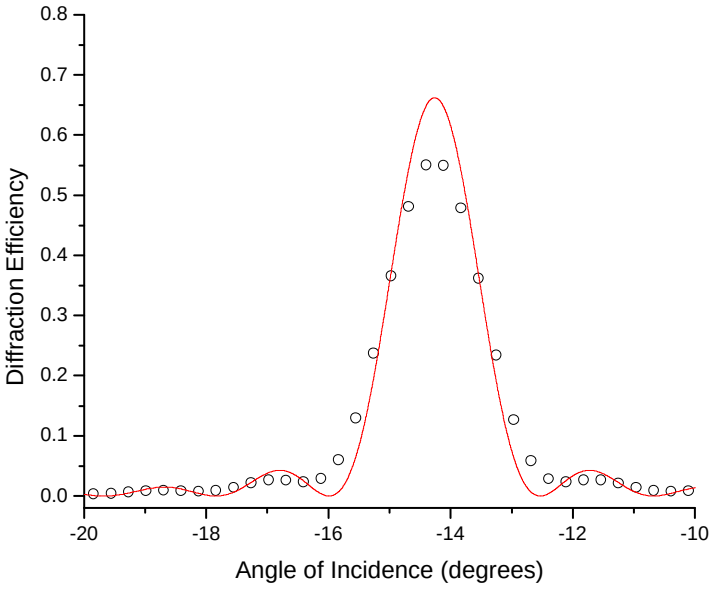

Figure 3.17. Angular sensitivity plot for a Bragg transmission mode H-PDLC sample. The circles are data and the curve is a theoretical fit to coupled-wave theory.

with a peak notch at 1165nm. We also present results for the switching characteristics of these gratings with switching fields on the order of 6 MV/m and rise times of 62μs.

3.3.1 Experimental Details

For the synthesis of the reflection mode H-PDLCs we utilized different mixtures of a polymerizable matrix and a thermotropic liquid crystal, E8 (Merck), with a nematic mesophase at room temperature (n_e=1.771, n_o=1.525, $\Delta\epsilon$=+15.6). Photopolymerization of the monomers was initiated by means of a photoredox-catalysis mixture, consisting of a photo-oxidant dye (Methylene Blue) and co-initiator (p-toluenesulfonic acid) with concentrations of 0.12x10^{-3} M and 0.21 M, respectively. The prepolymer for Sample-1 consisted of a mixture of a monofunctional acrylic oligomer, CN135, with functionality slightly larger than one and a tetra-functional monomer, and SR295 (pentaerythritol tetraacrylate), with proper weight fractions to achieve an effective functionality of 3.5.[21] For Sample-2 we utilized a penta-functional monomer, SR399 (dipentaerythritol

pentaacrylate), and CN135, again with proper weight fractions to achieve an effective functionality of 3.5. All samples were prepared with 30 wt% E8 LC, 68 wt% polymerizable matrix and 2 wt% photoredox-catalysis mixture.

Additional samples were created using a sample set composed of Ebecryl 4866 and Ebecryl 8301 monomers (from UCB Radcure), N-Vinyl Pyrrolidinone and co-initiator N-Phenylglycine (Sigma Aldrich), and the liquid crystal BL038 (EM Industries), as well as the Methylene Blue dye. The recipe starts with the creation of the photo-initiator solution. The Methylene Blue, a blue powder, and the N-Phenylglycine, a yellow powder, are combined in a brown light-blocking vial. The N-Vinyl Pyrrolidinone, a clear liquid, is then added and acts as a solvent to dissolve the two solid components. The vial is then capped and placed in a sonicator while the rest of the recipe is prepared. The next step is to place the monomer in a separate brown vial, and then add the liquid crystal and the surfactant Octanoic Acid. The photoinitiator is finally added, and a micro stir bar is placed in the vial. The mixture is then sonicated at an elevated temperature (¡ 35^{o}C) for about one hour, until the syrup appears clear with no streaks, indicating complete mixing. The syrup is then ready for use, and can be stored in a refrigerator for up to one week and still be viable. It should be warmed to room temperature before use to ensure the correct viscosities for phase separation.

The H-PDLC samples were realized by introducing the H-PDLC material, *via* capillary action, between ITO glass plates pre-gapped with UV optical adhesive (NOA-65) and 10μm fiber spacers (Merck), at about 1 wt%. The average H-PDLC cell thickness was approx 10 μm, as verified by cross-section analysis with optical microscopy. The micro-structures of the cured gratings were examined by use of a JEOL JSM-35C scanning electron microscope. For SEM analysis the samples were freeze-fractured with liquid nitrogen and allowed to soak in methyl alcohol for several hours to remove LC. Samples

were then heated to evaporate residual methyl alcohol and AuPd sputter coated onto the sample stub.

The experimental setup utilized a 1.8 mW He-Ne laser beam which is expanded and recollimated to 1.0 cm diameter by a beam expander. The recollimated beam is split into two beams directed at the H-PDLC sample to form an interference pattern. The irradiance of the two interference beams incident at the holographic medium are adjusted to equal intensity with typical exposure irradiance of 0.478 mW/cm^2. Transmission spectrum data of the H-PDLC samples were measured with light from a 150W Hg Arc source which passed through a JY-Triax 550 monochromator and was coupled into a fiber optic light guide. The signal was detected using a TE cooled PbSe-photodiode whose output was connected to a lock-in amplifier (Stanford Research Systems SR850) detecting at the fundamental frequency. The spectral resolution of the setup was less than 1.0 nm in the region studied. For the determination of the switching characteristics of the gratings, an Advance Instruments oscillator was used to apply external electric fields to the H-PDLCs samples, ranging up to about 8 MV/m at 1.0 kHz. All experiments were conducted by use of computer-controlled data acquisition and analysis software.

3.3.2 Results

The average refractive index of the prepolymer mixture is expected to be[137]

$$n_{avg} = \sqrt{n_{LC}^2 \phi_{LC} + n_M^2 \phi_M} \approx 1.524 \tag{3.5}$$

where ϕ_{LC} and ϕ_M are the volume fractions of LC and monomer in the prepolymer mixture, $n_{LC} = [(2n_o^2 + n_e^2)/3]^{1/2} = 1.611$ and n_M is the refractive index of the monomer (≈ 1.485). The incident angle for Sample-1 (θ_i) was set to 27^o to allow for a spatial period of $\Lambda = 457$ nm. Giving us an expected reflection wavelength of $\approx$ 1390nm without polymer shrinkage. For Sample-2 (θ_i) was set to 30^o with a corresponding spatial period

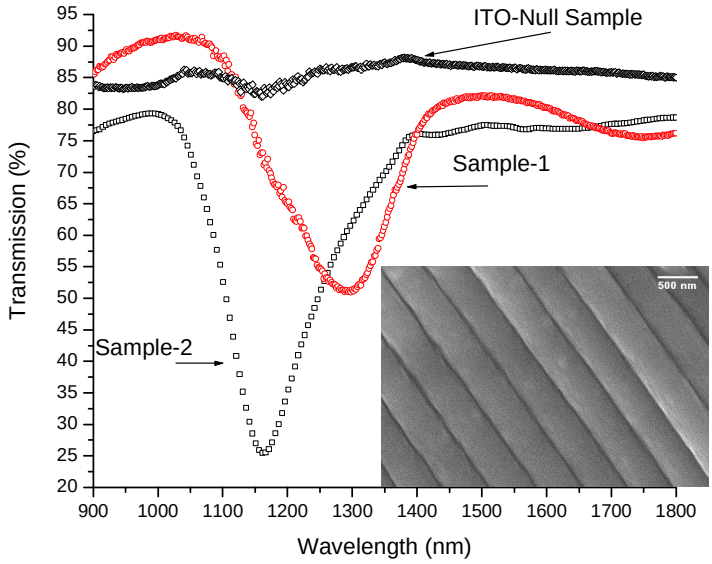

Figure 3.18. Transmission spectrum of Bragg reflection gratings for Sample-1 and Sample-2 along with ITO-null sample. Inset is SEM micrograph of Sample-2 with scale bar representing 0.5 μm.

of Λ= 415 nm with an expected reflection wavelength of $\approx$ 1260nm. Figure 3.18 shows our experimental results for both Sample-1 and Sample-2 along with a flood-lit ITO-null sample with SR295/CN135 polymer only. From the results we see significant shrinkage has occurred in both samples as expected, also a variation in diffraction efficiencies with Sample-2 having a diffraction efficiency of around 52% while Sample-1 achieving only 34%. We find the transmission spectrum has a notch with a minimum transmittance at the Bragg wavelength $\lambda_B = 2n_{avg}\Lambda_G$: 1295nm for Sample-1 and 1165nm for Sample-2. From the data, and utilizing equation (2) we can find the shrinkage factors (β) for the H-PDLC materials. For Sample-1 it is found to be 7% while for Sample-2 it is found to be 8%. These shrinkage factors are comparable with typical values which vary from 3% to 7% on average.[138] A possible explanation for the high shrinkage factors is that the long exposure time ($\sim$ 25 min) results in more complete cross-linking, and therefore a tighter matrix. Figure 3.18 inset shows SEM morphology for Sample-1 (scale bar is 0.5

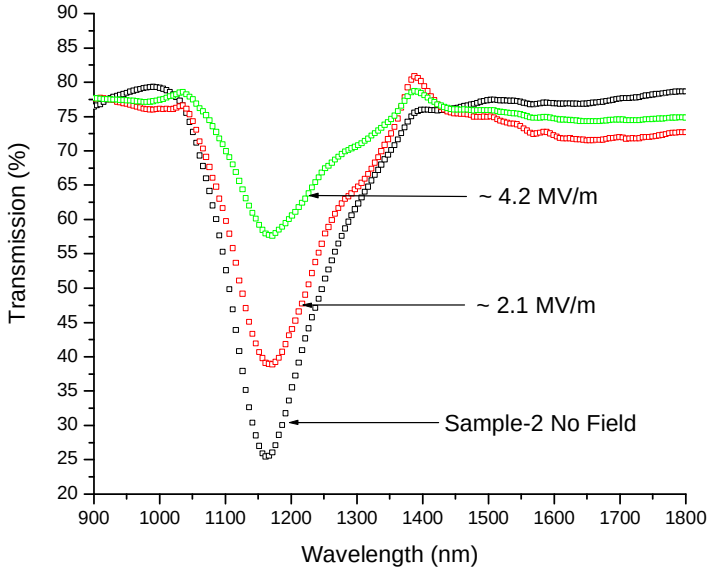

Figure 3.19. Optical spectra of Bragg reflection H-PDLC Sample-2 as a function of applied field.

μm). Here we see the lamellar polymer structure with voids where LC occupied; note that the polymer swells during preparation for SEM giving us an idea of the morphology but true spatial grating periods cannot be definitively determined.

For an ideal planar reflection grating, the reflection efficiency is given by [139]

$$\eta = \left[1 + \frac{(1 - \xi^2/\upsilon^2)}{\sinh^2\sqrt{\upsilon^2 - \xi^2}}\right]^{-1} \tag{3.6}$$

The transmittance T of the zero-order is then $T = 1 - \eta$. Here $\upsilon \propto n_1 L$, with n_1 being the first Fourier component of the refractive index modulation and L the thickness of the sample. The detuning parameter $\xi \propto (\lambda - \lambda_B)$ determines the fall-off of η as the wavelength (λ) departs from the Bragg condition (λ_B), and thus is related to the width of the transmission, notch full-width at half-maximum (FWHM). For our samples we have an approximate FWHM of 172nm for Sample-1 and 154nm for Sample-2. This FWHM is quite large compared to recent publications and at this time more studies are warranted with this monomer chemistry to determine the major contributor to this

effect. One possible cause is the large incident angle used during formation, in which waveguide effects in the sample occurs and high quality holograms become harder to write. The decrease in efficiency between samples, evident for increasing Λ_B, is due in part to the fact that the sample thickness is kept constant (10μm), and hence increasing Λ_B corresponds to reducing the number of Bragg planes.[140] An accompanying increase in the FWHM is also noted for the samples. From the data we determined a value for the index modulation (n_1) of the samples as 0.42 for Sample-1 and 0.37 for Sample-2. These values are higher than previous data reported.[141] It has been suggested that it is not suitable to use coupled-wave theory for calculating the index modulation for broad bandwidth reflection gratings, e.g., LippmannBragg broadband holographic gratings.[142] Figure 3.20 (a) shows our experimental results for a Bragg reflection grating using the liquid crystal BL038 and Ebecryl 8301 monomer. Figure 3.20 (b) shows the reflection data fitted utilizing coupled-wave theory and equation (2.61) with the fitting parameters as; $n_o = 1.54$, $L = 10\mu$m and $n_1 = 0.0245$ as the index modulation.

Figure 3.19 shows the electro-optic response of Sample-2. With application of an increasing amplitude 1.0kHz square wave signal, we note a reduction in the reflection notch as a function of applied field. The switching voltage (less than 10% reflectance) is determined to be approximately 6-7 MV/m. Sample-1 showed similar switching fields on the order of 5-6 MV/m. This high voltage can be partially attributed to nano-scale confinement of the LC along with other attributing factors such as LC anchoring strength and alignment, the LC droplet ordering parameter and the dielectric integrity of the sample. The switching voltage is found to be roughly inversely proportional to the size of the LC confinement($\sim$ 200nm for our samples). With applied fields greater than 8 MV/m, the H-PDLC grating is effectively switched off. Application of a 7 MV/m field shows that the transmission of the H-PDLC over the spectrum from 900nm-1800nm is

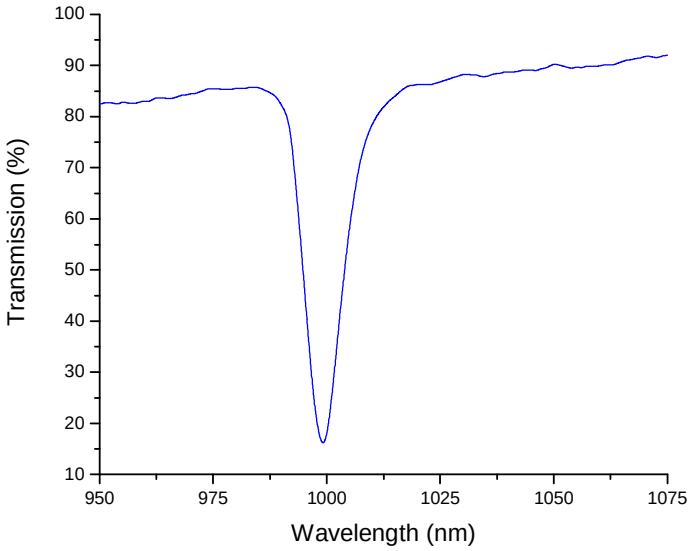

(a)

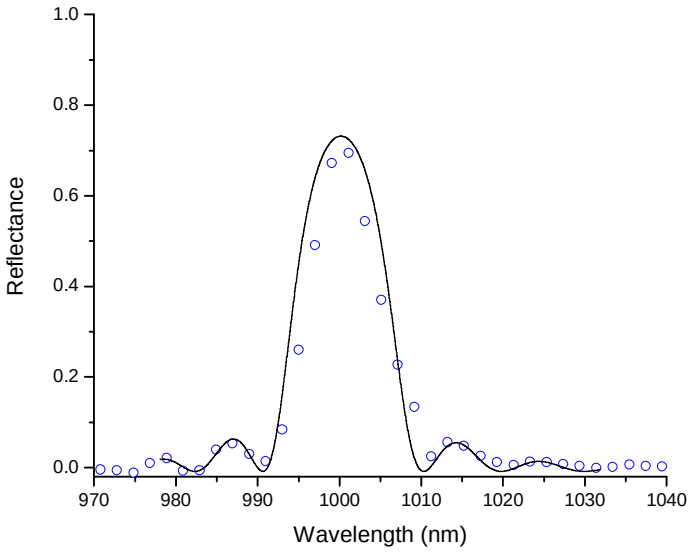

(b)

Figure 3.20. (a) Transmission spectrum of Bragg reflection grating utilizing liquid crystal BL038 and Ebecryl 8301 monomers. (b) Fitted data to reflection spectrum using coupled-wave theory.

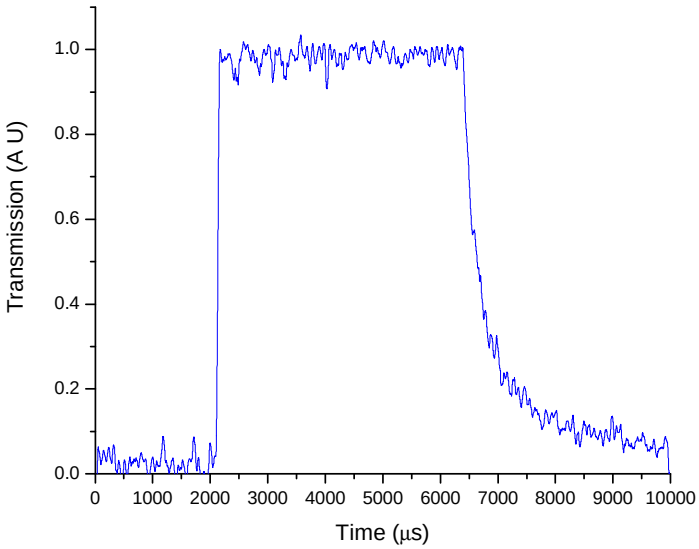

Figure 3.21. Temporal response of H-PDLC Sample-2 upon application of 5.0 MV/m DC pulse.

switched to about 76% transmission. Correcting for losses at the front and back surfaces increases the optical throughput of the sample to around 81%.

Temporal switching response data for Sample-2 is shown in Figure 3.21. Here we selected the wavelength of 1165 nm from a Hg lamp and monitored the transmission via lock-in detection of a PbSe TEC cooled detector. The collected data was scaled to a peak transmission of unity and smoothed using a Savizky-Golay filter. The applied pulse is 5.0 MV/m with a duration of 4ms. The reflection efficiency decreases rapidly with the applied field and allows transmission of 1165 nm wavelength. The response of the sample is found to have a rise time of 64.3 μs and a full relaxation time of 6.3ms. For Sample-1 we determined switching times of 58.6 μs and 7.2ms for rise time and relaxation time respectively.

3.4 Reverse-Mode Transmission Grating

First and foremost we would like to thank L. V. Natarajan and T. J. Bunning for bring this exiting problem to our attention and for their useful discussions. Reverse-mode transmission gratings are holographically recorded in a polymer dispersed liquid crystal materials set utilizing the 540nm lasing wavelength. The samples are synthesized utilizing mixtures of a reactive mesogen, RM257, nematic liquid crystals E44 and E3100-100, acrylate monomers and a photo-oxidant dye. We investigate the formation parameters, electro-optical and frequency characteristics of these gratings. It is found that for an applied field strength of around 14 V/μm a relative increase in the diffraction efficiency of almost 1200% is obtained with switching times of 12ms. In this section we discuss our initial experimental results on the reverse-mode operation of Raman-Nath (thin grating) diffraction gratings formed with a selective reactive mesogen material set.

3.4.1 Experimental Details

For the synthesis of the reverse-mode H-PDLC we utilized a mixture of nematic liquid crystals E3100-100 and E44 (Merck), a reactive mesogenic monomer, an acrylate monomer (trimethylolpropane triacrylate), and photoinitiator/co-initiators. The reactive mesogen used in this study is a diacrylate, trade name RM257 (EM Industries), which possesses a negative dielectric anisotropy ($\Delta\epsilon$=- 1.8) with a stable nematic liquid crystal phase in the temperature range 70-126^{o}C. Reactive mesogens are liquid crystalline materials with polymerizable end groups. Polymerization of reactive mesogens leads to densely crosslinked networks in which the liquid crystalline order, or director for nematics, is permanently fixed.[143] In our case we employ these reactive mesogens, in the liquid crystal phase, for in-situ photo-initiated polymerization of the end groups to obtain the optimum mesophase morphology and alignment for reverse-mode operational H-PDLCs, more on this later. The structure and chemical makeup of RM257

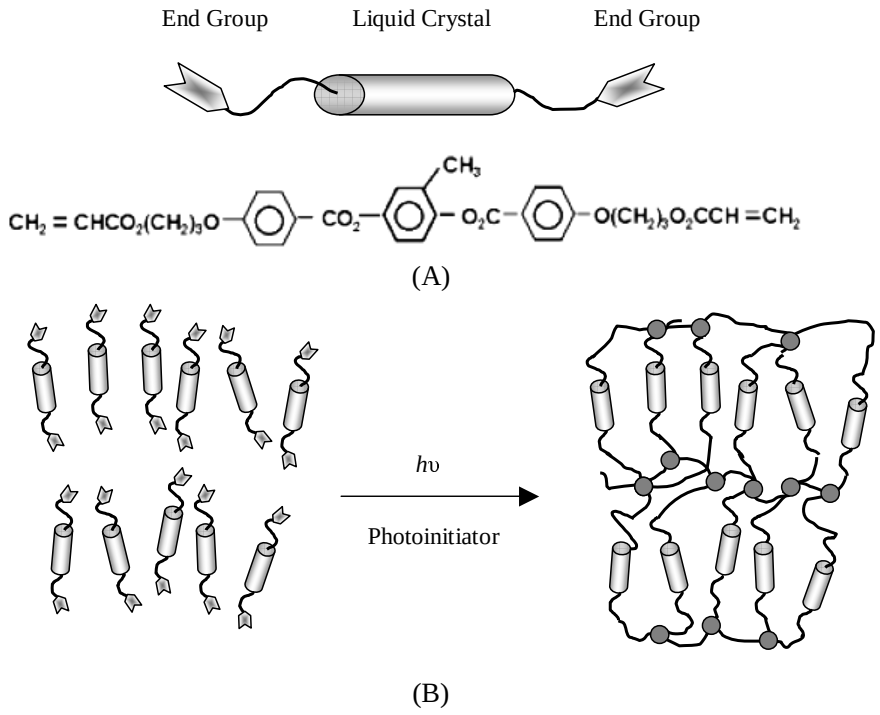

Figure 3.22. (A) Chemical structure of the reactive mesogen RM257. (B)Photopolymerization process of reactive mesogens.

is seen in Figure 3.22 as well as a figure depicting typical photopolymerization of reactive mesogens. Photopolymerization of the monomers is initiated by means of a photoredox-catalysis mixture, consisting of the photo-oxidant dye rose bengal wt 0.5% and co-initiators *N*-phenylglycine (NPG) and the commercially available CD1012, at 1.0 and 1.6 wt% respectively. The influence of the photoinitiator and co-initiator on the phase transition temperatures of the pure reactive mesogen are known to decrease these values with an increasing photoinitiator content. The prepolymer for the samples consisted of a mixture of the diacrylate RM257 at 20.5 wt% and the triacrylic monomer at 2.7 wt%. All samples were prepared with 55.7 wt% E3100-100, 15 wt% E44 and 0.5 wt% 5μm spacers (Merck). The addition of NVP as a homogenizer at 2.5 wt % was also employed in the mixture.

The liquid crystal E44 which has a large birefringence with a nematic mesophase at room temperature (Δn=0.2627) and E3100-100 (Δn=0.1707), also with a nematic mesophase at room temperature, were used as a dielectric dopant to increase the dielectric constant anisotropy ($\Delta\epsilon$) of the H-PDLC sample mixture. Doping of the samples to acquire a sufficiently positive $\Delta\epsilon$ allowed for the reactive mesogen to be aligned homeotropically, or parallel, with the applied electric field. The calculation of the resultant dielectric constant anisotropy of the LC/Mesogenic mixture is described by [144]

$$\bar{\Delta\epsilon} = m_1\Delta\epsilon_1 + m_2\Delta\epsilon_2 + m_3\Delta\epsilon_3 \tag{3.7}$$

where m_1, m_2 and m_3 are the molar fraction components of E44, E3100-100 and RM257 respectively along with their corresponding dielectric constant anisotropies $\Delta\epsilon_1$, $\Delta\epsilon_2$ and $\Delta\epsilon_3$. For our mixtures which have a sample mass of 1.0 g, we calculate, a dielectric constant anisotropy of $\bar{\Delta\epsilon} = +\ 0.1201$.

The sample mixture is heated to 95^{o}C and sonicated for 20 minutes at an elevated temperature above 65^{o}C to allow for mixing. Polyvinylalcohol (PVA) is spin coated onto indium-tin oxide (ITO) coated glass slides and baked at 110^{o}C for 1 hour. The PVA is then rubbed with velvet to allow for homogeneous alignment of the reactive mesogen at the PVA/mesogenic interface. The rubbing direction of the PVA was such that it is perpendicular to the impending H-PDLC grating vector. Rubbing changes the topography of an alignment layer in the PVA and induces an anisotropic orientation of polymer molecules along the rubbing direction. The liquid crystals in the nematic phase are then preferentially aligned along this direction which facilitates directional control of the reactive mesogens during photopolymerization. The sample mixture is heated after mixing and allowed to equilibrate for several minutes at 95^{o}C. At this temperature, the nematic liquid crystal phase is stable for RM257 and allows for easy alignment during the phase seperation process. The sample mixture is then sandwiched between two coated

glass slides and compressed together using binder clips for uniform spacing of the H-PDLC film. The average H-PDLC cell thickness was approx 5 μm, as verified by cross-section analysis with optical microscopy. It should be noted that the final photopolymerization, holographic exposure, must be carried out when the RM257 is in its nematic phase for proper alignment procedures to be successful. This can be achieved either with an experimental setup that allows for continual heating of the filled ITO sample cell during photopolymerization, or a rapid injection technique that allows for heated substrates to maintain the sample mixture above 70^{o}C long enough for photopolymerization to occur ($<$ 30 seconds).

The experimental setup utilized a 25 mW green diode laser (540nm) which was expanded and recollimated to 2.0 cm diameter by a beam expander. The recollimated beam was split into two beams with equal optical path lengths and directed at the H-PDLC sample to form an interference pattern. Both writing beams were incident on the same side of the H-PDLC sample, making the diffractive grating a transmission type grating. The irradiance of the two interference beams incident on the holographic medium were linearly polarized (p-type) and adjusted, using a linear stepped optical density filter, to equal intensity with typical exposure irradiance (sum of both beams) ranging from 0.19 mW/cm^2 to 2.0 mW/cm^2. The grating spatial period (Λ) written at 540nm, with our experimental geometry, was calculated to be 3.06 μm (Raman-Nath grating), this was verified under optical microscope. The probe beam was a 1.2 mW HeNe laser incident at 18.5^o from the normal. The incident light was linearly polarized with polarization selected to be parallel to the grating vector **K** (p-type polarization). This allowed for minimal dichroism effects of the rubbed PVA substrates to effect experimental results. The experimental geometry is seen in Figure 3.23. The probe beam lasing at 632.8nm was not absorbed by the samples and did not interfere with the writing process. For the determination of the electro-optical characteristics of the gratings, an Advance

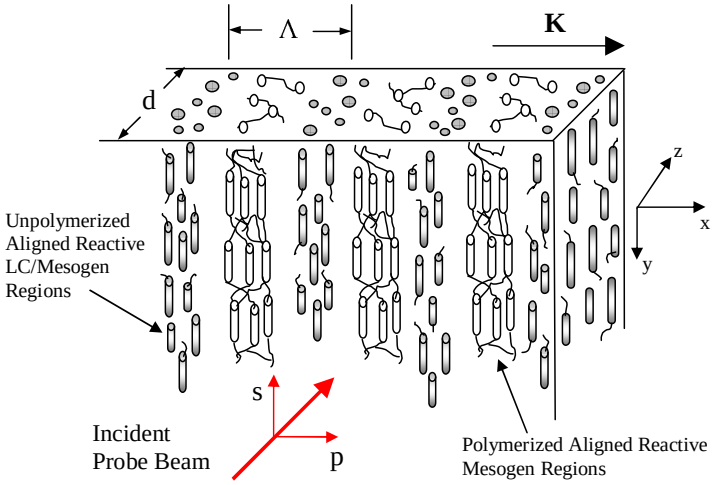

Figure 3.23. Schematic drawing of the H-PDLC experimental geometry for a typical transmission grating experiment with grating thickness d and grating spatial periodicity Λ shown, along with the grating vector $\mathbf{K}$ and probe beam polarization components.

Instruments oscillator was used to apply external electric fields ranging up to 20 V/μm at various frequencies. All experiments were conducted by use of computer-controlled data acquisition and analysis software and occurred under ambient conditions. The diffraction efficiency (η), was obtained by measuring the intensity of the incident probe beam and the intensity of the first-order diffraction beam using Si-photodiodes and associated electronic modules. Unless otherwise specified, diffraction results refer to first-order diffraction.

3.4.2 Results

Several reverse-mode samples were formed with subsequent data taken in which we observed a dependence on the electro-optical properties to varying exposure times as well as writing intensities. As one increases the exposure time, for a fixed writing intensity, sufficient polymerization of the reactive mesogens occurs and begins to have adverse effects that are detrimental to the operation of a reverse-mode diffraction grating. In the reactive mesogenic system, the mixture exposed to constructive interference (bright

regions) of the writing beam will polymerize and in the destructive regions of the interference pattern (dark regions) will remain LC-monomeric (mixture of LC and RM257). As polymer conversion occurs in the initial stages of the writing process the LC-monomeric regions are relatively free to orient under the influence of an externally applied field. As the polymerization continues (longer exposure times) the LC-monomeric regions become more rigid within the grating formation and appear to be influenced by anchoring forces from the polymerized regions, or possible lateral polymerization of the reactive mesogen into the LC-monomeric regions, each of which decreases the overall response to an applied electric field.

With the application of an electric field the LC-monomeric regions will align with the field due to its positive dielectric anisotropy. This results in a larger Δn and thus an increase in diffraction efficiency. We found that in order to minimize the LC-monomeric regions from being polymerized, but allow sufficient polymerization in the polymeric regions, an exposure time between 2-6 seconds was optimal. An exposure of less than 2 seconds gave very obscure diffraction orders that had no change on application of applied fields. With this short of an exposure, and at low intensities (< 0.25 mW/cm^2), little if any polymerized regions are formed and grating structure was all but absent under an optical microscope. For exposures longer than 7 seconds diffraction efficiencies grew, but applied field effects became less observable. At exposure times beyond 40 seconds applied field changes in the diffraction efficiency were less than 0.5%. Results of several samples with varying cure times and the achieved diffraction efficiency modulations are seen in Figure 3.24 in which we show the percent change in diffraction efficiency as a function of exposure time for a writing intensity of 0.31 mW/cm^2. These increases in diffraction efficiency are quite remarkable for sample that are allowed to cure between 2-6 seconds. The efficiencies are relative percent changes to an initial diffraction order. That is to say that all samples produced a first order diffraction even in the off state with

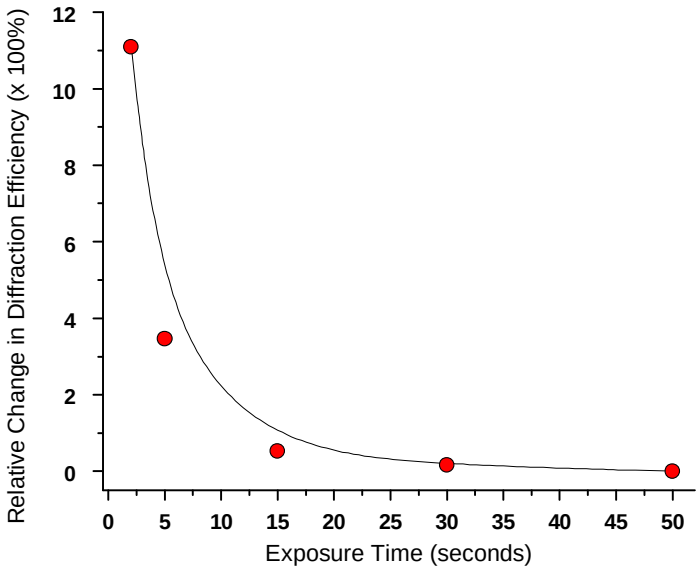

Figure 3.24. Effect of writing exposure times on the ability to modulate the diffraction efficiency in reverse-mode H-PDLC samples. Data plotted as relative change in diffraction efficiency (times 100%).

the application of the applied field increasing the efficiency. These diffraction orders in the off state are mainly due to small mesogenic anisotropies along the grating vector and poor alignment along the rubbed substrate. Seen in Figure 3.25 are the initial diffraction efficiencies achieved as a function of exposure time for the first order diffracted beam. Also seen is the modulation over which each diffracted order was able to be increased to.

It has been reported elsewhere that the shrinkage properties of particular diacrylate reactive mesogens during polymerization is low, 4-7% , compared to 11-15% for typical isotropic acrylate used in standard H-PDLCs.[145] This effect has been attributed to tight packing of the mesogenic monomer, which in turn produces a much less pronounced density grating, minimizing the off state diffraction over that of normal mode H-PDLCs. One key property of reactive mesogens which allows for reverse-mode technology is the polymerization shrinkage. This shrinkage is found to be anisotropic, with the principal

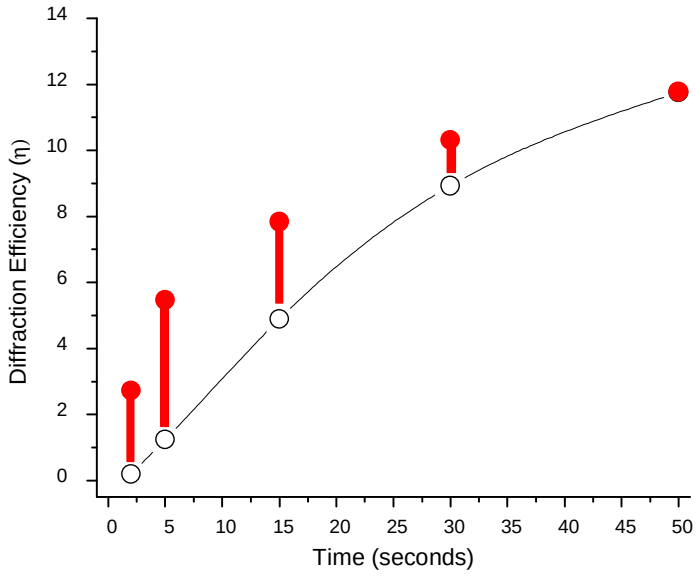

Figure 3.25. First order diffraction efficiency and modulation as a function of exposure time for a writing intensity of 0.31 mW/cm^2.

component occurring along the direction of alignment. In our geometry, this corresponds to the direction parallel to the grating lines. This in turn further reduces the contribution of mesogenic monomer diffusion to Δn in the polymerization process, given that shrinkage occurs primarily within each fringe and not across fringe boundaries for short exposure times.

The full temporal evolution of the grating formation follows qualitatively the same behavior as standard H-PDLC transmission mode diffractive gratings. In general, the complete writing process for a fully cured grating is accomplished with short exposure times ($<$ 50s) at varying writing intensities. Initially there is a short induction period ($\leq$ 2 s) during which all inhibitors, e.g. oxygen, have reacted. Next there is a period ($\sim$ 14 s) of polymerization of the reactive mesogens and acrylate monomers giving an associated rise in diffraction efficiency with several orders of diffraction developing as the process continues. Finally a plateau region occurs within which the polymerization is mostly completed and the rose bengal photoinitiator dye molecules are considered bleached.

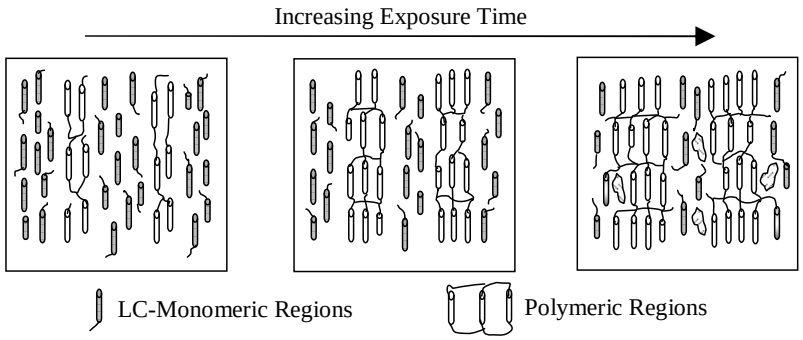

Figure 3.26. Schematic drawing of the temporal evolution of the morphology of a reverse-mode H-PDLC.

The process itself is quite complex, the photoinitiator that is dissolved in the reactive mesogen mixture is fragmented into a free radical upon photon absorption, this process initiates the chain polymerization. In the LC-monomeric state the long-range ordering of the mesogens proceeds rapidly due to the alignment layer, unlike the orientation in the polymeric state where, in addition to the rotational displacements of the mesogenic moieties, segments of the polymeric chain also have to be displaced, see Figure 3.26. Here we see that as time progress the free reactive mesogens are eventually added to the crosslinked network of polymerized mesogens. To become polymerized the moiety must move into place in the polymer network, this usually requires displacement of the moiety and possible rotation. One thing to note in our sample mixture is that the addition of E44 and E3100-100 liquid crystal utilized as a dielectric dopant adds a phase separation process to the overall morphology development. In addition to polymerization of the reactive mesogens and added acrylate monomers (trimethylolpropane triacrylate) there is also a phase separation process that occurs after polymerization of the reactive mesogens begins to proceed out from the constructive interference regions. As polymerization continues this leads to a change in the chemical potential of the system, reducing the miscibility gap between the LC and the monomer, resulting in diffusion processes and

eventual phase separation. The liquid crystal begins to phase separate out of the mixture and small liquid crystal pools begin to form in the morphology of the system. If the mixture is allowed to be exposed for the full time (> 50 s) the achieved morphology of the system resembles that of a typical H-PDLC with structured regions of mesogenic polymer and phase separate liquid crystal, but there is not an operational mode of a typical H-PDLC. That is to say, one cannot apply an electric field and decrease the diffraction efficiency, such as with typical H-PDLC technology. This final stage of the grating formation requires much more understanding at this junction and not the main thrust of this report. More research is ongoing into the mechanisms and processes that occur during the later stages of polymerization in reverse-mode H-PDLC technology. For reverse-mode operation, only when polymerized to the optimal degree were the mesogenic monomers able to be aligned by the applied electric field while the polymeric regions remain unaffected. As alignment of the mesogens proceeds with time, due to the rubbed PVA layer, a majority of the mesogens are aligned with the extraordinary optical axis normal to the substrate. As polymerization continues in the bright fringes these mesogens are fixed in place while the LC-monomeric regions, still aligned via PVA alignment layer but not fully crosslinked into the polymer network, are free to move under the influence of the applied electric field. RM257 is a long molecule that has vinyl groups at both end. This reactive mesogen forms a crosslinked network that is extremely rigid, and the long range order is preserved after photopolymerization is complete. The density of the crosslinked polymerization is much higher than that of non-crosslinked liquid crystalline elastomers formed by a single end-group reactive mesogen. Unlike the liquid crystalline elastomer, which changes orientation easily under external forces, the network formed via RM257 diacrylate is densely crosslinked and is expected to be more rigid and irreversible in orientation. This allows for the grating structure to maintain its integrity during electric field modulation of the diffraction grating.

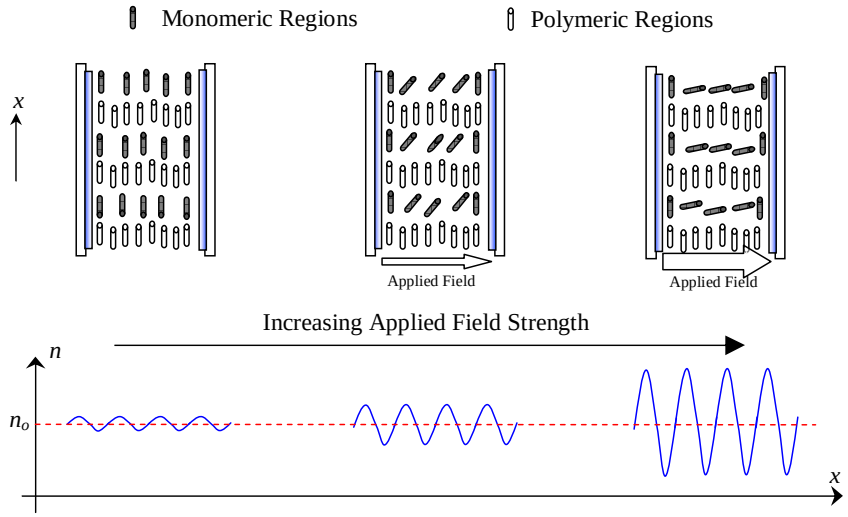

Figure 3.27. Schematic of reverse-mode operation of reactive mesogen materials set. The rubbing direction of the substrate is in the x direction. Also shown is the spatial index modulation profile (Δn).

The ability to modulate the diffraction grating was tested at different exposure times to further explore and understand the grating formation process. Figure 3.27 shows a cartoon of the switching of a reverse-mode H-PDLC. Shown is the LC-monomeric regions ability to orient themselves along the direction of the applied field. Also seen is how the spatial index modulation ($n(x)$) is increased as the applied field increases giving the device reverse-mode operation. Actual anchoring forces due to the alignment layer are not known but are assumed to be such that the mesogens within the LC-monomeric regions are allowed to initially overcome them with field strengths of 6-7 V/μm. As cure times increase; not only are there interfacial anchoring forces to be overcome, but other aspects such as polymerization occuring within the LC-monomeric regions.

Figure 3.28 shows the electro-optical switching response of a reverse-mode H-PDLC diffraction grating. Here a sample was exposed for 2 seconds at a writing intensity of 0.31 mW/cm^2, after which the sample was toggled on and off with an applied field to verify increasing index modulation. The applied field to the sample had an amplitude of 14

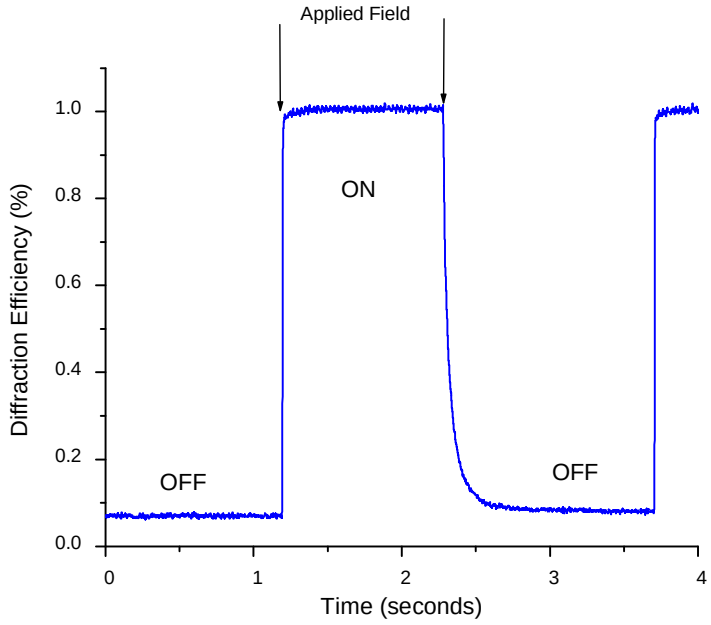

Figure 3.28. Switching response of first-order diffraction efficiency for a reverse-mode H-PDLC sample with exposure time of 2 seconds. The applied field is 14V/μm at 1.0 kHz frequency.

V/μm at 1.0 kHz, which is in range of typical values used in reverse-mode devices.[146] The sample was toggled consecutively for 60 seconds (see Figure 3.29) with an on/off duty cycle of 40% and period of 2.5 seconds. From the data it is seen that the sample showed stable reversibility with a percent change of approximately 1200% in the first-order diffraction efficiency with response times of 15ms and 190ms for rise-time and fall-time, respectively. Additional samples exposed for 5-50 seconds at the same writing intensity (0.31 mW/cm^2) began to show multiple orders of diffraction. Again fields of 14 V/μm at 1.0 kHz were applied to the samples and the first-order diffraction efficiency was monitored. The experimental results of several samples with varying exposure times for a fixed writing intensity are shown in Table 3.4. The table gives the rise and fall times of the switching response as well as the percent change in the diffraction efficiency. He we note a decreasing trend in the ability to modulate the diffraction efficiency as the

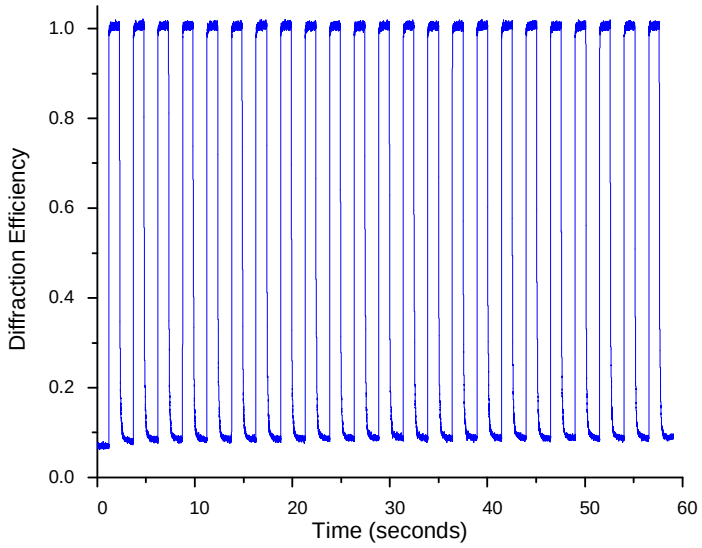

Figure 3.29. Switching response for a reverse-mode H-PDLC sample with exposure time of 2 seconds. The applied field is 14V/μm at 1.0 kHz frequency.

Table 3.4. Results of varying exposure time on the electro-optical properties

	Rise Time	Fall Time	$\Delta\eta$
5-Second Exposure	11.8 ms	17.7 ms	346%
15-Second Exposure	39.8 ms	79.2 ms	53%
30-Second Exposure	26.4 ms	110 ms	16%
50-Second Exposure	13.3 ms	65.4 ms	0.1%

exposure time is increased. Also there is an overall increase in the rise and fall times in the switching properties of the samples. This overall trend itself has many possible variables each of which could contribute to this increase, such as anchoring energies, interfacial energies due to rubbed substrates, phase separation of the LC itself. One notes the increase and then decrease in the rise times as we go from 5 to 15 seconds and then from 15 to 50 seconds. We believe it is within this time period that the LC begins to phase separate out and gelation of the reactive monomers occurs. As this occurs the larger pools of isolated LC within the morphology would allow for a decrease in the

switching times while at the same time decreases the overall reverse-mode operation of the H-PDLC. Because of the softness of the cure for samples between 2 and 15 seconds, sample preparation for SEM analysis is complicated. Additional switching cycles were preformed on the samples with modulation persisting for over an hour with a very slight decrease in the overall switching efficiency of the grating.

Another electro-optical parameter studied was the frequency at which the driving field was oscillating, at 1.0 kHz we appeared to obtain an optimal response. To verify this was the case we fabricated two samples using a 15 second exposure and allowed for the driving field to vary with frequency only. We also utilized another reactive mesogen at this time during our study, RM82 (EM Industries), which has a very similar reactive moiety with two end groups. Both samples were fabricated identically with only the reactive mesogen being replaced in the recipe. The results of the study are seen in Figure 3.30. Here we see the effects of varying the driving frequency of the applied field, which was varied from 10 Hz to 10 kHz at 14 V/μm. The data was fit utilizing a cubic-spline interpolation with the magnitude of the change in diffraction efficiency ($\Delta\eta$) having the greatest value at around 1.0 kHz for both reactive mesogens.

3.5 Summary

In this chapter we have shown our results from various experiments involving patterning techniques with polymer dispersed liquid crystals. We have investigated the effects of monomer functionality on the formation and performance of H-PDLC gratings written by using the 632.8 nm wavelength of He-Ne laser. We have also studied the effects of externally applied electric fields on the diffraction efficiency and their correlation to functionality for different H-PDLCs mixtures. We have also investigated the realization of switchable H-PDLC Raman-Nath and Bragg transmission and reflection gratings written with the 632.8 nm wavelength of He-Ne laser. We have demonstrated the fabrication

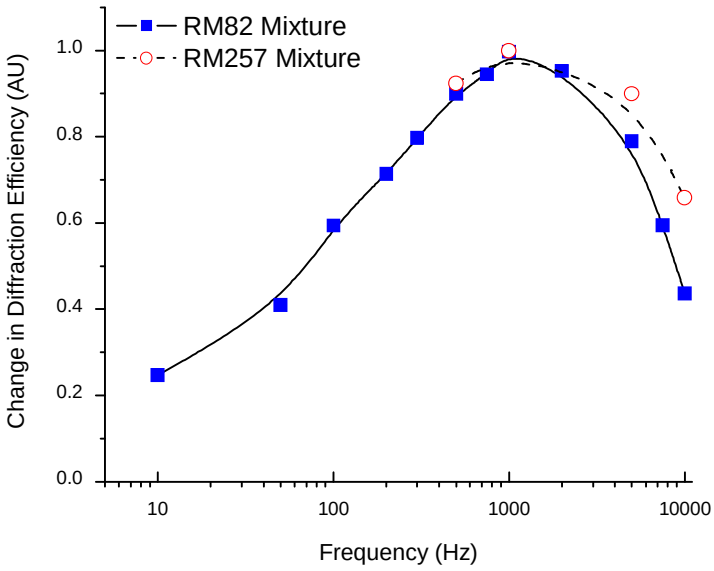

Figure 3.30. Effect of driving frequency on the modulation of the diffraction efficiency.

and operation of reverse-mode H-PDLC diffraction gratings which allows for an increase in the diffraction efficiency. For the reactive mesogens in our experiments, only when polymerization has occurred at the optimal timing can the maximum modulation ration be achieved.

CHAPTER 4

CONCLUSIONS

We have investigated the effects of monomer functionality on the formation and performance of H-PDLC transmission gratings written by using the 632.8 nm wavelength of He-Ne laser and utilizing a materials set not yet developed. We have observed the formation of well-defined periodic grating structures with varying diffraction efficiencies which show strong dependence upon monomer functionality. We have also studied the effects of externally applied electric fields on the diffraction efficiency and their correlation to monomer functionality for different H-PDLCs mixtures. We have also investigated the realization of switchable H-PDLC gratings written with the 632.8 nm wavelength of He-Ne laser. Further we have investigated the realization of switchable H-PDLC Bragg reflection gratings written with the 632.8 nm wavelength of He-Ne laser. We again observed the formation of well-defined periodic grating structures, which are characterized with grating periods, $\Lambda_B \sim$ 420-490 nm with maximum diffraction efficiencies of $\eta \sim$ 65% at varying IR wavelengths. We have also studied the effects of the externally applied square-wave electric fields on the diffraction efficiency and found switching fields on the order of 7-8 MV/m and switching rise times 64μs with relaxation times of 6ms. For the "revers-mode" H-PDLC operation we have developed and investigated diffraction gratings which allows for an increase in the diffraction efficiency in some cases up to 730%. We have studied the effects of writing beam intensity on the growth and performance as well as grating formation times. Reverse-mode H-PDLCs have been fabricated with switching fields of 12ms rise time and 18ms decay times. We have also studied the effects

of driving frequency of the externally applied electric fields on the diffraction efficiency and found an optimal response at 1.1 kHz.

BIBLIOGRAPHY

[1] F. Reinitzer, Monatsch. Chem. **9**, 421 (1888).

[2] O. Lehmann, Z. Phys. Chem. **4**, 462 (1889).

[3] E. B. Priestley, P. J. Wojtowiez, and P. Sheng, *Introduction to Liquid Crystals* (Plenum Press, New York, 1975).

[4] B. Bahadur, *Liquid Crystals, Applications and Uses. Vol. 1* (World Scientific, 1990).

[5] D. Demus, J. Goodby, G. W. Gray, H. W. Spiess, and V. Vill, *Hanbook of Liquid Crystals, Vol. 2A* (John Wiley and Sons (VCH), New York, 1998a).

[6] D. Demus, J. Goodby, G. W. Gray, H. W. Spiess, and V. Vill, *Hanbook of Liquid Crystals, Vol. 2B* (John Wiley and Sons (VCH), New York, 1998b).

[7] L. M. Blinov, *Electro-Optical and Magneto-Optical Properties of Liquid Crystals* (John Wiley and Sons (Interscience), New York, 1983).

[8] M. R. Kuzma and A. Saupe, "Structure and phase transitions of amphiphilic lyotropic liquid crystals," in *Handbook of Liquid Crystal Research*, P. J. Collings, ed. (Oxford University Press, New York, 1997).

[9] P. Mariani, F. Rustichelli, and G. Torquati, in *Physics of Liquid Crystalline Materials*, I. C. Khoo and F. Simoni, eds. (Gordon and Breach, Philadelphia, 1991).

[10] A. Ciferri, W. R. Krigbaum, and R. B. Meyer, *Polymer Liquid Crystals* (Academic Press, New York, 1982).

[11] H. G. Galabova, Y. Jiang, L. Li, S. Vartak, and S. M. Faris, SID International Syposium Digest of Tecnical Papers **30**, 1058 (1999).

[12] J. Chen, K. C. Chang, J. DelPico, H. Seiberle, and M. Schadt, SID International Syposium Digest of Tecnical Papers **30**, 98 (1999).

[13] H. Finkelmann, W. Gleim, K. Hammerschmidt, and J. Schatzle, Makromol. Chem.-M Symp **26**, 67 (1989).

[14] F. J. Davis, A. Gilbert, J. Mann, and G. R. Mitchell, J. Polym. Sci. Pol. Chem. **28**, 1455 (1990).

[15] N. S. Eichenlaub and G. P. Crawford, Mol. Cryst. Liq. Cryst. **329**, 1077 (1999).

[16] E. Lueder, *Liquid Crystal Displays: Addressing Schemes and Electro-Optical Effects* (John Wiley and Sons (SID), Chichester, 2001).

[17] I. W. Hamley, *Introduction to Soft Matter: Polymers, Colloids, Amphiphiles and Liquid Crystals* (John Wiley and Sons, New York, 2000).

[18] P. G. D. Gennes and J. Prost, *The Physics of Liquid Crystals 2nd Ed.* (Oxford University Press, United Kingdom, 1995).

[19] G. Vertogen and W. H. de Jeu, *Thermotropic Liquid Crystals, Fundamentals* (Springer-Verlag, Berlin, 1988).

[20] W. H. de Jeu and P. Bordewijk, J. Chem. Phys. **68**, 109 (1978).

[21] M. Deutsch, Phys. Rev. A **44**, 8264 (1991).

[22] A. Saupe and G. Englert, Phys. Rev. Lett. **11**, 462 (1963).

[23] W. Maier and G. Meier, Z. Natursforsch. **16a**, 262 (1961).

[24] E. F. Carr, J. Chem. Phys. **38**, 1536 (1963).

[25] S. Chandrasekhar, *Liquid Crystals* (Cambridge University Press, Cambridge, 1994).

[26] W. H. de Jeu, *Physical Properties of Liquid Crystalline Materials* (Gordon and Breach, New York, 1980).

[27] C. W. Oseen, Trans. Faraday Soc. **29**, 883 (1933).

[28] F. C. Frank, Disc. Faraday Soc. **25**, 19 (1958).

[29] A. Rapini and M. J. Papoular, J. Phys. Colloq. C4 **30**, 54 (1969).

[30] M. G. Tomlin, J. Opt. Tech. **64**, 452 (1997).

[31] M. C. Mauguin, Bull. SOc. Fr. Miner. **34**, 71 (1911).

[32] L. A. Goodman, D. Meyerhofer, and S. Digiovanni, IEEE Proc. **ED-23**, 1176 (1976).

[33] U. Wolff, W. Greubel, and H. Krüger, Mol. Cryst. Liq. Cryst. **23**, 187 (1973).

[34] J. Cheng and G. D. Boyd, Appl. Phys. Lett. **35**, 44 (1979).

[35] W. M. Gibbons, P. J. Shannon, S. Sun, and B. J. Swetlin, Nature **351**, 49 (1991).

[36] M. Schadt, K. Schmitt, V. Kozinkov, and V. G. Chigrinov, Jpn. J. Appl. Phys. **31**, 2155 (1992).

[37] X. T. Li, A. Natansohn, and P. Rochon, Appl. Phys. Lett. **74**, 3791 (1999).

[38] T. Uchida, C. Shishido, and M. Wada, Electron. Commun. Jpn. **58C**, 132 (1975).

[39] B. Y. Zel'dovich, N. F. Pilipetski, A. V. Sukhov, and N. V. Tabiryan, JETP Lett. **31**, 263 (1980).

[40] N. V. Tabiryan, A. V. Sukhov, and B. Y. Zel'dovich, Mol. Cryst. Liq. Cryst. **163**, 1 (1986).

[41] R. B. Meyer, Phys. Rev. Lett. **22**, 918 (1969).

[42] W. Helfrich, J. Chem. Phys. **51**, 4092 (1969).

[43] R. Williams, J. Chem. Phys. **39**, 384 (1963).

[44] P. A. Penz, Phys. Rev. Lett. **24**, 1405 (1970).

[45] P. J. Drzaic, *Liquid Crystal Dispersions* (World Scientific, Singapore, 1995).

[46] S. L. Rosen, *Fundemental Principles of Polymeric Materials* (John Wiley and Sons, New York, 1993).

[47] G. Odian, *Principles of Polymerization, 4th Ed.* (John Wiley and Sons, New York, 2004).

[48] E. Dubois-Violette and O. Paradi, J. Phys. Colloq. **30**, 57 (1969).

[49] P. Drzaic, J. Appl. Phys. **60**, 2142 (1986).

[50] J. W. Doane, N. Vaz, B. G. Wu, and S. Zumer, Appl. Phys. Lett. **48**, 269 (1986).

[51] N. Vaz, G. W. Smith, and G. Montgomery, Mol. Cryst. Liq. Cryst. **146**, 1 (1987).

[52] R. Hikmet, J. Appl. Phys. **68**, 4406 (1990).

[53] D. Uang, L. Chien, and J. Doane, Appl. Phys. Lett. **60**, 3102 (1992).

[54] C. Chang, L. Chien, and R. Meyer, Phys. Rev. E **56**, 595 (1997).

[55] M. Escuti, C. Bowley, G. Crawford, and S. Zumer, Appl. Phys. Lett. **75**, 3264 (1999).

[56] R. Ma and D. Yang, Phys. Rev. E **61**, 1567 (2000).

[57] J. Mangerum, A. Lackner, E. Ramos, G. Smith, N. Vaz, J. Kohler, and C. Allison, Polymer Dispersed Liquid Crystal Film Devices and Method of Forming the Smae pp. US Patent 4,938,568 (1990).

[58] J. Mangerum, A. Lackner, E. Ramos, G. Smith, N. Vaz, J. Kohler, and C. Allison, Polymer Dispersed Liquid Crystal Film Devices pp. US Patent 5,096,282 (1992).

[59] D. Whitney and R. Ingwall, Proc. SPIE **1213**, 18 (1990).

[60] R. I. T. Adams, Proc. SPIE **1555**, 279 (1991).

[61] R. Sutherland, L. Natarajan, V. Tondiglian, and T. Bunning, Chem. Mater **5**, 1533 (1993).

[62] R. Sutherland, L. Natarajan, V. Tondiglian, T. Bunning, and W. Adams, Appl. Phys. Lett. **64**, 1074 (1994).

[63] K. Tanaks, K. Kato, S. Tsuru, and S. Sakai, SID international Symposium Digest of Tehcnical Papers **24**, 109 (1996).

[64] D. Gabor, Nature **161**, 777 (1948).

[65] G. Saxby, *Practical Holography* (Prentice Hall, New York, 1994).

[66] T. Young, Phil. Trans. Roy. Soc. **92**, 12 (1802).

[67] P. Hariharan, *Optical Holography: Principles, Techniques and Applications* (Cambridge University Press, New York, 1996).

[68] C. C. Bowley and G. P. Crawford, Appl. Phys. Lett. **76**, 2235 (2000).

[69] K. Tanaka, K. Kato, S. Tsuru, and S. Sakai, J. Soc. Inf. Disp. **2**, 37 (1994).

[70] M. Date, N. Naito, K. Tanaka, K. Kato, and S. Sakai, Asia Display p. 603 (1995).

[71] K. Tanaka, K. Kato, and M. Date, Jpn J. Appl. Phys. **38**, L277 (1999).

[72] J. Qi, L. Li, M. D. Sarkar, and G. P. Crawford, Soc. Inf. Disp. Dig. **XXXIII**, 538 (2002).

[73] J. Qi, M. D. Sarkar, G. T. Warren, and G. P. Crawford, J. Appl. Phys. **91**, 4795 (2002).

[74] R. T. Pogue, R. L. Sutherland, M. G. Schmitt, L. V. Natarajan, S. A. Siwecki, V. P. Tondiglia, and T. J. Bunning, Appl. Spectr. **54**, 12 (2000).

[75] C. Bowley, P. Kossyrev, G. P. Crawford, and S. Faris, Appl. Phys. Lett. **79**, 9 (2001).

[76] K. Kato, T. Hisaki, and M. Date, JPn. J. Appl. Phys. **38**, 805 (1999).

[77] L. Domash, G. P. Crawford, A. Ashmead, R. Smith, M. Popovich, and J. Storey, Proc. SPIE **4107**, 46 (2000).

[78] L. Domash, US Patent 5.937.115 (1999).

[79] T. Stone and M. Malcult, US Patent 5.982.515 (1999).

[80] T. Stone, US Patent 6.072.923 (2000).

[81] R. L. Sutherland, L. Natarajan, V. P. Tondiglia, T. J. Bunning, and W. W. Adams, Appl. Phys. Lett. **64**, 1074 (1994).

[82] R. L. Sutherland, L. Natarajan, V. P. Tondiglia, and T. J. Bunning, Chem. Matter **5**, 1533 (1993).

[83] T. Karasawa and Y. Taketomi, Jap. J. Appl. Phys. **36**, 6388 (1997).

[84] M. Jazbinsek, I. Olenik, M. Zgonik, A. Fontecchio, and G. P. Crawford, J. Appl. Phys. **90**, 3831 (2001).

[85] K. Vardanyan, J. Qi, J. Eakin, M. D. Sarkar, and G. P. Crawford, Appl. Phys. Lett. **81**, 4736 (2002).

[86] Y. Boiko, J. Eakin, J. Vedrine, and G. P. Crawford, Opt. Lett. **27**, 1717 (2002).

[87] G. Montemezzain and M. Zgonik, Phys. Rev. E **55**, 1035 (1997).

[88] A. G. Fuh, C. R. Lee, Y. H. Ho, T. S. Mo, and P. M. Liu, Jpn. J. Appl. Phys. **40**, 6868 (2001).

[89] A. G. Fuh, C. R. Lee, Y. H. Ho, T. S. Mo, and P. M. Liu, Applied Optics **41**, 4585 (2002).

[90] J. Zhang and M. B. Sponsler, J. Am. Chem. Soc. **114**, 1506 (1992).

[91] J. Zhang, C. R. Carlen, S. Palmer, and M. B. Sponsler, J. Am. Chem. Soc. **116**, 7055 (1994).

[92] R. A. M. H. D. J. Broer and G. Challa, Makromol. Chem. **190**, 3201 (1989).

[93] D. J. Broer and G. N. Mol, Makromol. Chem. **192**, 59 (1991).

[94] M. S. H. Thiem, P. Strohriegl and I. McCulloch, Makromol. Chem. Phys. **206**, 2153 (2005).

[95] T. J. Bunning and F. Kreuzer, Trends Polym. Sci. **3**, 318 (1995).

[96] N. Gill, J. B. W. Jr., and N. Woullard, ACS Poly. **40**, 524 (1999).

[97] Y. M. Date and K. Kato, J. Phys. D. **31**, 2225 (1998).

[98] G. Smith, Mol. Cryst. Liq. Cryst. **196**, 89 (1991).

[99] C. Bowley, A. K. Fontecchio, H. Yuan, and G. P. Crawford, SID Technical Papers **30**, 958 (1999).

[100] T. Karasawa and Y. Taketomi, Jpn. J. Appl. Phys. **36**, 6388 (1997).

[101] T. J. Bunning, L. V. Natarajan, V. Tondiglia, R. L. Sutherland, R. Haaga, and W. Adams, Proc. SPIE **2651**, 44 (1996).

[102] A. Y. G. Fuh, T. C. Ko, M. S. Tsai, C. Y. Huang, and L. C. Chien, J. Appl. Phys. **83**, 679 (1998).

[103] A. Y. G. Fuh, C. C. Liao, K. C. Hsu, C. Lu, and C. Y. Tsai, Opt. Lett. **26**, 1767 (2001).

[104] R. Caputo, A. Sukhov, N. Tabirian, and C. Umeton, Chem. Phys. **245**, 463 (1999).

[105] R. Caputo, A. Sukhov, and C. Umeton, Mol. Mater. **12**, 169 (2000).

[106] R. Caputo, A. Sukhov, N. Tabirian, C. Umeton, and R. F. Ushakov, Chem. Phys. **271**, 323 (2001).

[107] C. Carre, D. J. Lougnot, and J. P. Fouassier, Macromolecules **22**, 791 (1989).

[108] G. Elicabe and H. A. L. R. J. Williams, Macromolecules **31**, 8173 (1998).

[109] V. Colvin, R. Larson, A. Harris, and M. Schilling, J. Appl. Phys. **81**, 5913 (1997).

[110] J. Fouassier, *Photoinitiation, Photopolymerization and Photocuring: Fundamentals and Applications* (Hanser, Munich, 1995).

[111] M. Escuit, J. Qi, and G. Crawford, Opt. Lett. **28**, 522 (2003).

[112] J. Jackson, *Classical Electrodynamics* (Wiley, New York, 1999).

[113] P. Yeh, *Introduction to Photorefractive Nonlinear Optics* (Wiley, New York, 1993).

[114] C. Raman and N. Nath, Proc. Ind. Acad. Sci. A **2**, 406 (1935).

[115] H. Kogelnik, Bell. Sys. Tech. J. **48**, 2909 (1969).

[116] M. Born and E. Wolf, *Principles of Optics* (Cambridge University Press, Cambridge, 1980).

[117] W. Helfrich, Phys. Rev. Lett. **24**, 201 (1970).

[118] P. G. de Gennes, Mol. Cryst. Liq. Cryst. **12**, 193 (1971).

[119] V. Freedericksz and V. Zolina, Trans. Faraday Soc. **29**, 919 (1933).

[120] I. N. Bronshtein and K. A. Semendyayev, *Handbook of Mathematics* (Springer, Berlin, 1998).

[121] F. Brochard, P. Pieranski, and E. Guyon, Phys. Rev. Lett. **28**, 1681 (1972).

[122] J. Nehring, A. Kmetz, and T. Scheffer, J. Appl. Phys. **47**, 850 (1976).

[123] N. Aoki, Y. Ohki, and K. Yanagi, Jpn. J. Appl. Phys. **18**, 523 (1979).

[124] F. Leslie, J. Phys. D **3**, 889 (1970).

[125] G. Arfken, *Mathematical Methods for Physicists* (Academic Press, New York, 1968).

[126] B. Wu, J. Edrmann, and J. Doane, Liq. Cryst. **5**, 1453 (1989).

[127] A. Golemme, S. Zumer, J. Doane, and M. Neubert, Phys. Rev. A **37**, 559 (1988).

[128] R. M. Henry, R. A. Ramsey, and S. C. Sharma, J. Polym. Sci. B **42**, 404 (2003).

[129] R. M. Henry, S. C. Sharma, R. A. Ramsey, M. L. Cramer, and J. B. Atman, J. Polym. Sci. B **43**, 1842 (2005).

[130] A. K. Fontecchio, C. C. Bowley, H. Yuan, and G. P. Crawford, Mol. Cryst. Liq. Cryst. **352**, 399 (2000).

[131] H. M. J. Boots, J. G. Kloosterboer, C. Serbutoviez, and F. J. Touwslager, Macromolecules **29**, 7683 (1996).

[132] G. Wu, J. H. Erdmann, and J. W. Doane, Liq. Cryst. **5**, 1453 (1989).

[133] R. A. Ramsey and S. C. Sharma, Opt. Lett. **30**, 592 (2005).

[134] G. Wu, J. H. Erdmann, and J. W. Doane, Liq. Cryst. **5**, 1453 (1989).

[135] T. J. Bunning, L. V. Nataranjan, V. Tondiglia, R. Sutherland, and W. W. Adams, Polymer **36**, 2699 (1995).

[136] R. A. Ramsey and S. C. Sharma, Appl. Phys. Lett **88**, 051,121 (2006).

[137] A. K. Fontecchio, C. C. Bowley, H. Yuan, and G. P. Crawford, Mol. Cryst. Liq. Cryst. **352**, 399 (2000).

[138] C. C. Bowley and G. P. Crawford, Appl. Phys. Lett. **76**, 2235 (2000).

[139] R. L. Sutherland, L. V. Nataranjan, V. Tondiglia, and T. J. Bunning, Mol. Cryst. Liq. Cryst. **358**, 23 (2001).

[140] J. Qi and G. P. Crawford, Display. **25**, 177 (2005).

[141] M. Jazbinsek, I. D. Olenik, M. Zgonik, A. K. Fontecchio, and G. P.Crawford, J. Appl. Phys. **90**, 3831 (2001).

[142] T. Jannson, I. Tengara, Y. Qiao, and G. Savant, J. Opt. Soc. Am. A **8**, 201 (1991).

[143] D. J. Broer, J. Boven, G. N. Mol, and G. Challa, Makromol. Chem. **190**, 2255 (1989).

[144] M. Schadt, Mol. Cryst. Liq. Cryst. **89**, 72 (1982).

[145] R. A. M. Hikmet, B. H. Zwerverand, and D. J. Broer, Polymer **33**, 89 (1992).

[146] K. Kato, T. Hisaki, and M. Date, Jpn. J. Appl. Phys. **38**, 805 (1999).

BIOGRAPHICAL STATEMENT

Robert A. Ramsey was born in Nacogdoches, TX, in 1974. He received his B.S. in Electrical Engineering and a B.S. in Physics from University of Texas at Arlington, in 2001. His current research interest is in the area of experimental soft matter physics and applied non-linear optics. He is a member of APS, Sigma Xi, ACS, International Liquid Crystal Society, SPS, SPIE, and IEEE.